UNIVERSITY OF CALIFORNIA
SANTA CRUZ

PROBING HIERARCHICAL GALAXY FORMATION WITH SDSS-IV MANGA

A dissertation submitted in partial satisfaction of the
requirements for the degree of

DOCTOR OF PHILOSOPHY

in

ASTRONOMY AND ASTROPHYSICS

by

Grecco A. Oyarzún Martínez

June 2022

The Dissertation of Grecco A. Oyarzún Martínez
is approved:

Professor Constance M. Rockosi, Chair

Professor Kevin Bundy

Professor Nia Imara

Peter F. Biehl
Vice Provost and Dean of Graduate Studies

Table of Contents

List of Figures

List of Tables

Abstract

Probing hierarchical galaxy formation

with SDSS-IV MaNGA

by

Grecco A. Oyarzún Martínez

In our current picture of the Universe, galaxies form and evolve in dark-matter structures known as dark-matter halos. Although the relationship between galaxies and halos has been extensively studied in the theory, our observational understanding of the galaxy-halo connection is far more limited. In this Thesis, I will present observational evidence of this connection through spatially resolved spectroscopy for thousands of nearby galaxies from the SDSS-IV MaNGA survey. I will show that the radial stellar metallicity profiles of massive galaxies contain signatures of minor mergers, a key feature of late-time halo growth. I will also show that the stellar populations parameters of passive central galaxies, namely stellar age, iron-abundance, and magnesium-enhancement, depend not only on the stellar mass of the galaxy, but also on proxies for the masses and formation times of their host halos. These results indicate that dark-matter halos not only dictate how much stellar mass central galaxies build-up, but can also affect their star-formation timescales and chemical enrichment histories. Finally, I will show that satellite galaxies are also affected by the properties of dark-matter halos. Satellites in denser local environments feature old, alpha-enriched stellar components, indicating that satellite quenching is facilitated by halo-driven mechanisms.

To my parents,

Ana María and Grecco,

whose sacrifice, vision, and foresight allowed me to aim for the stars

Acknowledgments

First, I would like to thank my advisor, Kevin Bundy, for his mentorship and support throughout the past six years. Without his guidance and expertise, this Thesis would not have been possible. I am also grateful to my dissertation committee members, Connie Rockosi and Nia Imara, and qualifying committee members, Alexie Leauthaud and Charlie Conroy, for their comments and suggestions that helped shape this work.

I also want to acknowledge Kyle Westfall and Francesco Belfiore for the all the valuable research discussions. Also thank everyone that made the fantastic SDSS-IV MaNGA survey possible. A big thanks to David Law, Renbin Yan, Matt Bershady, David Wake, Niv Drory, Karen Masters, Joel Brownstein, Brett Andrews, Brian Cherinka, José Sánchez-Gallego, Alfonso Aragón-Salamanca, Claudia Maraston, Sebastían Sánchez, and all the others that I have not yet had the pleasure to meet. I also want to acknowledge everyone at UC Santa Cruz that was ever involved in the installation and maintenance of the supercomputers Comrade, Graymalkin, and Lux that were instrumental to this work.

The text of this dissertation includes a reprint of the following previously published material: Oyarzún, G. A., Bundy, K., Westfall, K. B., et al. 2019, ApJ, 880, 111; doi= 10.3847/1538-4357/ab297c © AAS. Reproduced with permission. The co-authors listed in this publication directed and supervised the research which forms the basis for the dissertation. My contribution to the aforementioned publication was to act as the lead researcher, and therefore performed the majority of the data analysis, figure production, and text composition.

This Thesis would not have been possible without the support of my parents, Ana María and Grecco. Their priority always was to give their children access to the tools and opportunities to succeed, and for that I will be forever grateful. I would also like to acknowledge María José, my sister, for being a great companion in life. I also want to thank Enia Xhakaj for her love and support. The 2020s were difficult years for many reasons, and yet they are packed with highlights thanks to you.

Last but not least, I want to thank my friends for the joyful moments and unwavering support. To the friendships that stand the test of time: Sebastián Muñoz, Luis Zuñiga, Samy Naser, Alex Adrián, Diego González, Jorge Martínez, Juan Pablo Cordero, Juan Molina, Pepe Peña, Matías Díaz, and Sebastián Marchi. Also, to the friends that I made in Santa Cruz: Platon Karpov, Matt Siebert, Zack Briesemeister, Amanda Quirk, Callie Hood, César Rojas-Bravo, Chris Bradshaw, and Viraj Pandya. Graduate school was full of great memories because of you.

Chapter 1

Introduction

One of the most notorious features of galaxies in the nearby Universe is the existence of a morphological dichotomy. Late-type galaxies are disk-dominated, whereas early-type galaxies feature prominent spheroidal components. This dichotomy inspired a debate in the 20th century about the true origin of early-type galaxies. Do they originate from the physical disruption of a late-type galaxy (e.g. "ram-pressure stripping"; Gunn & Gott 1972)? Or perhaps they stem from gravitational instabilities that lead to subsequent collapse and star-formation (e.g. "monolithic collapse"; Eggen et al. 1962; Lynden-Bell 1967; Sandage et al. 1970)?

The monolithic collapse picture gained a lot of traction in the latter half of the 20th century (Eggen et al. 1962). Once a gravitationally bound region of intergalactic material would reach a critical density, its gravitational pull cannot be sustained by its thermal energy any further and it collapses. This collapse occurs in a runaway fashion where condensations become globular clusters and stars. The spheroidal morphology of

the resulting system would be consistent with early-type galaxies. Later on, the angular momentum of the galaxy stalls the collapse in all but the rotating axis, resulting in a disk and giving origin to late-type galaxies.

Despite its early success, it would later become clear that the "monolithic collapse" scenario cannot explain the compactness of massive early-type galaxies at high redshift ($M_* > 10^{11.5} M_\odot$ at $z > 2$; Toft et al. 2007; Cimatti et al. 2008; Buitrago et al. 2008; van Dokkum et al. 2010). Since $z \sim 2$, the stellar masses (M_*) of early-type galaxies have increased by a factor of two, yet their effective radii (R_e) have increased by factor of three to six (see Figure 1.1; Daddi et al. 2005; Trujillo et al. 2006a,b, 2007; Zirm et al. 2007; van der Wel et al. 2008; van Dokkum et al. 2008; Damjanov et al. 2009; Cassata et al. 2010). Why are early-type galaxies in the nearby Universe only slightly more massive, yet so much larger than these "red nuggets" at high-redshift? (e.g. van Dokkum et al. 2009; Newman et al. 2010; Damjanov et al. 2011; Whitaker et al. 2012; Dekel & Burkert 2014).

Several studies have attempted to explain this observation (e.g. Barro et al. 2013; Cappellari et al. 2013; Wellons et al. 2016). For instance, Hopkins et al. (2010a) considered mechanisms like major and minor mergers, adiabatic expansion (Fan et al. 2008, 2010), gradients in stellar mass-to-light ratio (Hopkins et al. 2008), mass uncertainties (van Dokkum et al. 2010), and observational biases as possible drivers. Figure 1.2 shows the impact that each mechanism would have on the observed stellar mass surface density profiles of nearby early-type galaxies. Of the simulated scenarios, only minor mergers and stellar accretion can explain the extended stellar envelopes in the surface brightness profiles of massive galaxies at low redshift (also in Figure 1.2; Huang et al. 2013b,a)

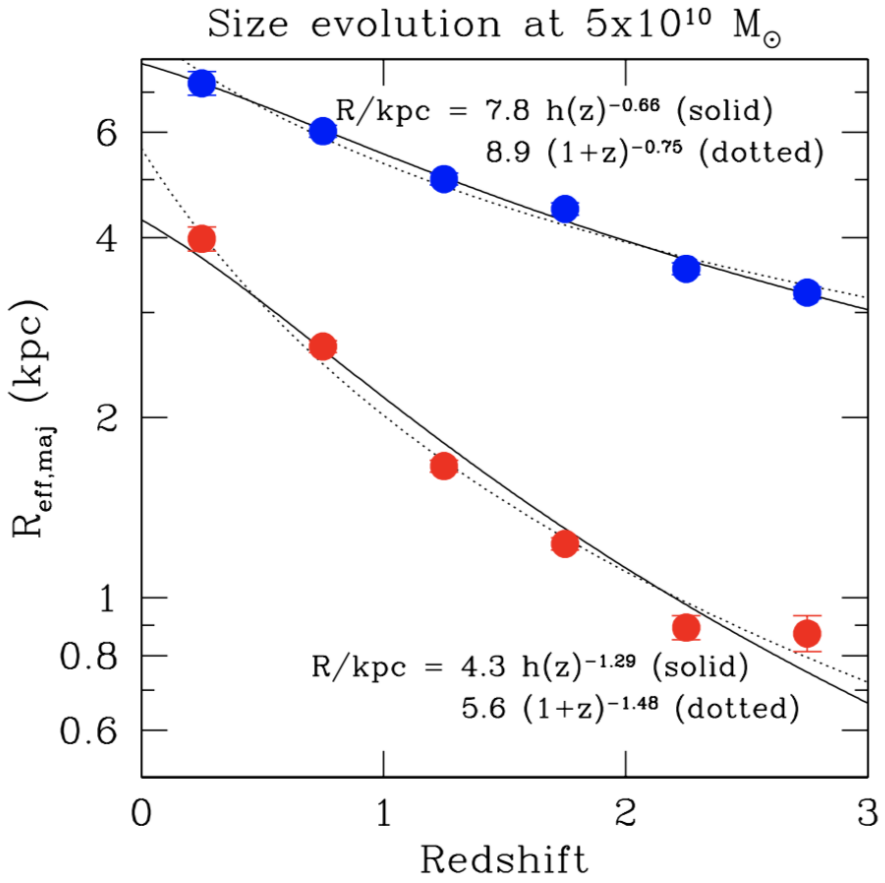

Figure 1.1: Figure from van der Wel et al. (2014). Average sizes of early-type (red) and late-type (blue) galaxies as a function of redshift for $M_* \sim 5 \times 10^{10} M_\odot$. At these high stellar masses, early-type galaxies are remarkably compact at high redshift, hence the term "red nuggets".

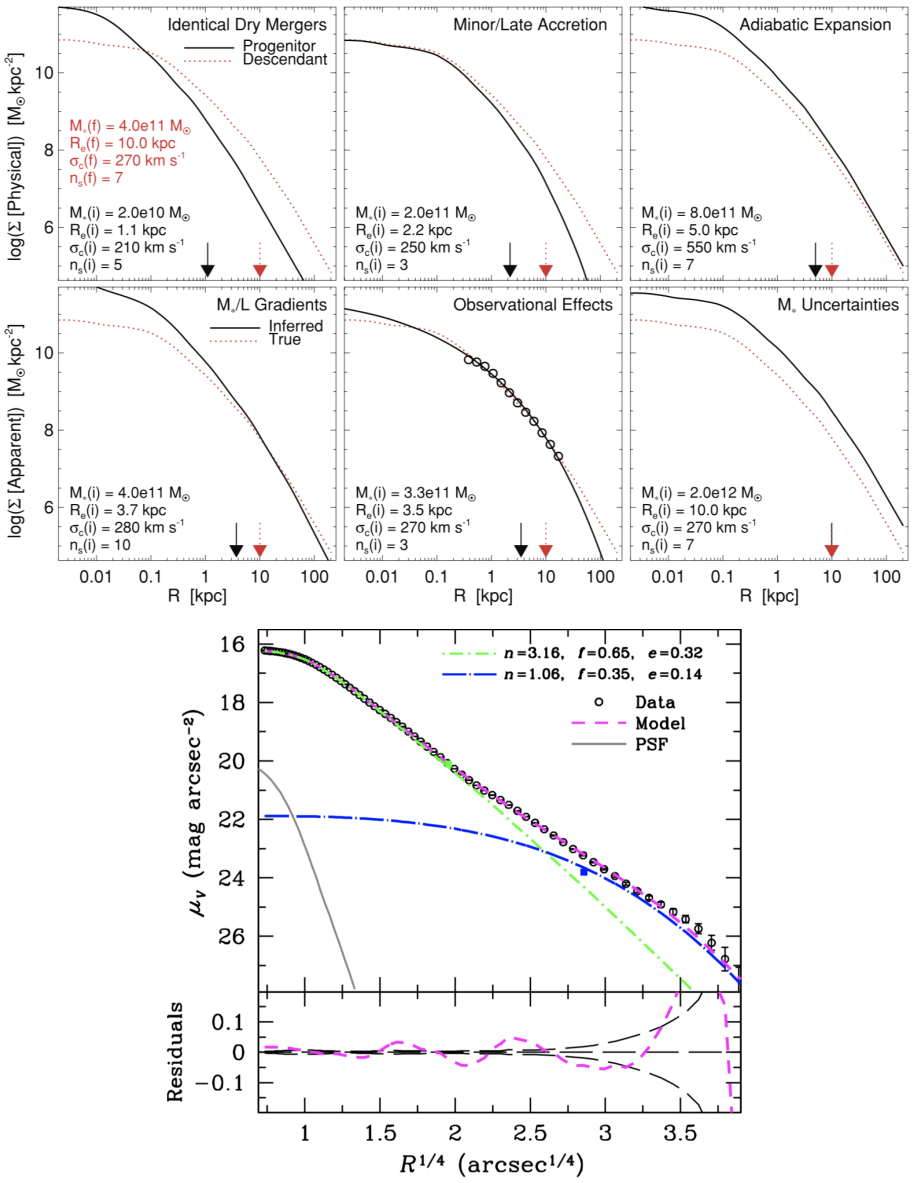

Figure 1.2: Top: Figure from Hopkins et al. (2010a). Effect of physical mechanisms and observational biases on the observed stellar mass surface density profiles of early-type galaxies. Bottom: Figure from Huang et al. (2013b). Observed surface brightness profiles of nearby early-type galaxies. The existence of an outer envelope in the surface brightness profile is consistent with the stellar accretion scenario.

Stellar accretion not only can explain the shape of the stellar mass surface density profiles of massive nearby galaxies, but it also fits very well with our current cosmological picture for the formation and evolution of structure (Oser et al. 2010, 2012; Johansson et al. 2012b). Galaxies assemble at the center of dark-matter halos where the gas was able to cool and form stars. The matter power spectrum indicates that the cores of galaxies formed first (i.e. *in-situ* growth), and then grew larger in mass and size through halo and galaxy mergers (i.e. *ex-situ* growth) that efficiently increased their effective radii and stellar masses (e.g. Bezanson et al. 2009).

That said, it is unclear how consistent the hierarchical formation picture is with observations of galaxy stellar populations. For instance, it is well known that the bulk of the stars in massive galaxies are old, indicating that they assembled at high-redshift (i.e. *downsizing*; e.g. Thomas et al. 2005). This appears to be at odds with the "bottom-up" fashion of halo formation, where high-mass halos form later than low-mass halos. A possible explanation for this apparent inconsistency is that galaxy assembly does not necessarily coincide with halo assembly (Neistein et al. 2006). Indeed, recent models of hierarchical formation have argued that massive galaxies assemble early because they can efficiently cool their gas and therefore form stars at early times (e.g. Moster et al. 2013). Instead, the late assembly of their host dark-matter halos would have an impact on how much stellar mass is accreted from satellite galaxies (e.g. De Lucia & Blaizot 2007).

The implication that massive early-type galaxies formed their stars early and exhausted their gas reservoirs rapidly is consistent with their high quenched fractions at low redshift. This scenario has motivated the concept of "red and dead" or "passive" galaxies

to refer to early-type galaxies at high stellar masses ($M_* > 10^{10} M_\odot$; e.g. Lacerna et al. 2020). Throughout this Thesis, we refer to galaxies with both low star-formation rates and elliptical morphology as early-types, while galaxies with low star-formation rates are referred to as passive.

A greater challenge for the hierarchical formation scenario has been to explain the spatial distribution of the stellar populations in nearby early-type galaxies. In hierarchical formation models, stars formed *in-situ* dominate at the centers of galaxies, whereas *ex-situ* stars are more prominent beyond the effective radii (Zolotov et al. 2009). Hydrodynamical simulations argue that this radial transition from *in-situ* to *ex-situ* stars leaves imprints in the stellar populations of early-type galaxies, particularly by flattening the stellar metallicity profiles as stellar mass increases (e.g. Cook et al. 2016). Unfortunately, no conclusive evidence supporting this flattening of the stellar metallicity profile had been found in observational work.

Carollo et al. 1993 measured the radial gradient of magnesium-sensitive stellar absorption features in 42 nearby galaxies with long-slit spectroscopy. In tension with merger-driven growth, the gradients within $0.5R_e$ show no dependence on stellar mass for $M_* > 10^{11} M_\odot$. It could be argued that the flattening of the metallicity profile only becomes apparent beyond the R_e, explaining why long-slit spectroscopic work that followed found evidence of flattening around the R_e (e.g. Sánchez-Blázquez et al. 2007; Spolaor et al. 2009). However, later work with larger IFU samples would report that no clear correlation exists between the stellar metallicity gradients of galaxies and their stellar masses or central velocity dispersions (e.g. González Delgado et al. 2015; Greene et al. 2013, 2015; Zheng et al.

2017; Goddard et al. 2017a,b).

In part, these struggles came from the sample size and spectral signal-to-noise limitations of IFU surveys at the time (i.e. 2016-2017). The MaNGA (Bundy et al. 2015) samples used in Zheng et al. (2017); Goddard et al. (2017a,b) had less than 2,000 galaxies, and yet they were the largest IFU samples back then (Wake et al. 2017). In contrast, work that measured the stellar population parameters in galaxies from the SDSS MAIN Galaxy Survey (York et al. 2000; Gunn et al. 2006; Alam et al. 2015) boosted over 300,000 objects (e.g. Pasquali et al. 2010).

Fortunately, the MaNGA survey completed observations in 2020 and now boosts over 10,000 galaxies, five times more than in 2017 (Bundy et al. 2015; Yan et al. 2016a). Its combination between sample size, wavelength coverage ($3600 - 10300$Å), spatial resolution ($\sim 2 - 5$kpc), and radial coverage (out to $1.5R_e$) make it the ideal dataset for probing how galaxies assembled their stellar components (Drory et al. 2015; Law et al. 2015; Wake et al. 2017). This is highlighted in the comparison between the constraining powers of modern IFU surveys shown in Figure 1.3. In this Thesis, I will take advantage of the now completed MaNGA survey to revisit some of the questions about the hierarchical formation picture that remain unsolved.

Unfortunately, sample size was not the only factor limiting our ability to constrain the stellar metallicity profiles of nearby galaxies. Stellar population parameters measured from optical spectra are plagued by inaccuracies and biases. The spectral response to changes in the stellar parameters is highly non-linear, and the spectral imprints left by stellar age, metallicity, element abundances, and IMF are quite degenerate (e.g. Conroy

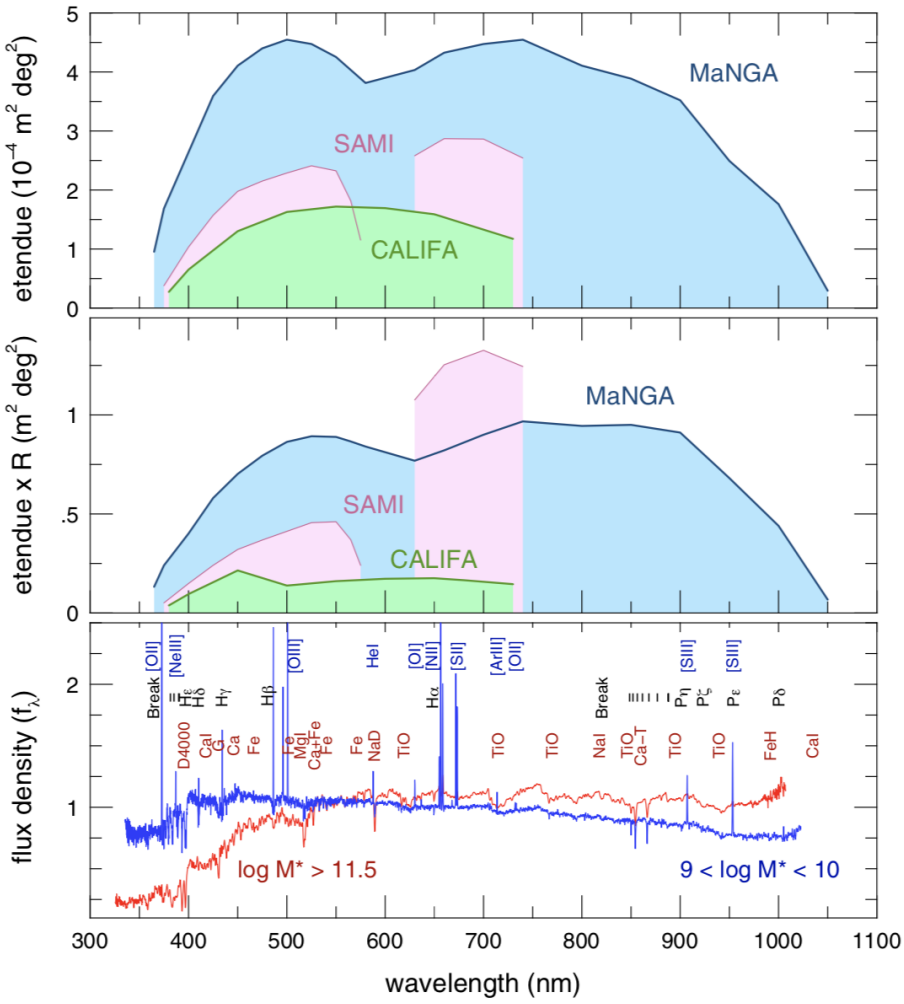

Figure 1.3: Figure from Bundy et al. (2015). Compared here are the gathering powers of modern IFU surveys. Etendue quantifies the collecting power of each survey by considering the telescope collecting area, instrument sensitivity, and sample size considerations. The middle panel shows etendue multiplied by the spectral resolution, therefore also accounting for the spectral resolving power of the survey. The bottom panel highlights the chemical information probed by the spectrographs used in MaNGA (Dawson et al. 2013).

et al. 2018). As a result, estimates of stellar population parameters from galaxy spectra are strongly sensitive to the approach to stellar population synthesis and template fitting. This is highlighted in Figure 1.4, where the scatter in the stellar metallicities derived by different stellar population fitting codes can exceed 0.2 dex for early-type galaxies and 1 dex for late-type galaxies.

In this Thesis, I will address the issue of stellar population characterization accuracy in three different ways. First, I will employ several stellar population fitting codes to control for systematics in the stellar population synthesis and fitting approach. Second, I will employ direct spectral comparison as a completely-model free method to detect stellar population variations. Finally, I will also turn to the stellar population fitting program `alf` (Conroy & van Dokkum 2012; Conroy et al. 2018) that is designed to measure the stellar population parameters of old stellar systems ($\gtrsim$1 Gyr) with high precision while also accounting for uncertainties in stellar evolution.

As I will show in Chapter 2 of this Thesis, signatures of minor mergers are apparent in the stellar metallicity profiles of nearby galaxies once some of these difficulties are circumvented. After comparing the outputs from the stellar population fitting codes FIREFLY, pPXF, and Prospector to control for systematic errors, I will show that the average metallicity profiles of early-type galaxies in various stellar mass bins are not linear. As a result, these profiles are poorly characterized by a single gradient value, explaining why weak trends reported in previous work can be difficult to interpret. Instead, I examined the full radial extent of stellar metallicity profiles and found them to flatten in the outskirts of $M_* \gtrsim 10^{11} M_\odot$ early-types. This is a signature of stellar accretion. Based on a toy model

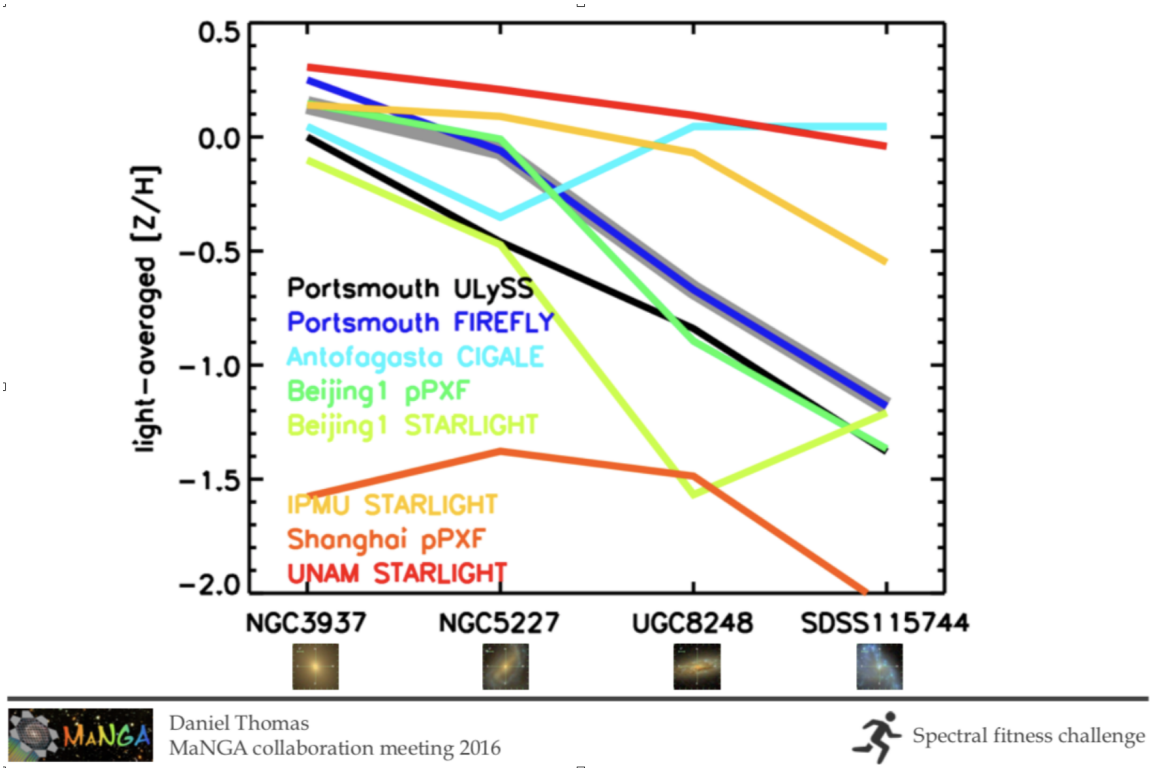

Figure 1.4: Figure from the MaNGA Collaboration Meeting in 2016. Members of the collaboration were tasked with fitting optical galaxy spectra with their stellar population fitting code of choice. Shown are the light-weighted stellar metallicites recovered by the different codes for four different galaxies. Note how the measured [Z/H] is strongly dependent on the code that was used, even for early-type galaxies.

for stellar metallicity profiles, I inferred the *ex-situ* stellar mass fraction in early-type as a function of stellar mass and galactocentric radius. I found that *ex-situ* stars at R$\sim$2R$_{\rm e}$ make up 20% of the projected stellar mass of M$_* \lesssim 10^{10.5}$M$_\odot$ early-type galaxies, rising up to 80% for M$_* \gtrsim 10^{11.5}$M$_\odot$ counterparts, in consistency with predictions from hierarchical formation (e.g. Rodriguez-Gomez et al. 2016).

Based on this result, it is natural to expect the assembly histories of galaxies to be determined not only by the physical conditions of their formation at high redshift (i.e. "nature"), but also by their local environment (i.e. "nurture"). This prediction is particularly well defined for central galaxies, as they are believed to form their cores *in-situ* before building-up stellar mass through the accretion of stellar envelopes from satellite galaxies. However, studies of nearby galaxies have found little evidence that galaxy stellar populations depend on the local environment, instead concluding that the *in-situ* formation histories of galaxies are by far the dominant factor. For instance, Peng et al. (2012) found that the fraction of red centrals in SDSS does not depend on local environment but only on stellar mass (see Figure 1.6). Even more puzzling is that La Barbera et al. (2014) and Greene et al. (2015) find conflicting results on how the stellar metallicities of centrals depend on environment at fixed central velocity dispersion.

Alternatively, the role of local environment in galaxy formation can be constrained through structural arguments. Early-type galaxies are dominated by random motions, meaning that their central stellar velocity dispersions (σ_*) can be used to estimate their total stellar masses with the Virial Theorem. Indeed, masses derived via this method show consistency with masses inferred from the luminosity or surface brightness (I_e) of

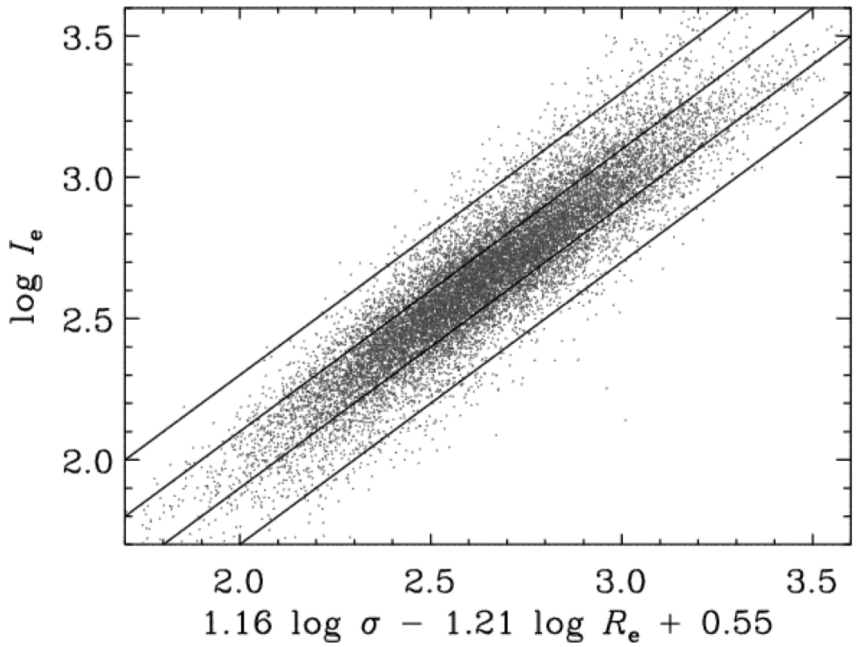

Figure 1.5: Figure from Graves et al. (2009). Early-type galaxies occupy a two-dimensional surface in central velocity dispersion, central surface brightness, and effective radius space.

the galaxy (Faber & Jackson 1976a). It would later be discovered that early-type galaxies actually occupy a two-dimensional surface in the space composed by σ_*, I_e, and galaxy size (parameterized by the effective radius R_e). This two-dimensional surface is known as the fundamental plane of early-type galaxies (FP; Dressler et al. 1987; Djorgovski & Davis 1987) shown in Figure 1.5.

As galaxies residing in different local environments are expected to experience unique variations to their stellar masses and sizes, there is the expectation that galaxies in different environments would deviate or "tilt" the FP (e.g. D'Onofrio & Chiosi 2021). However, linking hierarchical formation with variations of the FP has proven to be challenging. While some work argue that minor mergers "tilt" the FP (e.g. Taranu et al. 2015),

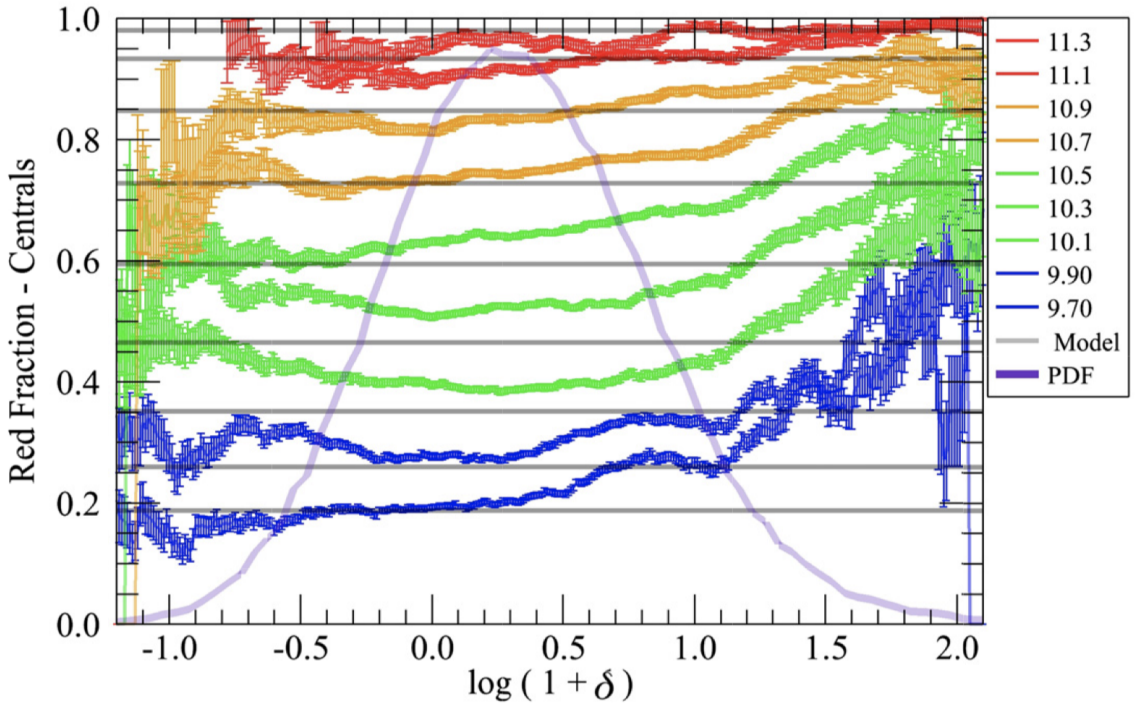

Figure 1.6: Figure from Peng et al. (2012) that shows the fraction of red central galaxies from SDSS in narrow stellar mass bins as a function of overdensity (within the 5th closest neighbor). Note how the the fraction of red centrals depends almost solely on stellar mass.

other studies indicate that their effect is limited to the addition of scatter (e.g. Nipoti et al. 2003). Using the FP to search for evidence of merger-driven growth is further hampered by how other structural perturbations can also affect the coefficients and scatter of the FP (e.g. variations in the stellar initial mass function or dynamical non-homology; D'Onofrio & Chiosi 2021).

In the current scenario of subtle trends and conflicting results, data-driven methods can be very powerful. In Chapter 3 of this Thesis, I will show that the strength of several stellar absorption features in central galaxies from MaNGA vary systematically with local

environment at fixed stellar mass. Completely model-free, this is one of the first indications that the stellar populations of centrals with identical stellar mass are affected by the properties of their host halos. To interpret these variations, I applied full spectral fitting with the code `alf`. At fixed stellar mass, centrals in more massive halos are older, show lower [Fe/H], and have higher [Mg/Fe] with 3.5σ confidence. Halos not only dictate how much M_* galaxies assemble, but also modulate their chemical enrichment histories.

From a theoretical perspective, halo mass (M_h) is a more fundamental property than stellar mass. Massive dark-matter halos provide the gravitational potential required for gas accretion and retention, therefore facilitating star-formation and stellar mass build up in galaxies (e.g. Moster et al. 2013). For this reason, in Chapter 3 I will also turn to a stellar population analysis at fixed halo mass. I found that in halos of the same mass today, centrals with higher stellar mass are older, show lower [Fe/H], and have higher [Mg/Fe] for $M_h > 10^{12} M_\odot$ with confidence $> 4\sigma$. While massive early-type galaxies are thought to form early and rapidly, my results are among the first to distinguish these trends at fixed halo mass. They suggest that centrals with high M_*-to-M_h ratios experienced unique *early* formation histories, possibly through enhanced collapse and gas fueling at high-redshift.

Alternatively, it is possible that these stellar population variations at fixed halo mass are driven by secondary halo properties. Halo formation time and halo concentration are also believed to play roles, albeit secondary, in how efficiently galaxies assemble their stellar components, an effect known as *galaxy assembly bias* (Matthee et al. 2017; Xu & Zheng 2020). It is possible that centrals with high M_*-to-M_h ratios are old, have high [Mg/Fe], and show low [Fe/H] because they assembled in old, highly concentrated dark-

matter halos.

Though tentative detections of galaxy assembly bias have been reported in observations, their reliability has been questioned due to the biases that plague group finding algorithms and catalogs (e.g. Campbell et al. 2015). In Chapter 4, I will search for evidence of galaxy assembly bias in the population of red central galaxies of SDSS with the new SDSS group catalog by Tinker (2020a,b). This catalog is designed to mitigate many of the biases affecting previous group catalogs and exploits deep imaging data from the DESI Legacy Imaging Survey (Dey et al. 2019). I will report that centrals with high M_*-to-M_h ratios have higher environmental densities within $10h^{-1}$ Mpc, indicating that they assembled in older dark-matter halos. This result is perhaps the most significant evidence of galaxy assembly bias to date, suggesting that early halo formation leads to fast stellar mass build-up, rapid quenching, and efficient metal retention.

One of the successes of the hierarchical formation scenario is that it can successfully explain some of the differences between the central and satellite galaxy populations. Satellites are older and more often quenched than centrals of the same stellar mass, suggesting that host halos facilitate satellite quenching (see Figure 1.7). In fact, the outskirts of satellites show some suppression of star-formation (Schaefer et al. 2017) and deficit of M_* (Spindler & Wake 2017a), in consistency with halo-driven quenching. That said, studies have found no difference in how the stellar populations of centrals and satellites are spatially distributed within the galaxy. For instance, Santucci et al. (2020) found little difference between the stellar age, metallicity, and [α/Fe] gradients of central and satellite galaxies in the SAMI survey (Allen et al. 2015). Goddard et al. (2017b) and Zheng et al. (2017)

reached the same conclusion in MaNGA.

In Chapter 5, I will show evidence for subtle, yet systematic differences in the radial profiles of stellar population parameters within satellites compared to centrals after exploiting the full MaNGA sample and the new SDSS group catalog by Tinker (2020a,b). Except for the most massive galaxies ($M_* \lesssim 10^{12} M_\odot$), the stellar populations within 1.5 effective radii (R_e) of passive satellites are older and metal-enriched compared to those of passive centrals with the same stellar mass, a result in agreement with a similar signal previously reported (e.g. Pasquali et al. 2010). These differences are more pronounced in higher M_h halos, suggesting an important role for the host halo in driving satellite formation histories. I also find a residual halo-mass dependent signal even in more distant satellites that are expected to have more recently joined the halo, perhaps a signature of "pre-processing" prior to infall. For the first time, I find subtle but systematic differences in the radial profiles of stellar population parameters within satellites compared to centrals. Among $M_* \sim 10^{10} M_\odot$ satellites, the stars beyond 1.5 R_e appear to be older and alpha-enhanced compared to their counterparts in the outer regions of centrals. Although satellites may quench as a result of internal processes, their detailed evolution appears subject to unique environment-driven effects.

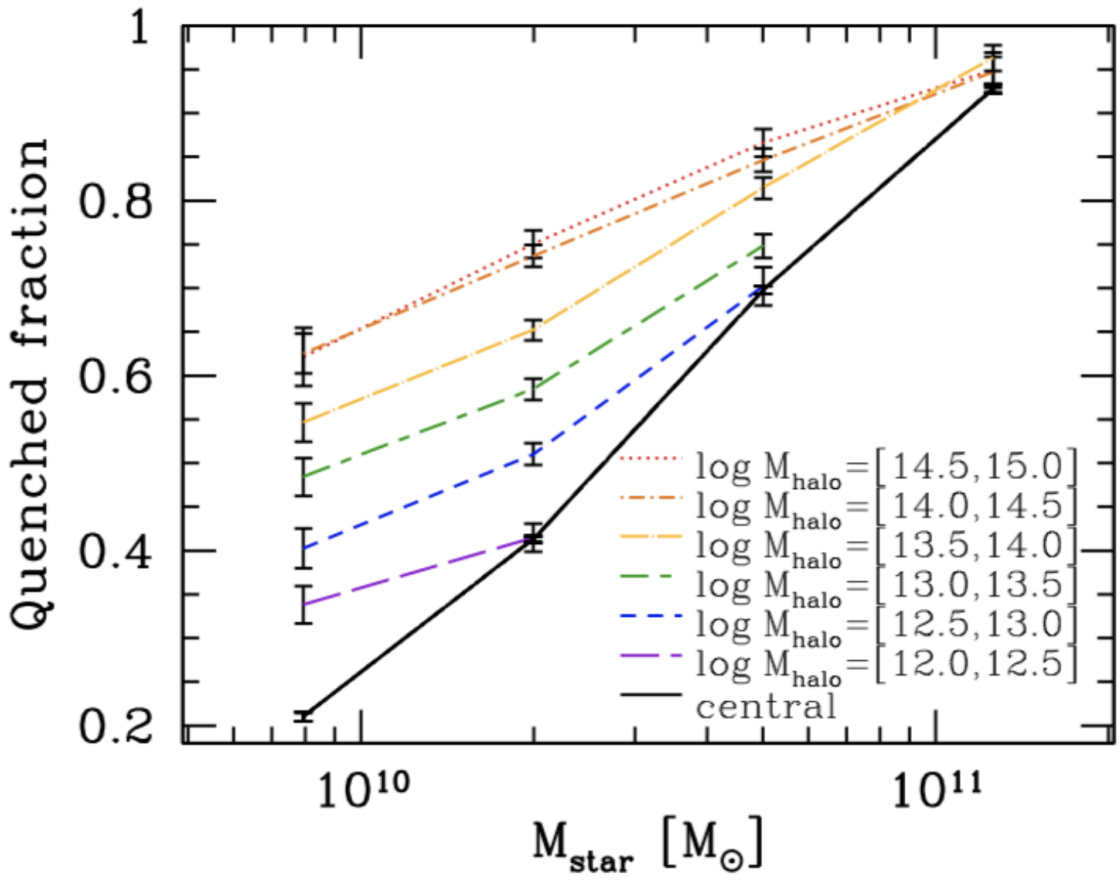

Figure 1.7: Figure from Wetzel et al. (2012) showing the fraction of quenched galaxies in SDSS as a function of stellar mass. The results of this figure can be reproduced if galaxy quenching has an internal, stellar mass-driven component and an environmental, halo-mass driven component.

Chapter 2

Signatures of stellar accretion in MaNGA early-type galaxies

2.1 Introduction

The effective radii (R_e) of $z \sim 0$ early-type galaxies (ETGs) are observed to be a factor of three to six larger than those of their $z \sim 2$ counterparts (Toft et al. 2007; Cimatti et al. 2008; Buitrago et al. 2008; van Dokkum et al. 2010). On the other hand, the stellar masses (M_*) of local ETGs have only increased by a factor of two since $z \sim 2$ (Daddi et al. 2005; Trujillo et al. 2006a,b, 2007; Zirm et al. 2007; van der Wel et al. 2008; van Dokkum et al. 2008; Damjanov et al. 2009; Cassata et al. 2010, 2011). While galaxies quenched at later times tend to be larger, driving the average R_e upward (progenitor bias; e.g. Valentinuzzi et al. 2010; Carollo et al. 2013), this alone is not sufficient to explain size growth (e.g. Furlong et al. 2017). Late stellar accretion in spheroidal, or even disk configurations (Graham et al. 2015), appears to be required, especially at the high M_* end ($M_* > 10^{10.5} M_\odot$, e.g. Genel et al. 2018). Minor mergers have been shown to be particularly efficient at increasing the R_e of ETGs while keeping their M_* roughly constant (e.g. Bezanson et al. 2009; Hopkins et al. 2010a; Barro et al. 2013; Cappellari et al. 2013; Wellons et al. 2016).

These ideas are at the basis of the current cosmological picture for structure evolution at $z < 2$, in which massive systems accrete stellar envelopes from satellite galaxies (Oser et al. 2010, 2012; Johansson et al. 2012b; Moster et al. 2010; Furlong et al. 2017). In this framework, stars that formed within their host galaxies tend to dominate at the center, whereas accreted stars begin to do so in the outskirts ($R \sim 2R_e$; Rodriguez-Gomez et al. 2016) and in the lower surface brightness regions beyond $2R_e$ known as stellar halos (Zolotov et al. 2009; Tissera et al. 2013, 2014; Cooper et al. 2015). These stellar popula-

tions of different origin are usually referred to as *in-situ* and *ex-situ*, respectively. Several simulations have made predictions about observational signatures of the predicted radial transition from *in-situ* to *ex-situ* (e.g. Pillepich et al. 2014). Among stellar population tracers, stellar metallicity is expected to be one of the most sensitive to this transition (e.g. Cook et al. 2016).

In the absence of late-time minor mergers, the radial stellar metallicity profiles are predicted to be negative (Kobayashi 2004; Pipino et al. 2010; Taylor & Kobayashi 2017). This implies that the outer parts of ETGs tend to be more metal-poor than the inner parts. Albeit with significant variance (Lackner et al. 2012; Hirschmann et al. 2015), the deposition of accreted stars in the outskirts of galaxies induces flattening of the *in-situ* profile (Cook et al. 2016; Taylor & Kobayashi 2017). Since mergers are expected to have a larger effect on more massive systems, the resulting prediction is that the stellar metallicity profiles of ETGs are flatter toward higher M_*, especially in the stellar halos (Cook et al. 2016).

These theoretical predictions have motivated the search for observational signatures of stellar accretion. Using long-slit spectroscopy, Carollo et al. 1993 estimated the strength of metallicity-sensitive stellar absorption features as a function of galactocentric radius in 42 nearby galaxies. Though larger samples can be studied using photometric surveys (e.g. La Barbera et al. 2005, 2011; Tortora et al. 2010; Tortora & Napolitano 2012), spectroscopy is critical for breaking the age-metallicity degeneracy. More recently, studies of stellar populations in nearby galaxies have benefited from integral field unit (IFU) surveys like MASSIVE (Greene et al. 2013, 2015), CALIFA (Sánchez et al. 2012), SAMI (Allen et al. 2015), and MaNGA (Mapping Nearby Galaxies at Apache Point Observatory; Bundy

et al. 2015). In particular, MaNGA observations extend to the outskirts of galaxies (beyond 2 R_e), starting to probe the radii at which the signatures of minor mergers are predicted to appear (e.g. Cook et al. 2016).

Stellar metallicity profiles are typically characterized by radial gradients, estimated by fitting a linear form to the profile between the center and 1-2R_e (e.g. Zheng et al. 2017; Goddard et al. 2017b; Li et al. 2018). In agreement with simulations, the metallicity gradients of ETGs tend to be negative (e.g. Rawle et al. 2010; González Delgado et al. 2015; Roig et al. 2015). However, the dependence of the gradient slope on M_* remains unclear. Based on a sample of $\sim 10^3$ galaxies from the MaNGA survey, Zheng et al. (2017) find weak or no correlation between the gradients and M_*. Using data from the same survey, Goddard et al. (2017a) find that gradients are steeper with increasing M_*, although with low significance. Though also based on MaNGA, Li et al. (2018) find shallower gradients at higher central velocity dispersions ($\sigma_* > 100$km/s). There are several possible sources for these discrepancies, from stellar population synthesis approach (see Conroy 2013) to fitting method. Another important factor, as we show in this paper, is that the stellar metallicity profiles of ETGs are not well described by a linear fit.

In this work, we examine the full radial extent of metallicity profiles from spatially resolved spectroscopy of 1010 ETGs from MaNGA. We inform our interpretation of the stellar metallicity profiles by using results from hydrodynamical simulations (e.g. Cook et al. 2016; Rodriguez-Gomez et al. 2016; D'Souza & Bell 2018). This paper is structured as follows. In Section 2.2 we define our sample. In Section 2.3, we describe the stellar population fitting process with the codes FIREFLY (Wilkinson et al. 2017), pPXF (Cappellari

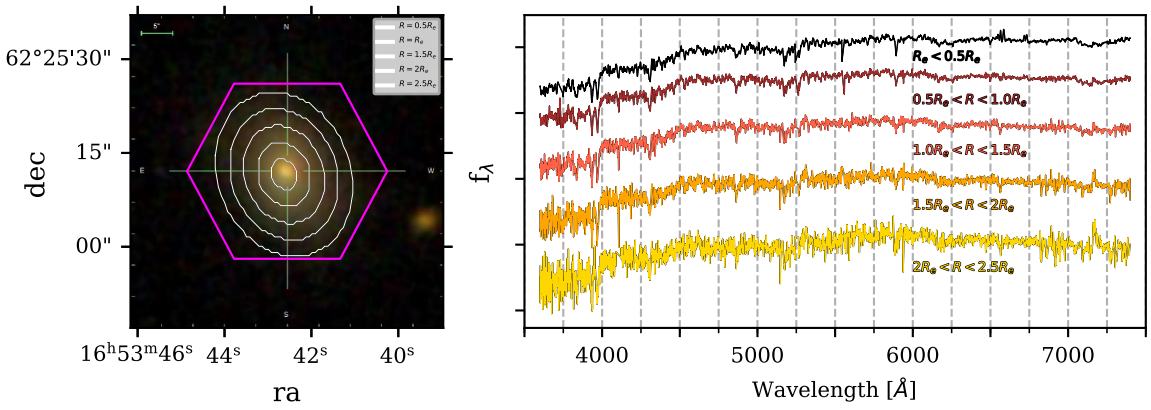

Figure 2.1: Illustration of our analysis on MaNGA galaxy 1-22298, one of 1010 ETGs in our sample. Left: SDSS r-band image. The MaNGA IFU footprint is overlaid in magenta. We also show in white the five annuli defined for this galaxy. Right: Co-added spectra for every annulus from the center to the outskirts.

& Emsellem 2004; Cappellari 2017), and Prospector (Leja et al. 2017). We show our results in Section 2.4 and discuss the implications in Section 2.5. We summarize in Section 2.6. This work adopts $H_0 = 70$ km s^{-1}Mpc^{-1} and all magnitudes are reported in the AB system (Oke & Gunn 1983).

2.2 Dataset

The MaNGA survey (Bundy et al. 2015; Yan et al. 2016a) is part of the fourth generation of SDSS (York et al. 2000; Gunn et al. 2006; Blanton et al. 2017), and is on track to provide spatially resolved spectra for ten thousand nearby galaxies ($z < 0.15$) by the end of 2020. By means of integral field unit spectroscopy (IFS; Smee et al. 2013; Drory et al. 2015; Law et al. 2015), every galaxy is observed with 19-to-127 fiber bundles with

diameters varying between 12.″5 and 32.″5. The resulting radial coverage reaches between $1.5R_e$ and $2.5R_e$ for most targets (Wake et al. 2017; see Figure 2.1). The spectra cover the wavelength range 3600-10300 Å at a resolution of R$\sim$2000.

All MaNGA data used in this work were reduced by the Data Reduction Pipeline (DRP; Law et al. 2016; Yan et al. 2016b). The reduced spectra have a median spectral resolution of σ=72 km s^{-1}. The data cubes typically reach a 10σ continuum surface brightness of μ=23.5 mag arcsec^{-2}, and their astrometry is measured to be accurate to 0.″1 (Law et al. 2016). De-projected distances and stellar kinematic maps have been calculated by the MaNGA Data Analysis Pipeline (DAP; Westfall et al. 2019). This work also makes use of Marvin (Cherinka et al. 2019), the specially designed tool for access and handling of MaNGA data[1].

This paper is based on the SDSS Data Release 15 (DR15), which consists of the observations of the first 4675 MaNGA targets. We extracted the stellar masses (M_*), Sersic indices ($n_{\rm Sersic}$), and effective radii (R_e) of these galaxies from the publicly available NASA-Sloan Atlas[2](NSA). In particular, the M_* estimates were derived using a k-correction fit to the Sersic fluxes (Blanton & Roweis 2007), adopting the Bruzual & Charlot (2003) stellar population models and a Chabrier (2003) initial mass function (IMF). They also assumed H_0 = 100 km s^{-1}Mpc^{-1}, but we scaled them for an H_0 = 70 km s^{-1}Mpc^{-1} cosmology. The $n_{\rm Sersic}$ estimates were obtained from one-component, two-dimensional fits to r-band images. The R_e are determined using an elliptical Petrosian analysis of the r-band image from the NSA. All NSA measurements use the detection and deblending technique described

[1]https://api.sdss.org/doc/manga/marvin
[2]http://nsatlas.org

in Blanton et al. (2011).

To select ETGs, we first applied the morphological cut $n_{\rm Sersic} > 2.5$ (e.g. Blanton et al. 2003, 2005a; Peng et al. 2010a). In addition, we selected passive ETGs by using the average Hα equivalent width across the galaxy -EW(Hα)- as proxy for specific star-formation rate (sSFR). The cut was EW(Hα) < 3 Å, which is commonly used to distinguish between ionization due to smooth background of hot evolved stars and due to star formation and AGN (Cid Fernandes et al. 2011; see also Belfiore et al. 2016). This yielded a sample with 1101 galaxies. We also limited the central velocity dispersions and stellar masses of our sample to the ranges $\sigma_* < 400$ km s^{-1} and 10 <logM/M$_*$ < 12, respectively. We performed these cuts to provide a relatively uniform distribution of ETGs over M$_*$. The final outcome was a sample of 1010 ETGs. We did not remove quiescent galaxies with significant stellar disks from the sample. From visual inspection, we estimate the fraction of lenticulars (S0s) to be $\lesssim 20$ %. However, we acknowledge the challenge of achieving precise S0 classification of SDSS galaxies (see Nair & Abraham 2010). Our selection may also miss blue ellipticals, but their number fraction is $\lesssim 5\%$ for our M$_*$ range (Kannappan et al. 2009). Our goal here is to study a generally passive sample of spheroidal galaxies. We delay to future work a characterization of stellar populations in more finely discriminated morphological types.

2.3 Methodology

2.3.1 Radial binning

Using the R$_{\rm e}$ value of every galaxy, we associated elliptical polar radii to all spaxels in units of R$_{\rm e}$. These account for the axis ratio of every object, which were measured on

the r-band photometry. We then binned them into the five annuli $R/R_e = [0, 0.5]$, $[0.5, 1]$, $[1, 1.5]$, $[1.5, 2]$, and $[2, 2.5]$. This is shown for a sample galaxy on the left panel of Figure 2.1.

After binning, we shifted every spectrum back to the rest-frame using the stellar systemic velocity (v_*) maps calculated by the DAP. We used the maps computed with a Voronoi binning scheme that aims for a minimum signal-to-noise ratio of 10 per bin. For each galaxy, we co-added the spectra in every annular bin. We did not convolve the spectra to a common σ_* prior to stacking. After co-addition, we ran pPXF (Cappellari & Emsellem 2004; Cappellari 2017) with the MILES Single Stellar Population (SSP) library (Vazdekis et al. 2010) on the stacked spectra to measure the co-added v_* and σ_*. The right panel of Figure 2.1 shows the five co-added spectra for a sample galaxy.

2.3.2 Stellar population fitting

Estimates of stellar population parameters like stellar metallicity can be obtained by full spectral fitting, but depend sensitively on the adopted priors, assumptions used to generate template spectra (Conroy 2013), and fitting method. To mitigate the effect of systematic biases from any one approach, we applied three independent codes to the same data and examine the differences that arise.

The first code we ran was the public version of FIREFLY[3][4](Comparat et al. 2017; Wilkinson et al. 2017; Goddard et al. 2017a). This χ^2 minimization code decouples stellar populations from dust by removing the low-order continuum shape before performing the

[3]FIREFLY - A full spectral fitting code http://www.icg.port.ac.uk/FIREFLY/

[4]https://github.com/FireflySpectra/firefly_release

model fitting. Hence, it focuses on high frequency modes in the spectra to infer stellar ages and metallicities. SSPs of different ages and metallicities are added iteratively until the improvement in χ^2 is negligible.

We ran the code with the stellar population models of Maraston & Strömbäck (2011), MILES stellar library (Sánchez-Blázquez et al. 2006), and Chabrier IMF (Chabrier 2003). We used a set of SSPs covering an age grid between 6.5 Myr and 15 Gyr, while the sampled stellar metallicities were $\log Z/Z_{\odot}$=-2.3, -1.3, -0.3, 0.0, and 0.3. The library spans the wavelength range 4000Å to 7400Å. As shown in Wilkinson et al. 2017, FIREFLY effectively recovers stellar population parameters for spectra with S/N$>$ 10 (see also Goddard et al. 2017b). To limit the systematics in the measurements from Firefly, we excluded any co-added spectra with S/N$<$ 10. We also masked emission lines. Fitting with FIREFLY took, on average, a minute per spectrum on a single core. Throughout this paper, we show light-weighted measurements, although we find similar results when using the mass-weighted counterparts.

We also ran pPXF[5](Cappellari & Emsellem 2004; Cappellari 2017) on our spectra. This code applies a penalized maximum likelihood approach to fit libraries of stellar population templates to observed data. Since this code penalizes pixels that are not well characterized by the templates, it minimizes template mismatch. We ran it with the included library of SSPs based on the MILES stellar library (Sánchez-Blázquez et al. 2006; Vazdekis et al. 2010).

We simultaneously fitted for the gas and the stars, allowing for two moments in

[5]pPXF
https://www-astro.physics.ox.ac.uk/ mxc/software/#ppxf

gas kinematics and four in stellar kinematics. We chose not to smooth the distribution of template weights (i.e., no regularization). After the best linear combination of templates was found, we added several realizations of the noise in the spectra to the best fit. This allowed us to characterize the uncertainties in the reported stellar population parameters. On average, our runs of pPXF took about a minute per spectrum on a single core.

The third stellar population fitting code we ran was Prospector[6](Leja et al. 2017). This code is based on the stellar population synthesis code FSPS[7](Conroy et al. 2009; Conroy & Gunn 2010), which generates composite stellar spectra for a variety of prescriptions for stellar population synthesis and evolution. This allows Prospector to sample the posterior distribution of a user-defined parameter space, while formally characterizing uncertainties and degeneracies. We chose the MILES stellar library (Sánchez-Blázquez et al. 2006), MIST isochrones (Dotter 2016; Choi et al. 2016), and Kroupa IMF (Kroupa 2001) as inputs. We also masked emission lines prior to fitting.

Since we fitted old stellar populations, we modeled the spectra with exponentially decaying (τ) star-formation histories to speed up the fitting process. In addition to τ, our parameter space included the optical depth of dust in the V-band, and stellar ages, metallicities, masses, and velocity dispersions. Our priors are shown in Table 2.1. To derive the posterior distributions, we used the Dynamic Nested Sampling package dynesty[8](Speagle 2019). On average, convergence of Prospector was achieved after an hour per spectrum.

[6]Prospector
https://github.com/bd-j/prospector/blob/master/doc/index.rst
[7]FSPS: Flexible Stellar Population Synthesis
https://github.com/cconroy20/fsps
[8]dynesty
https://github.com/joshspeagle/dynesty/blob/master/docs
/source/index.rst

Table 2.1: Priors used in the Prospector runs

Parameter	Prior
τ	LogUniform$(10^{-2}, 10)$
dust2	TopHat$(0, 1)$
Stellar age [Gyr]	TopHat$(5, 14)$
Stellar metallicity [log$Z/Z_{\odot}$]	TopHat$(-2, 0.3)$
Stellar mass [$M_{\odot}$]	LogUniform$(10^5, 10^{12})$
σ_* [km/s]	TopHat$(10, 400)$

Table 2.2: Total number of spectra used to derive the stellar metallicity profiles

$M_*[M_{\odot}]$	R<0.5R_e	0.5< $R[R_e]$ <1	1< $R[R_e]$ <1.5	1.5< $R[R_e]$ <2	2< $R[R_e]$ <2.5
$10^{10} - 10^{10.5}$	174 (174)	174 (174)	174 (174)	170 (170)	167 (160)
$10^{10.5} - 10^{11}$	267 (267)	267 (267)	266 (265)	264 (264)	252 (246)
$10^{11} - 10^{11.5}$	420 (420)	420 (420)	417 (417)	393 (392)	347 (319)
$10^{11.5} - 10^{12}$	148 (148)	147 (147)	142 (142)	114 (111)	88 (67)

Numbers apply to pPXF and Prospector; Firefly numbers are in parenthesis (cut of S/N> 10). The decrease in number of spectra with radius is a consequence of IFU coverage and quality cuts on the fits to stellar kinematics.

2.4 Results

Using the three codes described above, we derived stellar population parameters in each radial bin for all galaxies in the sample. After binning in M_* (with numbers in Table 2.2), we computed the average stellar metallicity profiles as a function of M_* and show them in Figure 2.2. The three panels show the results from the three fitting codes. While the metallicity profiles differ in normalization and in their detailed shapes, qualitative trends are similar across the codes.

We start by discussing the two notable discrepancies among the outputs. First, pPXF systematically measures metallicities ~ 0.1 dex lower than Firefly and Prospector. This overall offset does not correlate with S/N or M_* and will not affect our primary conclusions, which are based on the shape of derived metallicity profiles. Second, Firefly outputs tend to avoid metallicities in the range $\log Z/Z_\odot = [-1.3, -0.3]$, preferring higher values. This is presumably due to sampling in the stellar metallicity grid (see Wilkinson et al. 2017). As we show in Figure 2.2, flattening of the Firefly metallicity profiles occurs at higher metallicities as a result.

In nearly all radial bins, more massive galaxies exhibit more metal-rich stars. The $\log Z/Z_\odot$ profiles of ETGs fall linearly with galactocentric radius out to $1.5R_e$. Remarkably, the profiles flatten at the largest radii for $M_* > 10^{11} M_\odot$. The flattening is present in the output of all three codes. Comparing a given set of profiles as a function of M_*, we see that the radius at which this flattening occurs moves inward as M_* increases. These results are also apparent in the behavior of Lick indices Fe4531, Mgb(5178), and Fe5270 (Appendix 2.7). The observed flattening is consistent with the signatures of stellar accretion predicted

by hydrodynamical simulations (e.g. Cook et al. 2016) and motivates the interpretative framework we discuss in Section 2.5.

We note that even though the M_* dependence of the stellar metallicity profiles is consistent across codes, the same cannot be said about the stellar age profiles (not shown). This is not surprising, since it is extremely difficult to determine the ages of stellar populations older than 9 Gyr because of the slow isochrone evolution at late times (Conroy 2013). Since radial gradients in stellar age are not predicted to capture much information about the accretion history of ETGs (Cook et al. 2016), we leave a more detailed analysis of stellar ages for future work.

Some galaxies only satisfied our quality criteria (see Section 2.3) at some annuli. Hence, some galaxies contributed only to some regions in the profiles of Figure 2.2. To ensure our results are not biased, as a result we constructed a subset of 822 ETGs composed only of high quality spectra (S/N$>$ 10 for all radii). Our results were also recovered with this subset.

We have also attempted to reproduce our results using the publicly available Firefly[9] (Goddard et al. 2017a,b) and Pipe3D[10] (Sánchez et al. 2016, 2018) Value Added Catalogs, which provide spatially-resolved maps of stellar population properties for MaNGA galaxies. Unfortunately, Voronoi bins with S/N$<$10 dominate in the outermost low-surface brightness regions. Various tests have shown that stellar population codes are biased at S/N$<$10 (e.g. Wilkinson et al. 2017). As a result of these complications, we refrained from incorporating these catalogs in our analysis.

[9]MaNGA FIREFLY Value Added Catalog http://www.sdss.org/dr14/manga/manga-data/manga-FIREFLY-value-added-catalog/

[10]Pipe3D Value Added Catalog https://www.sdss.org/dr14/manga/manga-data/manga-pipe3d-value-

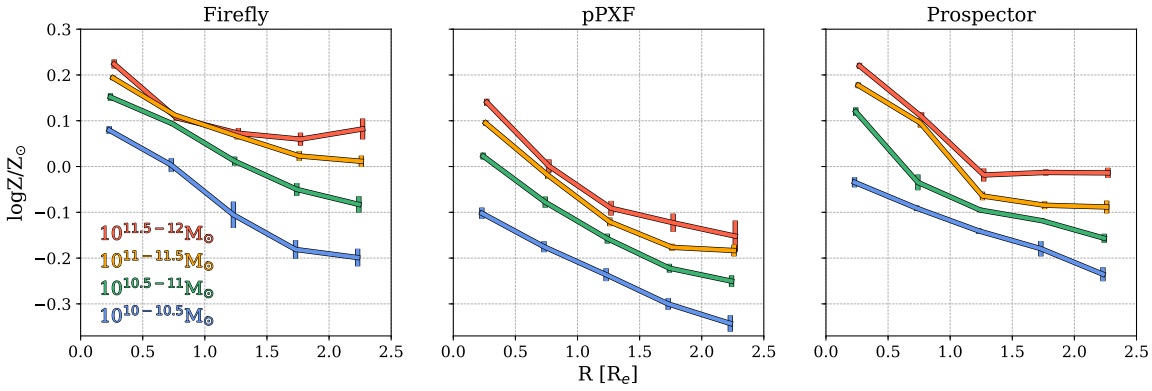

Figure 2.2: Median radial metallicity profiles of ETGs for different M_* bins. The three panels show the profiles derived by the codes Firefly, pPXF, and Prospector. The profiles of lower mass ETGs fall linearly with galactocentric radius. As galaxy mass increases, the profiles flatten at $R>1.5R_e$.

2.5 Discussion

2.5.1 On the radial metallicity profiles of ETGs

In the $R<R_e$ region, Martín-Navarro et al. (2018) found that the stellar metallicity profiles of ETGs fall more steeply at higher σ_* and M_*. Similarly, Goddard et al. (2017a) reported weak evidence for a steepening of their radial gradients with M_*. On the other hand, Kuntschner et al. (2010); Tortora et al. (2010); Kuntschner (2015); Li et al. (2018) found gradients to flatten at higher σ_*. González Delgado et al. (2015); Zheng et al. (2017) claimed no clear correlation between their stellar metallicity gradients and M_*. Similarly, Greene et al. (2013, 2015) found no strong correlations between the shape of element abundance profiles and σ_*. In this work, we found the profiles to flatten in the outskirts for $\log M_*/M_\odot \gtrsim 11$. Here, we demonstrate how some of the apparent disagreement among

added-catalog/

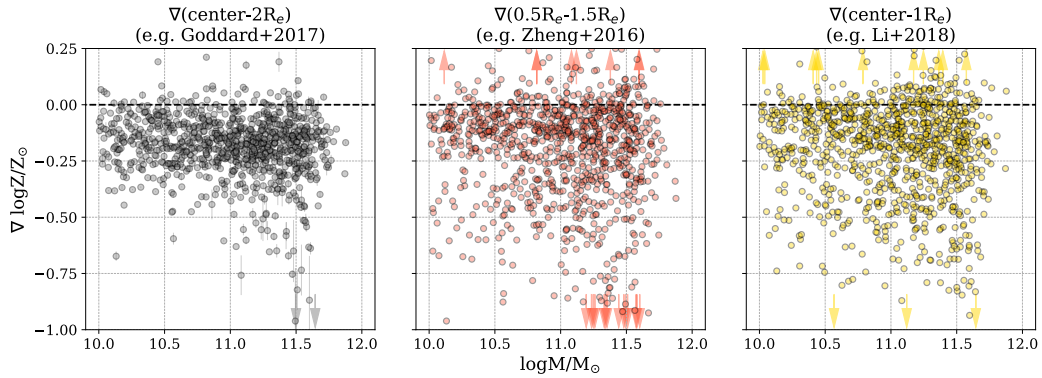

Figure 2.3: Radial metallicity gradients for our ETGs as a function of M_*. These gradients were computed by fitting a straight line to the radial profiles. From left to right, we fit the radial ranges $R<2R_e$, $0.5R_e<R<1.5R_e$, and $R<1R_e$. The arrows indicate gradients beyond the scale of the figure. Note how gradients fail to capture most of the high M_* flattening seen in Figure 2.2. This figure was made with the outputs from Prospector, but results stand for Firefly and pPXF.

observations may owe to the definition of metallicity gradients.

A quick look at our Figure 2.2 reveals that the average metallicity profiles of ETGs are not straight lines. It stands to reason that fitting lines to these radial profiles could "wash-out" the flattening in the outskirts of high M_* ETGs. Figure 2.3 shows the outcome of fitting lines to our metallicity profiles over different radial ranges motivated by the literature. Some ranges trace the inner regions ($R<R_e$; Li et al. 2018), while others have more extended coverage ($R<2R_e$; Goddard et al. 2017a). The scatter is considerable in all cases, and recovering any correlations with M_* is difficult. We conclude that gradients are sensitive to radial coverage (see also Greene et al. 2019) and can also miss important behavior in the stellar metallicity profiles. Gradients should be avoided when possible.

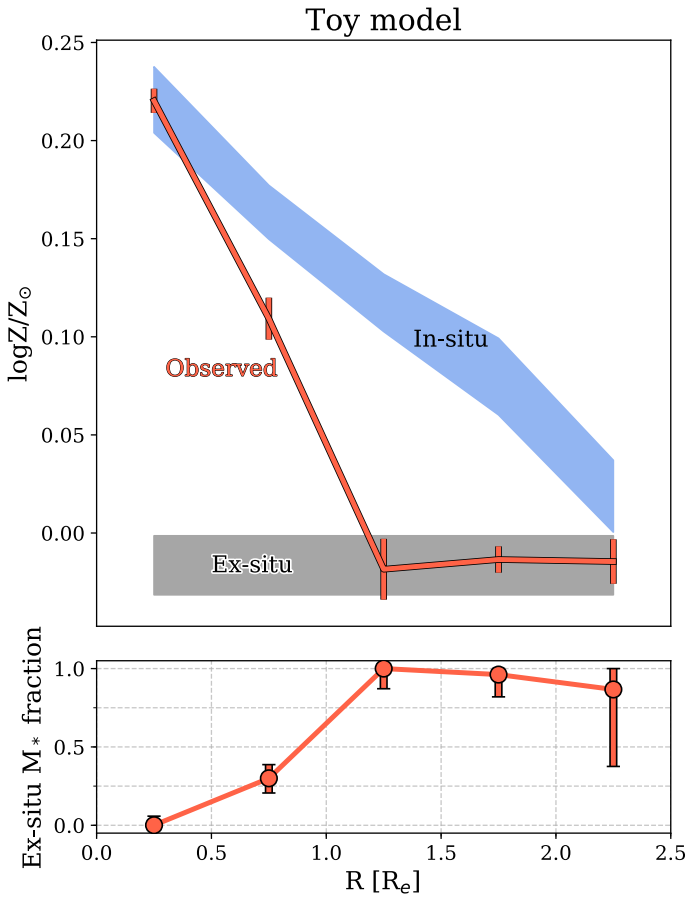

Figure 2.4: Top: Decomposition of the observed metallicity profile (red data points) in the highest M_* bin ($10^{11.5} - 10^{12} M_\odot$). We ascribe the *in-situ* component in this mass bin the same shape as the observed metallicity profile in the lowest M_* bin ($10^{10} - 10^{10.5} M_\odot$), but scaled upward to match the observed, central metallicity at higher M_*. The *ex-situ* component (grey) is ascribed a single metallicity $\varepsilon \sim -0.24$ lower than the observed central metallicity. The mix of components lowers the observed metallicity at all radii. Bottom: The amount of suppression determines the required fraction of *ex-situ* stars at each radius. This figure was made with the outputs from Prospector, but also applies to Firefly and pPXF.

2.5.2 Comparison with hydrodynamical simulations

Hydrodynamical simulations predict stellar accretion to induce gradient flattening (e.g. Cook et al. 2016). In general, stars accreted via dry, minor mergers tend to settle around and beyond the outskirts of ETGs (R=2-4R_e), which results in a flatter stellar metallicity profile than the inherently steeper form it originally had. Since mergers are expected to have a larger effect on more massive systems, this prediction is in broad agreement with our results from Figure 2.2.

A relevant point involves the radii at which accretion signatures are expected to appear. Rodriguez-Gomez et al. (2016) derived the accreted mass fraction of galaxies as a function of galactocentric radius in the Illustris simulation (Vogelsberger et al. 2014a,b). On average, this fraction increases with radius. It goes from zero at the center to unity at radii $R \gtrsim 5R_e$. This motivates the definition of the transition radius (R_T). It is defined as the galactocentric radius at which the M_* fraction of the *ex-situ* stellar component overtakes its *in-situ* counterpart (D'Souza et al. 2014). Rodriguez-Gomez et al. (2016) found R_T to decrease with M_*, going from $R_T \sim 5R_e$ at $M_* \sim 10^{10}M_\odot$ to $R_T < R_e$ at $M_* \sim 10^{12}M_\odot$. Our results are qualitatively consistent with this prediction.

However, there are some quantitative tensions. For $\log M_*/M_\odot \sim 11$ galaxies, Rodriguez-Gomez et al. (2016) reported $R_T \sim 4\ R_e$. Within $2.5R_e$, we should only be probing accreted stellar mass fractions of $\lesssim 0.3$ at this mass range. Cook et al. (2016), also based on the Illustris simulation, reported that the flattening of metallicity gradients with M_* only becomes noticeable in the stellar halo ($R = 2 - 4R_e$). Therefore, the signatures we see in Figure 2.2 are apparent at smaller radii than some simulations have predicted. There

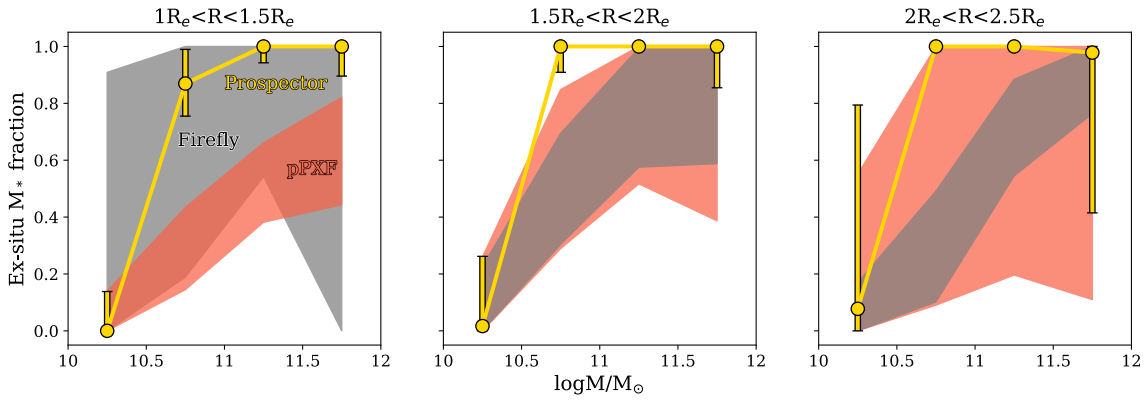

Figure 2.5: Observational estimate of the *ex-situ* stellar mass fraction in ETGs as a function of M_* for three different radial bins. Shown are the 1σ contours derived with Firefly (grey), pPXF (red), and Prospector (yellow). The estimates come from expressing the metallicity profiles of ETGs as a linear combination of *in-situ* and *ex-situ* profiles (Figure 2.4). Note how *ex-situ* signatures increase with M_*.

are a few possible explanations for this tension. The works of Rodriguez-Gomez et al. (2016); Cook et al. (2016) were based on Illustris. Galaxies at $z \sim 0$ from the first generation of this simulation were found to be larger by a factor of ~ 2 than observed galaxies. IllustrisTNG solved this problem, among others, by improving the treatment of galactic winds, magnetic fields, and black hole feedback (Pillepich et al. 2018; Weinberger et al. 2017, 2018). The treatment of these, among with other secular processes, can strongly impact the stellar population gradients measured in simulations (e.g. Taylor & Kobayashi 2017). On the observational side, estimates of the ages and metallicities of stellar populations can strongly depend on the choice of stellar library, isochrones, and approach to fitting. These systematic uncertainties also affect the conversion between stellar mass and stellar light, impacting the comparison between simulations and observations.

2.5.3 Estimating the *ex-situ* stellar mass fraction

Observationally, global stellar metallicity correlates with M_* or the central velocity dispersion σ_* of galaxies (Faber & Jackson 1976a; Cid Fernandes et al. 2005; Gallazzi et al. 2005; Thomas et al. 2005, 2010; González Delgado et al. 2014), as would be expected if the deeper potential wells of more massive systems limit the impact of galactic winds (Matteucci 1994). In the Illustris simulation, D'Souza & Bell (2018) found an accreted M_{acc}-Z_{acc} relation, where M_{acc} and Z_{acc} refer to the stellar mass and stellar metallicity of the accreted components, respectively. This relationship lies ~ 0.3 dex below the global counterpart. We can make informed assumptions for the *in-situ* stellar metallicity profile and the M_{acc}-Z_{acc} relation to build a toy model capable of inferring the *ex-situ* M_* fraction as a function of mass and galactocentric radius from our observations.

We assume the intrinsic *in-situ* metallicity profiles of ETGs to be well described by the profiles observed in the low mass end of our sample. This is supported by hydrodynamical simulations that find $M_* \sim 10^{10} M_\odot$ galaxies to be dominated by *in-situ* stars within the radial coverage of our data (Rodriguez-Gomez et al. 2016). We take the $M_* = 10^{10} - 10^{10.5} M_\odot$ profiles from Figure 2.2 for each code and refer to them as

$$\log Z_{obs}(R, \text{low } M_*) \tag{2.1}$$

In our model, the *in-situ* profiles of all galaxies follow the shape of $\log Z_{obs}(R, \text{low } M_*)$ with a normalization applied to match the metallicity at the center (i.e. within 0.5 R_e). This

can be written as

$$\log Z_{\text{in-situ}}(R, M_*) = \log Z_{\text{obs}}(R, \text{low } M_*) \tag{2.2}$$

$$+\log Z_{\text{obs}}(0.25R_e, M_*) - \log Z_{\text{obs}}(0.25R_e, \text{low } M_*)$$

with a schematic representation in Figure 2.4.

The M_{acc}-Z_{acc} relation is offset 0.3 dex from the global counterpart in the Illustris simulation. The existence of this relation originates from single massive progenitors contributing to the bulk of the mass to the accreted stellar component (D'Souza & Bell 2018). If we assume the accreted envelopes of ETGs to be comparable in stellar mass to their host ETG (e.g. Rodriguez-Gomez et al. 2016), *ex-situ* metallicities can be approximated by

$$\log Z_{\text{ex-situ}}(M_*) = \log Z_{\text{obs}}(0.25R_e, M_*) - \varepsilon \tag{2.3}$$

i.e., stellar metallicity of *ex-situ* stars will be $\varepsilon = 0.3$ dex lower than the metallicity at the center of the galaxy. Note that there is no dependence on galactocentric radius in the definition of $\log Z_{ex}$.

For measured metallicities, the offset will be dependent on the stellar population synthesis approach. To account for differences between codes, we set ε equal to the difference in metallicity between the centers and outskirts of $M_* = 10^{11.5} - 10^{12} M_\odot$ ETGs (see Figure 2.4). The corresponding values are $\varepsilon \sim -0.14$ (Firefly), -0.29 (pPXF), and -0.24 (Prospector).

We can now write observed metallicities as a linear combination between *in-situ*

and *ex-situ* metallicities:

$$\log Z_{\rm obs}(R,\, M_*) = f_{\text{in-situ}}(R,\, M_*)\, \log Z_{\text{in-situ}}(R,\, M_*)$$
$$+ f_{\text{ex-situ}}(R,\, M_*)\, \log Z_{\text{ex-situ}}(M_*) \tag{2.4}$$

where $f_{\text{in-situ}}$ and $f_{\text{ex-situ}} = 1 - f_{\text{in-situ}}$ are the *in-situ* and *ex-situ* fractions. Figure 2.4 describes our toy model and how we derive *ex-situ* fractions from it.

The results as a function of M_*, galactocentric radius, and code are shown in Figure 2.5. *Ex-situ* fractions increasingly dominate at larger radii and higher M_*. *Ex-situ* stars at R$\sim$2R$_e$ make up $\lesssim$20% of the projected stellar mass of $M_* \lesssim 10^{10.5} M_\odot$ ETGs, rising up to $\gtrsim$80% for $M_* \gtrsim 10^{11.5} M_\odot$ ETGs.

Stellar accretion and minor mergers provide an explanation for the size growth of spheroids from $z \sim 2$ to the present. Keeping in mind the simple nature of our comparison, we showed that the logZ profiles of nearby ETGs are consistent with this framework. However, this picture might not apply to S0s, which we visually estimate to compose $\lesssim$ 20% of our sample. The growth and accretion histories of S0s can differ from those of elliptical galaxies ($n_{\rm Sersic} > 2.5$; Blanton et al. 2003, 2005a; Peng et al. 2010a), as suggested by Johnston et al. (2012, 2014); Fraser-McKelvie et al. (2018); Saha & Cortesi (2018) (see also Diaz et al. 2018). Moreover, galaxy assembly history is not only expected to depend on the total M_* or morphology of galaxies, but also on their environment (e.g. Greene et al. 2015, 2019). We will study second order trends in the metallicity profiles of ETGs in follow-up work.

2.6 Summary

We characterized the radial stellar metallicity profiles of MaNGA ETGs and compared them with predictions from hierarchical formation. Through stellar population fitting with Firefly, pPXF, and Prospector, we found the following:

1. The three codes are built around different stellar population synthesis codes and are unique in their approach to fitting. Nonetheless, we found the main conclusions from this paper not to be dependent on the fitting code.

2. The profiles of $\log M_*/M_\odot \gtrsim 11$ ETGs fall with galactocentric radius and flatten beyond $R \sim 1.5 R_e$. Based on hydrodynamical simulations, a possible explanation for this flattening is stellar accretion through minor mergers.

3. The average radial metallicity profiles of ETGs are not linear. Therefore, linear fits can miss important behavior in the stellar metallicity profiles. When possible, fitting stellar population gradients should be avoided.

4. Using informed assumptions for the *in-situ* metallicity profile and the metallicity of accreted stars, we built a toy model to infer the *ex-situ* stellar mass fraction of ETGs. We found *ex-situ* signatures to grow in significance toward large galactocentric radii and higher M_*.

2.7 Appendix: Lick index profiles

Lick indices (Worthey et al. 1994; Thomas et al. 2003; Parikh et al. 2019) are a useful method to empirically estimate the chemical abundance patterns of galaxies. Here, we compute the radial profiles of Mgb(5178), Fe5270, and Fe5335 to test the high M_*

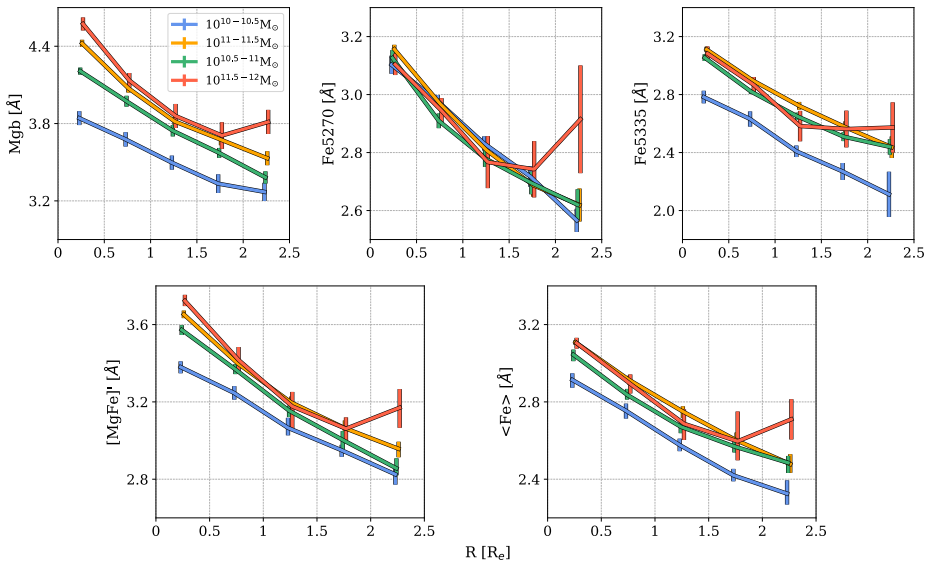

Figure 2.6: Median radial profiles of Mgb, Fe5270, Fe5335, [MgFe]', and <Fe> for MaNGA ETGs as a function of M_*. These profiles are based on measurements made by the MaNGA Data Analysis Pipeline. The profiles flatten at the highest M_*, in consistency with Figure 2.2.

flattening we find through stellar population fitting. We retrieved the indices measured by the MaNGA Data Analysis Pipeline and used them to compute:

$$[\text{MgFe}]' = \sqrt{\text{Mgb}(0.72 \times \text{Fe5270} + 0.28 \times \text{Fe5335})} \tag{2.5}$$

$$<\text{Fe}> = 0.5 \times \text{Fe5270} + 0.5 \times \text{Fe5335} \tag{2.6}$$

Here [MgFe]' and <Fe> are tracers of the global and Iron abundances (Johnston et al. 2018). We binned the measurements into the five annuli $R/R_e = [0, 0.5]$, $[0.5, 1]$, $[1, 1.5]$, $[1.5, 2]$, and $[2, 2.5]$ to derive the median profiles shown in Figure 2.5. Note how the profiles flatten for the highest M_* bin.

Chapter 3

How the stellar populations of passive central galaxies depend on stellar and halo mass

3.1 Introduction

The historical debate over spheroidal galaxy formation pitted an *in-situ* process (so-called "monolithic collapse," e.g. Eggen et al. 1962; Larson 1974; Arimoto & Yoshii 1987; Bressan et al. 1994) against an *ex-situ* one (so-called "hierarchical assembly," e.g. Toomre 1977; White & Rees 1978). More recently, this debate has been recast in the form of a proposed "two-phase" scenario that incorporates elements from both formation pathways (Oser et al. 2010, 2012; Johansson et al. 2012b). The question now is what physical processes, both *in-situ* and *ex-situ*, dominate and at what redshifts?

The two-phase formation scenario found particular motivation and success in explaining why, since $z \sim 2$, the M_* of passive spheroidal galaxies has apparently increased by only a factor of two (Toft et al. 2007; Cimatti et al. 2008; Buitrago et al. 2008; van Dokkum et al. 2010), while their effective radii (R_e) have increased by a factor of three to six (Daddi et al. 2005; Trujillo et al. 2006a,b, 2007; Zirm et al. 2007; van der Wel et al. 2008; van Dokkum et al. 2008; Damjanov et al. 2009; Cassata et al. 2010, 2011; van der Wel et al. 2014). After an initial phase that forms the "red nuggets" observed at $z \sim 2$ (van Dokkum et al. 2009; Newman et al. 2010; Damjanov et al. 2011; Whitaker et al. 2012; Dekel & Burkert 2014), the second evolutionary phase involves stellar accretion through minor mergers which preferentially adds *ex-situ* stars to the outskirts (e.g. Zolotov et al. 2009; Hopkins et al. 2010a; Tissera et al. 2013, 2014; Cooper et al. 2015; Rodriguez-Gomez et al. 2016). It has been shown that such accretion efficiently increases R_e while keeping M_* roughly constant (e.g. Bezanson et al. 2009; Barro et al. 2013; Cappellari et al. 2013; Wellons et al. 2016).

Direct support of this picture comes from studies of the surface brightness profiles of massive nearby galaxies that almost always feature multiple components (e.g. Huang et al. 2013b). Their inner parts ($R < 1$ kpc) are very compact and populate the same region of the mass-size plane as massive $z > 1$ galaxies (Huang et al. 2013a). In contrast, their outer envelopes can be quite extended ($R > 10$ kpc) and are consistent with being built through minor mergers (Huang et al. 2013a). These outer envelopes can also show greater ellipticity than the inner parts, potentially reflecting the orbital properties of accreted satellites (Huang et al. 2018).

In Oyarzún et al. (2019), we applied a different test of the two phase formation scenario by searching for the predicted flattening of the stellar metallicity profile that is expected from the accretion of lower mass galaxies (e.g. Cook et al. 2016; Taylor & Kobayashi 2017). Using a sample of early-type galaxies (ETGs) from the MaNGA survey (Bundy et al. 2015), we detected a flattening beyond R_e in the otherwise declining metallicity profiles. This flattening grows more prominent with increasing M_*, especially for ETGs with $M_* > 10^{11} M_\odot$. This observation not only suggests that massive ETGs assembled their outskirts through minor mergers, but also that their *ex-situ* stellar mass fraction is higher, in agreement with theoretical predictions (Rodriguez-Gomez et al. 2016).

With mergers and stellar accretion driving the second phase of spheroidal galaxy evolution, it is natural to search for a link between passive centrals and their host halo environments, given that those environments determine the central galaxy's merger history (e.g. Hopkins et al. 2010b). Unfortunately, searches for signatures of environment-driven growth in spatially resolved surveys have been so far inconclusive. Santucci et al. (2020)

compared the stellar population gradients of central and satellite galaxies in the SAMI survey (Allen et al. 2015) at fixed M_* and found no significant differences. In initial efforts with MaNGA data, Zheng et al. (2017); Goddard et al. (2017a,b) studied the stellar age and metallicity gradients of massive galaxies and found no significant correlation with the local environment or different proxies for the large scale structure. The consensus of recent work is that at fixed M_*, the stellar populations of massive galaxies within $\sim$1 R_e are largely determined by their *in-situ* formation histories rather than their environment (Peng et al. 2012; Greene et al. 2015; Goddard et al. 2017b; Scott et al. 2017; Contini et al. 2019; Bluck et al. 2020).

In this paper, we return to the important question of *in-situ* versus *ex-situ* evolution in passive galaxies. By adopting the perspective of the stellar-to-halo mass relation, as defined for central galaxies (SHMR; Moster et al. 2013), we re-frame the question as a search for secondary correlations in the stellar populations of passive centrals as a function of halo mass (M_h) at fixed stellar mass (M_*), as well as correlations with M_* at fixed M_h. The first characterization allows us to revisit the role of environment, as expressed by M_h, in modulating galaxy formation at fixed M_*. The second lets us ask, to what extent does M_h determine the fate of a central galaxy?

This latter question is significant because theoretical models ultimately tie galaxy properties to their dark matter halos. Deviations, especially in the intrinsic scatter of the SHMR, have garnered a lot of interest and motivated work on "galaxy assembly bias," the possible existence of correlations between galaxy and secondary halo properties at fixed M_h (e.g. Zentner et al. 2014; Wechsler & Tinker 2018; Xu & Zheng 2020). According to the

theory, galaxy luminosity correlates with halo formation time and concentration at fixed M_h (Croton et al. 2007; Matthee et al. 2017; Kulier et al. 2019; Xu & Zheng 2020). More concentrated halos, for example, facilitate the formation of deeper potential wells that may promote a more rapid assembly of M_* (Booth & Schaye 2010; Matthee et al. 2017; Kulier et al. 2019). Gas accretion and star formation should commence earlier in halos that formed early for their M_h (Kulier et al. 2019). Yet, it remains unclear whether these predicted differences in halo and galaxy assembly history have an impact on the nature of the stellar populations across the SHMR as observed today.

To make progress on these questions and begin to delineate subtle secondary correlations between M_* and M_h, we construct an updated catalog of 2200 passive centrals drawn from the MaNGA survey. Previous work has emphasized the importance of $\sim$1% level or better precision in measuring stellar age and abundances in ETG spectra (e.g. Conroy et al. 2014). Galaxy-integrated spectra in our sample can exceed signal-to-noise (S/N) ~ 100 per galaxy, making MaNGA the premiere data set for co-added spectral analyses of nearby galaxies at this level of precision. The S/N from stacking all single-fiber ETG spectra in the SDSS MAIN Galaxy Survey (York et al. 2000; Gunn et al. 2006; Alam et al. 2015) would be a factor 0.6 times lower than the equivalent from the MaNGA stack. Equally important, the MaNGA data allow for simultaneous spatially-resolved measurements, allowing for consistency checks across radial bins. Our high S/N sample allows us to first detect subtle spectral differences in a model-free manner and then employ sophisticated full spectral fitting codes like `Prospector` and `alf` for the interpretation (Leja et al. 2017; Johnson et al. 2020; Conroy & van Dokkum 2012; Conroy et al. 2018). These codes model

the non-linear response of spectral features (Conroy 2013) to infer the age, abundance of various elements, and initial mass function (IMF) of old stellar systems ($\gtrsim$1 Gyr), while also accounting for uncertainties in stellar evolution.

We also pay close attention to the impact of systematic errors on our results from potential biases in the M_h estimates. We are unfortunately limited in this study to halo estimates from group finding algorithms, which must first distinguish centrals from satellites and then require total M_* measurements of all group members (e.g. Yang et al. 2005, 2007). Group catalogs often fail to reproduce the fractions of red and blue satellites, the dependence of the stellar-to-halo mass relation for centrals (SHMR) on galaxy color, and correlations between M_h and secondary galaxy properties (Tinker 2020a). We address these concerns by utilizing the new SDSS halo catalog in Tinker (2020a,b), which exploits deep photometry from the DESI Legacy Imaging Survey (Dey et al. 2019). Tinker (2020a) also implement a group finding algorithm that is calibrated on observations of color-dependent galaxy clustering and estimates of the total satellite luminosity. As a result, their catalog better reproduces the color-dependent satellite fraction of galaxies and improves on the purity and completeness of central galaxy samples. In this work, we use the M_h estimates by Tinker (2020a,b) and compare them against those by Yang et al. (2005, 2007), allowing us to assess how sensitive our results are to systematics in halo catalogs.

This paper is structured as follows. In Section 3.2, we introduce our dataset and sample of passive central galaxies. In Section 3.3, we describe our treatment of the spectra and the stellar population fitting process. In Section 3.4, we show the results from direct spectral comparison and stellar population fitting. We interpret our findings in Section 3.5

and summarize in Section 3.6. Stellar masses throughout were obtained assuming a Kroupa (2001) IMF. This work adopts $H_0 = 70$ km s^{-1}Mpc^{-1} and all magnitudes are reported in the AB system (Oke & Gunn 1983).

3.2 Dataset

3.2.1 The MaNGA survey

The MaNGA survey (Bundy et al. 2015; Yan et al. 2016a) is part of the now complete fourth generation of SDSS (York et al. 2000; Gunn et al. 2006; Blanton et al. 2017; Aguado et al. 2019) and obtained spatially resolved spectra for more than ten thousand nearby galaxies ($z < 0.15$). By means of integral field unit spectroscopy (IFS; Drory et al. 2015; Law et al. 2015), every galaxy was observed with fiber bundles with diameters varying between $12\farcs5$ and $32\farcs5$ and composed of 19 to 127 fibers. The resulting radial coverage reaches between $1.5R_e$ and $2.5R_e$ for most targets (Wake et al. 2017). The spectra cover the wavelength range 3600-10300 Å at a resolution of R$\sim$2000 (Smee et al. 2013). The reduced spectra have a median spectral resolution of σ=72 km s^{-1}.

All MaNGA data used in this work was reduced by the Data Reduction Pipeline (DRP; Law et al. 2016, 2021; Yan et al. 2016b). The data cubes typically reach a 10σ continuum surface brightness of 23.5 mag arcsec^{-2}, and their astrometry is measured to be accurate to $0\farcs1$ (Law et al. 2016). De-projected distances, stellar kinematics, and spectral index maps were calculated by the MaNGA Data Analysis Pipeline (DAP; Belfiore et al. 2019; Westfall et al. 2019). This work also used Marvin (Cherinka et al. 2019), the tool

specially designed for access and handling of MaNGA data[1].

Effective radii (R_e) for all MaNGA galaxies are publicly available as part of the NASA-Sloan Atlas[2](NSA). These R_e were determined using an elliptical Petrosian analysis of the r-band image from the NSA, using the detection and deblending technique described in Blanton et al. (2011).

3.2.2 Selection of passive galaxies

This paper is based on the MaNGA Product Launch 11 (MPL-11) dataset, which consists of observations for over 10,000 MaNGA targets (see Table 1 in Law et al. 2021 for reference on the various release versions). To select passive galaxies, we used estimates of the spatially integrated specific star-formation rate (sSFR) of MaNGA galaxies derived as part of the pipeline for the pipe3D Value Added Catalog for DR17[3]. We defined our sample of passive galaxies by setting the criterion $\log(\mathrm{sSFR}) < -11.5\ \mathrm{M}_{\odot} yr^{-1}$.

Our approach yielded a subset with 3957 passive galaxies, of which 2217 are identified as centrals in the catalog by Tinker (2020a,b) and 952 in the Yang et al. (2007); Wang et al. (2016) catalog. Details on the environmental classification are presented in Section 3.2.4.

[1]https://www.sdss.org/dr15/manga/marvin/

[2]http://nsatlas.org

[3]https://www.sdss.org/dr17/manga/manga-data/manga-pipe3d-value-added-catalog/. These sSFRs are based on measurements of the Hα equivalent width that were corrected by dust attenuation using the Balmer decrement (Sánchez et al. 2016)

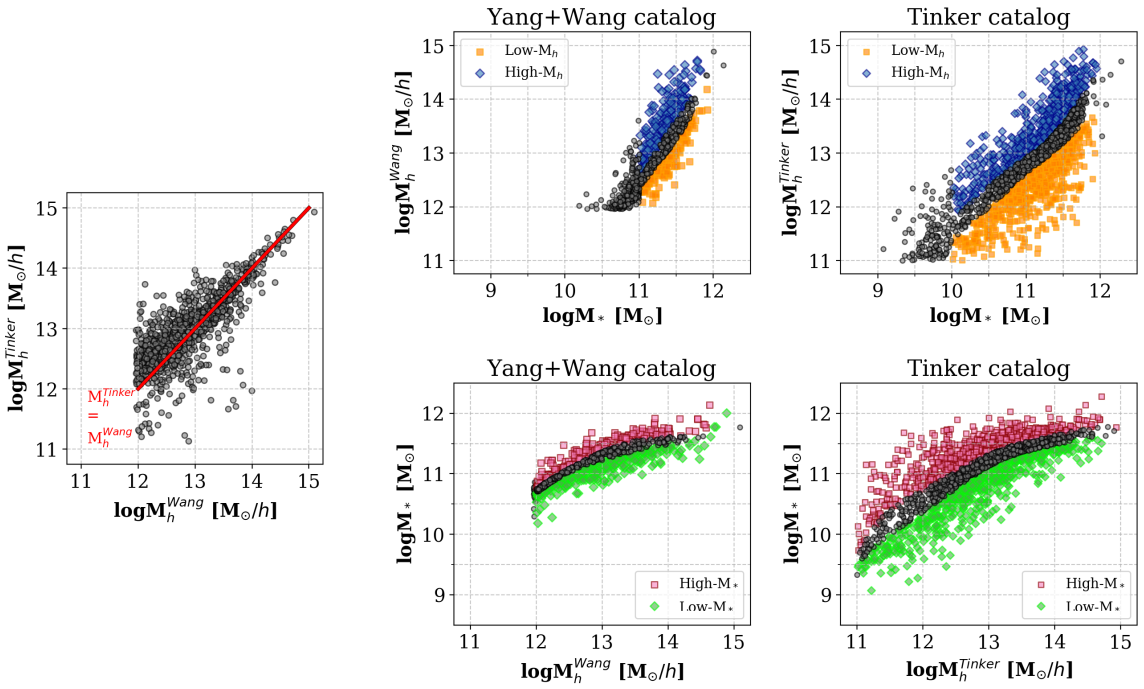

Figure 3.1: Comparison between the M_h measured by Wang et al. (2016) and Tinker (2020b) for our passive centrals. The $M_h^{\rm Wang}$ =$M_h^{\rm Tinker}$ line is shown in red. **Right:** Stellar-to-halo mass relation for passive centrals in the two catalogs. We define our subsamples based on the independent property and stellar-to-halo mass ratio. At fixed M_* (upper panels), high-M_h centrals are shown in blue and low-M_h centrals in orange. At fixed M_h (lower panels), high-M_* centrals are shown in red and low-M_* in green. Galaxies in regions of the SHMR with narrow dynamic range were not included in the analysis (gray). We also excluded galaxies between the 33rd and 66th percentiles in M_*-to-M_h ratio.

Table 3.1: Number of passive centrals in MaNGA as a function of stellar and halo mass

M_* [$M_\odot$]=	$10^{10} - 10^{10.5}$	$10^{10.5} - 10^{11}$	$10^{11} - 10^{11.5}$	$10^{11.5} - 10^{12}$	Out	Total
Wang	7	267	523	153	2	952
Wang low-M_h	0	0	174	48	-	222
Wang high-M_h	0	0	172	51	-	223
Tinker	211	514	948	412	132	2217
Tinker low-M_h	70	188	317	128	-	703
Tinker high-M_h	70	143	353	148	-	714

M_h [$M_\odot/h$]=	$10^{11} - 10^{12}$	$10^{12} - 10^{13}$	$10^{13} - 10^{14}$	$10^{14} - 10^{15}$	Out	Total
Wang	27	517	358	49	1	952
Wang high-M_*	0	172	113	15	-	300
Wang low-M_*	0	170	120	19	-	309
Tinker	329	888	860	139	1	2217
Tinker high-M_*	112	310	301	50	-	773
Tinker low-M_*	109	297	265	45	-	716

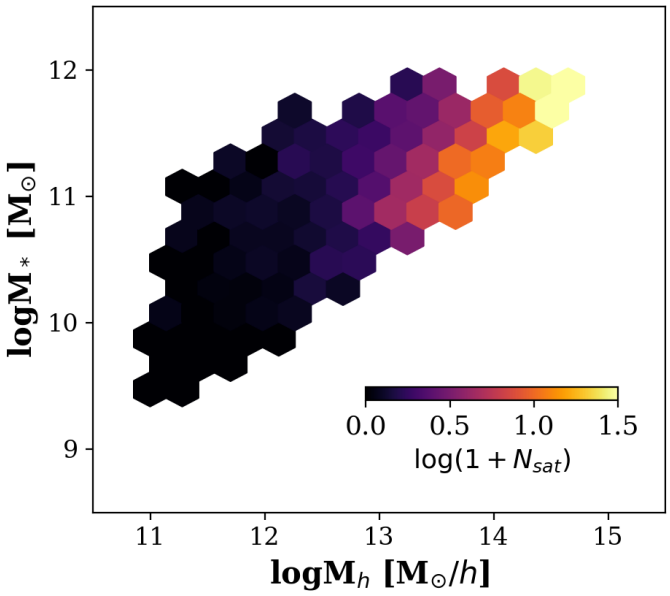

Figure 3.2: Number of satellite galaxies per halo as a function of M_h and M_* in the Tinker (2020a,b) catalog. At fixed M_*, centrals in high-M_h halos tend to have more satellites than centrals in low-M_h halos.

3.2.3 Stellar masses

To estimate the M_* of our galaxies, we first co-added the MaNGA spectra within the R_e of every galaxy (measured on r-band imaging from SDSS). Before co-addition, we shifted every spectrum back to the rest-frame using the stellar systemic velocity (v_*) maps calculated by the DAP. Then, we estimated the mass within $1R_e$ by running the stellar population fitting code `Prospector` (Leja et al. 2017; Johnson et al. 2020) on the co-added spectrum. Our runs adopted the MILES stellar library (Sánchez-Blázquez et al. 2006), MIST isochrones (Dotter 2016; Choi et al. 2016), and Kroupa (2001) IMF. Further details on our `Prospector` runs are presented in Section 3.3.4.

We then assumed the total spectroscopic stellar mass of every galaxy to be

$$M_*^{total} = 2M_*^{R_e} \times 10^{-0.15}, \tag{3.1}$$

where $M_*^{R_e}$ is the spectroscopic stellar mass within the effective radius measured with `Prospector`. Since it has been found that half-mass radii are smaller than half-light radii (García-Benito et al. 2017), our M_*^{total} may be overestimated. Yet, we do not expect any biases to arise from this definition, since differences between half-mass and half-light radii have not been found to correlate with stellar mass (Szomoru et al. 2013). Any overestimation of our stellar masses was corrected by implementing an offset of 0.15 dex (see the multiplicative term in the equation). This value was obtained by measuring the offset between our $2M_*^{R_e}$ and the stellar masses measured through k-correction fits to the Sersic fluxes in the NSA (Blanton & Roweis 2007). For the rest of the paper, we will simply refer to M_*^{total} as M_*.

3.2.4 Yang+Wang halo masses

For our first characterization of environment, we used the MPL-9 version of the Galaxy Environment for MaNGA Value Added Catalog[4] (GEMA-VAC; Argudo-Fernández et al. 2015). We used this catalog to identify central galaxies and retrieve estimates of their halo masses. The environmental classification and halo mass entries were computed by cross-matching MaNGA MPL-9 with the Yang et al. 2007 group catalog for SDSS (see also Yang et al. 2005). The halo masses computed by Yang et al. 2007 assumed a WMAP3 cosmology (Spergel et al. 2007). In this work, we use the values in the GEMA-VAC that were updated to a WMAP5 cosmology (Dunkley et al. 2009) as part of the work by Wang et al. (2009, 2012, 2016).

The group catalog by Yang et al. (2007) was computed on the SDSS New York University Value-Added Galaxy Catalog (NYU-VAGC; Blanton et al. 2005b) based on SDSS DR4 (Adelman-McCarthy et al. 2006). To compute the Yang et al. (2007) catalog, a series of steps were iterated until convergence was achieved. First, clustering analysis in redshift space was used to find potential cluster centers and groups. In the second step, group luminosities ($L_{19.5}$) were computed as the combined luminosity of all group members with $M_r - 5\log h \leqslant -19.5$ (hence the subscript in $L_{19.5}$). Dark matter halo masses, sizes, and velocity dispersions were then estimated. In particular, tentative M_h were assigned according to the $L_{19.5}$-M_h relation measured in the previous iteration, which assumes a one-to-one correspondence between $L_{19.5}$ and M_h. Finally, membership probabilities in redshift space around group centers were estimated. This allowed for group memberships to update.

[4]https://www.sdss.org/dr15/data_access/value-added-catalogs/?vac_id=gema-vac-galaxy-environment-for-manga-value-added-catalog

The process from the second to the final step was repeated until no further changes in group memberships were observed. After convergence, final M_h were derived through abundance matching using the van den Bosch et al. (2007) halo mass function.

Of the 3957 passive galaxies in our sample, 952 are centrals with halo mass measurements in the GEMA-VAC (see Figure 3.1). The SHMR using the stellar masses from Section 3.2.3 and the halo masses from the Yang+Wang catalog is plotted in Figure 3.1. Details on the number of galaxies as a function of M_* and M_h are shown in Table 3.1.

3.2.5 Tinker halo masses

Group finding algorithms, like the one described in Section 3.2.4, are affected by several issues. By not breaking down galaxy samples into star-forming and quiescent subsamples, they can fail to reproduce the fraction of quenched satellite galaxies and misestimate by an order of magnitude M_h (Campbell et al. 2015). Some of these shortcomings can be tackled by calibrating the free parameters of the group finder with real data instead of mock catalogs. In this paper, we work with the group finder by Tinker (2020a), which uses observations of color-dependent galaxy clustering and total satellite luminosity for calibration.

In the self-calibrating halo-based galaxy group finder by Tinker (2020a), the probability of a galaxy being a satellite depends on galaxy type and luminosity. This dependence is quantified by 14 different parameters that are calibrated until the best-fitting model is found. First, a starting value for the parameters is adopted and the group finder is run until the fraction of red and blue satellites match the input dataset. The assigned groups and halo masses are then used to populate the Bolshoi-Planck simulation (Klypin et al.

2016) and predict galaxy clustering and the total satellite luminosity. These predictions are compared to observational measurements to quantify the adequacy of the model. The process is then repeated until the best-fitting model is found.

This algorithm was applied to SDSS galaxies in Tinker (2020b). Compared to the dataset available to Yang et al. (2005, 2007), Tinker (2020b) had access to deeper photometry from the DESI Legacy Imaging Survey (DLIS; Dey et al. 2019). This is quite important, since good accounting of group and galaxy M_* is key to properly constraining M_h (Bernardi et al. 2013; Wechsler & Tinker 2018). As a result, the SDSS group catalog by Tinker (2020b) is an improvement in both dataset and algorithm.

Despite improvements, the approach by Tinker (2020a) still has limitations. Like all group finding algorithms, it is susceptible to central galaxy mis-identification. It also assumes that the amount of light in satellite galaxies is a function of halo mass only and its implementation on SDSS data fails to match the clustering of faint quiescent galaxies (Tinker 2020b). There is also room for further freedom in how the algorithm fits the data, in particular for taking into account secondary correlations between galaxy and halo properties (Tinker 2020b).

The self-calibrating halo-based galaxy group finder applied to SDSS is publicly available[5]. We downloaded the catalog and cross-matched with our sample of quenched systems. We selected all galaxies with satellite probabilities lower than 0.1 and obtained a sample with 2217 passive central galaxies (see Table **??**). The M_h measured by Tinker and Yang+Wang are compared in the left panel of Figure 3.1. The right panel shows the SHMR using our M_* and $M_h^{\rm Tinker}$, which extends down to $M_* \sim 10^{10} M_\odot$ ($M_h^{\rm Tinker} \sim 10^{11} h^{-1} M_\odot$).

[5]https://galaxygroupfinder.net

Figure 3.2 shows that the average number of satellites per halo monotonically increases with $M_h^{\rm Tinker}$.

3.3 Methodology

3.3.1 Sample definitions

The correlation between the M_* and M_h of central galaxies has significant scatter, some of which is thought to be intrinsic (e.g. Xu & Zheng 2020). This would imply that the stellar masses of central galaxies are not uniquely determined by the mass of their halos, but also by secondary properties (e.g. Zentner et al. 2014). In consequence, the SHMR is a very useful tool for testing the mechanisms driving the galaxy-halo connection (e.g. Leauthaud et al. 2017). The purpose of this work is to probe these mechanisms through the analysis of galaxy stellar populations.

Figure 3.1 shows the SHMR for our sample of centrals according to both environmental catalogs. We computed the 33rd and 66th percentiles in M_*-to-M_h ratio as a function of M_* to define two subsamples. High-M_h centrals are those that reside in high M_h for their M_* and are shown in blue. Low-M_h centrals, on the other hand, reside in low M_h halos for their M_* and are shown in orange. In equation form,

$$\text{High-M}_h \text{ sample: } \frac{M_*}{M_h}(M_*) < \left[\frac{M_*}{M_h}(M_*)\right]_{.33} \tag{3.2}$$

$$\text{Low-M}_h \text{ sample: } \frac{M_*}{M_h}(M_*) > \left[\frac{M_*}{M_h}(M_*)\right]_{.66}. \tag{3.3}$$

To quantify correlations at fixed M_h, we also computed the 33rd and 66th per-

centiles in M_*-to-M_h ratio as a function of M_h. High-M_* centrals have high M_*-to-M_h ratios, whereas low-M_* centrals have low M_*-to-M_h ratios. Put in an equation,

$$\text{High-M}_* \text{ sample: } \frac{M_*}{M_h}(M_h) > \left[\frac{M_*}{M_h}(M_h)\right]_{.66} \tag{3.4}$$

$$\text{Low-M}_* \text{ sample: } \frac{M_*}{M_h}(M_h) < \left[\frac{M_*}{M_h}(M_h)\right]_{.33}. \tag{3.5}$$

Galaxies between the 33rd and 66th percentiles in M_*-to-M_h ratio were not used and are shown as gray points in Figure 3.1. Since the distribution of centrals in M_*-to-M_h ratio as a function of M_* or M_h is rather flat, no subsample is biased as a result of uncertainties in M_* or M_h. Note that the sample membership of a given galaxy depends on the environmental catalog, since our classification scheme is based on M_h. The number of galaxies in every M_* and M_h bin for the two environmental catalogs is presented in Table 3.1. Due to the narrow dynamic range in M_h with the Yang+Wang catalog for $M_* < 10^{11} M_\odot$, the corresponding bins were not included in the analysis (see Table **??**). The average number of satellites per halo (N_{sat}) for every subsample is plotted in Figure 3.2. At fixed M_*, N_{sat} correlates with M_h.

3.3.2 Co-addition and stacking of spectra

The spectral precision needed by our stellar population analysis requires high signal-to-noise (S/N$\gtrsim$ 50) spectra (e.g. Conroy et al. 2014). Thus, we first co-added the MaNGA spectra within every galaxy following a radial binning scheme. We then computed the median of these co-additions to generate galaxy stacks for every subsample. The co-addition and stacking steps are described below.

For every galaxy, we associated galactocentric distances to all spaxels by retrieving elliptical polar radii (R) from the DAP that account for the axis ratio of every object. We binned all the spaxels within every galaxy into the three annuli $R = [0, 0.5]$, $[0.5, 1]$, and $[1, 1.5]$ R_e. After masking sky line residuals and spectra outside the wavelength range (3700Å, 9200Å) in the observed frame, the co-added spectra in every bin were co-added. To do this, we shifted every spectrum back to the rest-frame using the stellar systemic velocity (v_*) maps computed by the DAP with a Voronoi binning scheme that aims for a minimum signal-to-noise ratio of 10 per bin. We did not convolve the spectra to a common σ_* prior to stacking. We also masked all spaxels that were flagged as unusable by the DRP and DAP.

After co-addition, we ran pPXF (Cappellari & Emsellem 2004; Cappellari 2017) with the MILES Single Stellar Population (SSP) library (Vazdekis et al. 2010) on the resulting spectra to measure the co-added v_* and σ_*. Co-added v_* showed values $v_* \lesssim 1$ km/s, indicating that spectra were properly shifted back to the rest-frame. We also ran `Prospector` (details in Section 3.3.4) to measure stellar mass surface density profiles for every galaxy.

After binning in M_* and M_h (see Table 3.1), we stacked the spectra across every subsample in each of the four radial annuli. For stacking, all co-added spectra were convolved to $\sigma_* = 350\ kms^{-1}$ and median normalized. This value is motivated by the maximum observed dispersion, and it mitigates line-strength variations caused by different Doppler broadening. Stacks were obtained by computing the median at each wavelength after removing the continuum. Errors on the stacks were quantified through Monte Carlo simulations of the stacking process that took into account the propagated errors. Two stacked spectra

are shown in Figure 3.3 after all emission lines were masked. The dependence of the stacks on whether masking is performed before or after stacking is minimal.

Appendix 3.7 shows stacked spectra at multiple radii and M_h. We typically reach $S/N > 200$ at the centers and $S/N > 100$ in the outskirts. We find the spectral S/N of the stacks to show dependence on both the individual S/N and the total number of spectra. As a result, the highest M_* and M_h stacks show the lowest spectral S/N of all bins by factors of ~ 2.

3.3.3 Evidence for environmental differences

The top panel of Figure 3.3 compares the stacked spectra at the centers of high- and low-M_h centrals with $M_* = 10^{10} - 10^{10.5} M_\odot$. With M_* held constant (see Section 3.3.1), any differences between the spectra in this comparison can be interpreted as environmental signatures. In this subsection, we describe our method to finding and highlighting these signatures.

We started by subtracting high-M_h stacks from low-M_h counterparts of the same M_*. An example of the resulting spectral difference is shown in the middle panel of Figure 3.3. Then, to highlight variations in spectral features, we subtracted fits from the spectral differences. The result is shown in the bottom panel of Figure 3.3. Note how the spectral difference captures variations in both spectral shape and features. As we will show in Section 3.4, we find some significant environmental signatures at different M_* and radii. This is evidence that M_h has an impact on the stellar populations of passive central galaxies at fixed M_*.

For context, some abundance sensitive features are labeled in this figure. Difference

at these locations highlight the fact that environmental signatures can manifest because of differences in stellar age, metallicity, element abundances, and the IMF of central galaxies (Conroy et al. 2018). To inform our interpretation of these differences, we turned to stellar population fitting codes `Prospector` and `alf`.

3.3.4 Stellar mass surface density profiles with Prospector

We used the stellar population fitting code `Prospector`[6] (Leja et al. 2017; Johnson et al. 2020) on the co-added spectra to estimate stellar masses (Section 3.2.3) and stellar mass surface density (Σ_*) profiles for all galaxies.

`Prospector` samples the posterior distribution for a variety of stellar population parameters and star formation history (SFH) prescriptions defined by the user. In this code, stellar population synthesis is handled by the code FSPS[7](Conroy et al. 2009; Conroy & Gunn 2010). Our runs used the MILES stellar library (Sánchez-Blázquez et al. 2006), MIST isochrones (Dotter 2016; Choi et al. 2016), and Kroupa IMF (Kroupa 2001) as inputs. We adopted a non-parametric SFH with a continuity prior, which emphasizes smooth SFHs

[6]https://github.com/bd-j/prospector/blob/master/doc/index.rst
[7]https://github.com/cconroy20/fsps

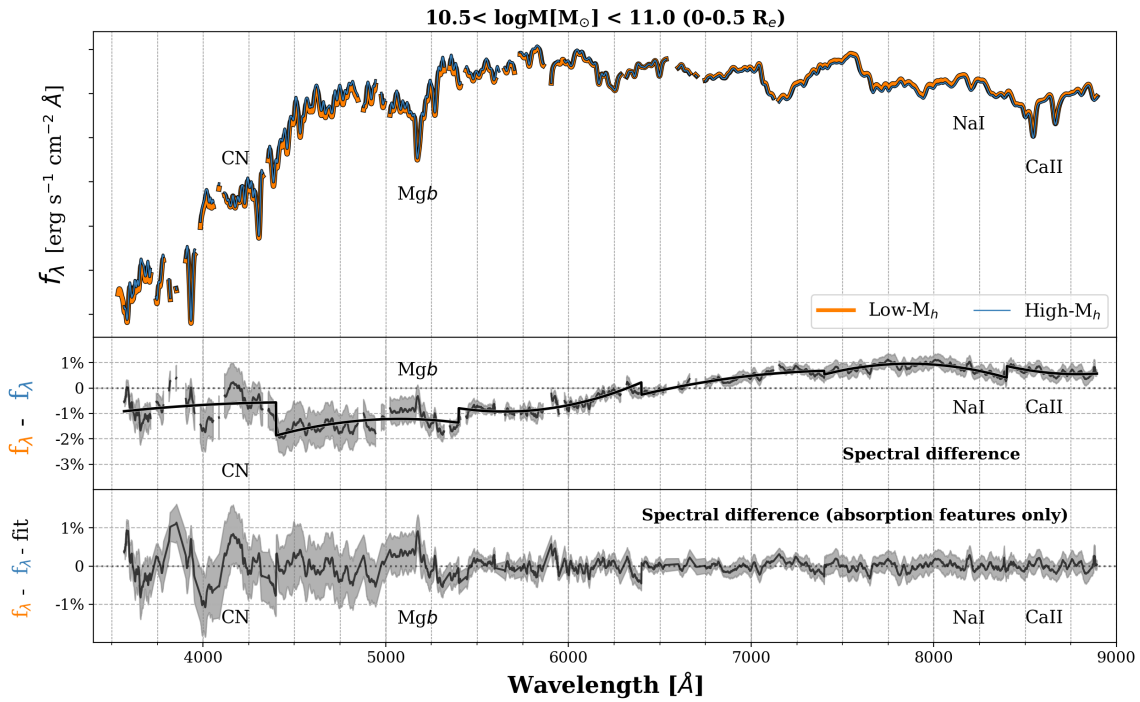

Figure 3.3: **Top:** Stacked spectra of central galaxies at fixed M_* that reside in low-M_h halos (orange) and high-M_h halos (blue). The data represent stacks within the central $0.5R_e$ for $M_* = 10^{10.5} - 10^{11} M_\odot$ centrals. **Middle:** The high-M_h stack subtracted from the low-M_h stack with a fit plotted in black. Gray shades show the error on this difference. **Bottom:** Result of subtracting the fit from the spectral difference. This highlights variations in several absorption features, some of which help to break degeneracies between various stellar population parameters. The two subsets reveal significant differences in both spectral shape and absorption features. Requiring no model assumptions, this figure demonstrates that M_h has an impact on the stellar populations of passive central galaxies with same M_*.

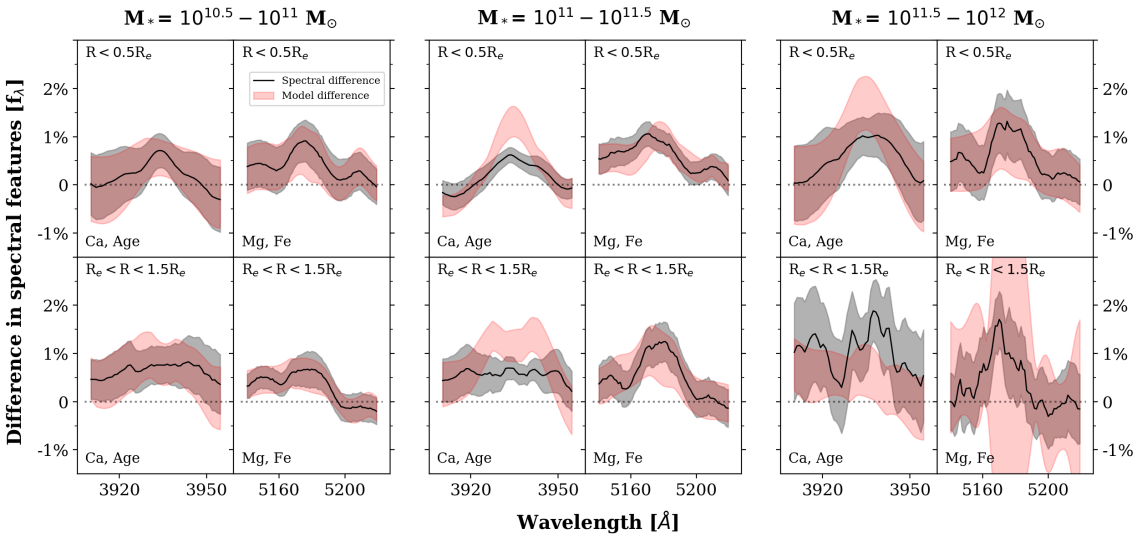

Figure 3.4: Differences in spectral features between low- and high-M_h centrals of the same M_*. Positive difference indicates stronger absorption in high-M_h galaxies, with the 1σ error plotted in gray. Different panels show different spectral features for which we detect significant differences that are systematic with M_* and radius. Stellar mass increases from left to right, galactocentric distance from top to bottom. Annotated are the stellar population parameters that dominate the strength of each feature. The red shading represents the 1σ posterior distribution of the best-fitting model spectra produced by `alf`. The `alf` posteriors reproduce the observed spectral differences well, although some model mismatch at the 1% level is apparent.

over time (Leja et al. 2019). As in Leja et al. (2019), we used the following time bins:

$$
\begin{aligned}
0 < t < 30 \text{ Myr} \\
30 \text{ Myr} < t < 100 \text{ Myr} \\
100 \text{ Myr} < t < 330 \text{ Myr} \\
330 \text{ Myr} < t < 1.1 \text{ Gyr} \\
1.1 \text{ Gyr} < t < 3.6 \text{ Gyr} \\
3.6 \text{ Gyr} < t < 11.7 \text{ Gyr} \\
11.7 \text{ Gyr} < t < 13.7 \text{ Gyr}
\end{aligned} \tag{3.6}
$$

Our parameter space also included the optical depth of dust in the V-band (Kriek & Conroy 2013), stellar mass, stellar velocity dispersion, and mass-weighted stellar ages and metallicities. To derive the posterior distributions, we used the Dynamic Nested Sampling package dynesty[8] (Speagle 2019).

3.3.5 Stellar ages and element abundances with alf

We used the program `alf` to characterize the stellar populations in more detail. This code fits the absorption line optical-near infrared spectrum of old ($\gtrsim$1 Gyr) stellar systems (Conroy & van Dokkum 2012; Conroy et al. 2018). Unlike `Prospector`, `alf` allows us to fit for the abundances of multiple elements and the IMF. This comes at the cost of computation times that are longer by a factor of 100. `alf` is based on the MIST isochrones (Dotter 2016; Choi et al. 2016) and the empirical stellar libraries by Sánchez-Blázquez et al.

[8] https://github.com/joshspeagle/dynesty/blob/master/docs/source/index.rst

(2006) and Villaume et al. (2017). Full spectral variations induced by deviations from the solar abundance pattern are quantified in the theoretical response functions (Conroy et al. 2018; Kurucz 2018). These allow `alf` to sample a multivariate posterior that includes the abundances of 19 elements (including C, N, O, Mg, and Fe).

We ran `alf` in "full" mode, which fits for a two-component SFH, stellar velocity dispersion, IMF, and the abundances of 19 elements. We adopted a triple power law IMF with two free parameters. Power laws were fit in the ranges $0.08 - 0.5\mathrm{M}_{\odot}$ and $0.5 - 1\mathrm{M}_{\odot}$. The IMF slope was set to -2.35 in the range 1-100 $\mathrm{M}_{\odot}$ (Salpeter 1955). Posterior sampling was performed with emcee (Foreman-Mackey et al. 2013). We found our runs to fully converge under the default configuration, which is 1024 walkers, 10^4 burn-in steps, and 100-step chains. For this setup, `alf` took $\sim$100 CPU hours per spectrum to run.

With `alf`, we recover stellar velocity dispersions within 1% of the input value ($\sigma_* = 350$ km s^{-1}). We derived mass-weighted stellar ages by mass-weighting the posteriors of the two-component SFHs. The stellar ages measured by `Prospector` and `alf` show agreements within 2 Gyr. The most significant age differences between high- and low-M_h centrals are found by both codes. More subtle differences are only detected by `alf` (more details in Section 3.4).

Following the approach of Lick indices, we use [Mg/Fe] as a proxy for [α/Fe] throughout(Johansson et al. 2012a, see Kirby et al. 2008 for other elements that can be used as tracers for [α/Fe]). Conversions from [X/H] to [X/Fe] assumed the correction factors in Schiavon (2007). The abundances measured by `alf` cannot be directly compared to the stellar metallicity reported by `Prospector`, since the latter only fits a scaled solar

abundance pattern.

For estimating uncertainties on the fitted parameters, we adopted a three-step method that was iterated over 5 times. First, we bootstrapped the galaxies selected in the sample assignment step from Section 3.3.1. Then, we computed the stacked spectra for the corresponding bootstrapped galaxies as in Section 3.3.2. Lastly, we fit each stacked spectrum with `alf`. This resulted in 5 posterior distributions for every subsample in each stellar and halo mass bin. The 5 distributions were then folded in, such that the final posteriors account for uncertainties in both methodology and modeling. Some of the model fits and posterior distributions are shown in Appendix 3.7.

3.4 Results

3.4.1 Empirical spectral differences with environment

Using the methods in Section 3.3.3, we quantified differences between the spectra of centrals in high- and low-M_h halos. Our findings are plotted in Figure 3.4. The M_* of the compared galaxies increases from left to right, with the top row displaying results for an inner bin of galactocentric radius and the bottom row for an outer bin. Shaded contours show 1σ errors, which fully account for uncertainties in sample assignment and stacking. Absorption features that are deeper in low-M_h galaxies are negative whereas features that are stronger in high-M_h galaxies are positive. We listed the stellar parameters that drive feature changes as quantified in the response functions by Conroy et al. (2018).

At all M_* and radii, high-M_h centrals show stronger Mgb 5172Å absorption (Faber & Jackson 1976b; Faber et al. 1985). Apart from being dominated by magnesium abun-

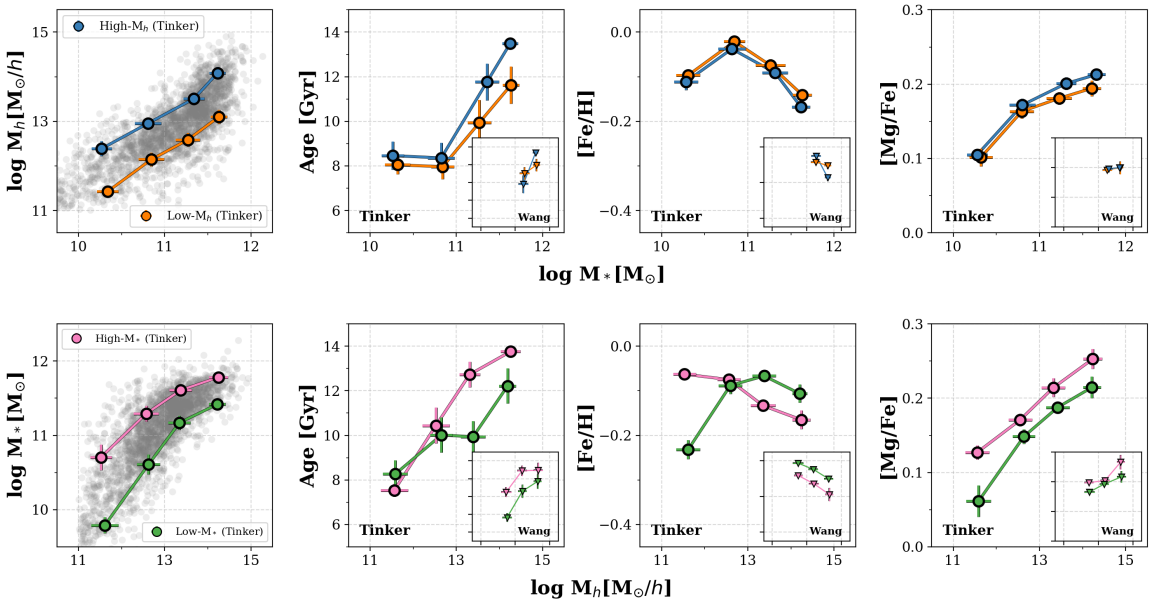

Figure 3.5: Stellar population parameters of passive central galaxies within $1.5R_e$ as a function of M_* (top) and M_h (bottom). Measurements that used the Tinker catalog for sample assignment are plotted in circles. Measurements that used the Yang+Wang catalog are shown in triangles. The stellar populations of passive centrals better correlate with M_* than with M_h. **Top:** High-M_h centrals are older (3.6σ), have lower [Fe/H] (3.6σ), and show higher [Mg/Fe] (3.4σ) than low-M_h centrals. **Bottom:** For $M_h > 10^{12}h^{-1}M_\odot$, the stellar populations of high-M_* centrals are older (4.4σ), have lower [Fe/H] (5σ), and have greater [Mg/Fe] (4.4σ) than those of low-M_* counterparts.

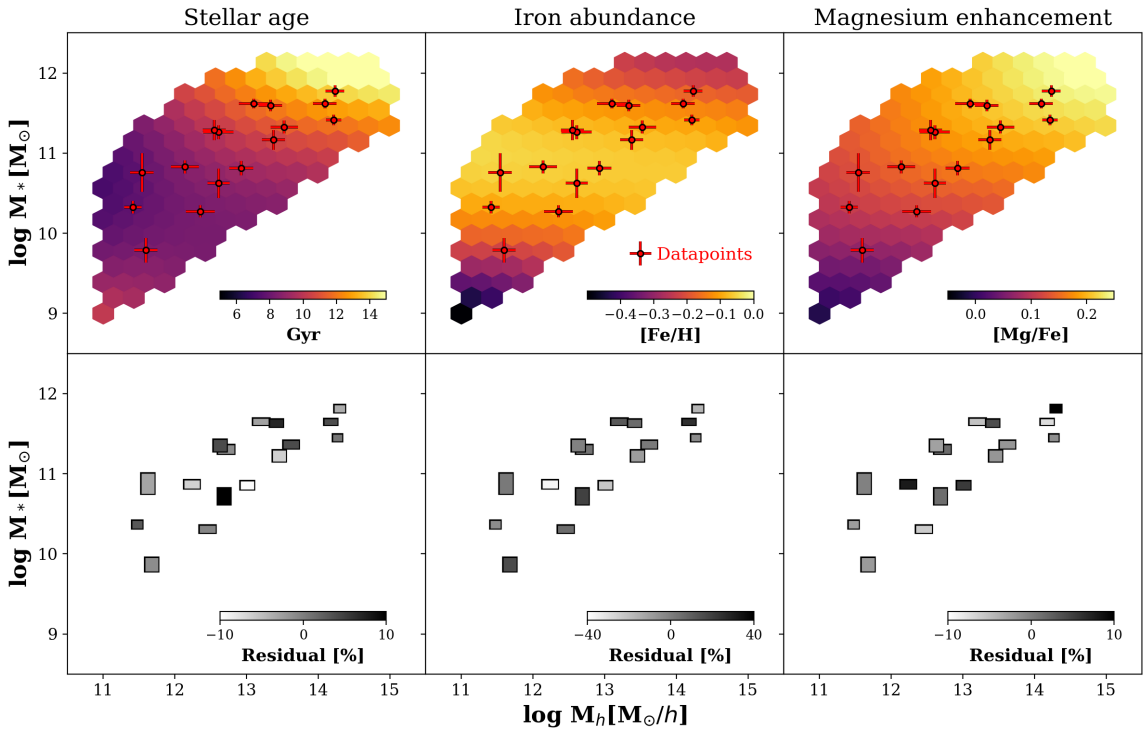

Figure 3.6: **Top:** The SHMR of passive centrals colored by stellar age, [Fe/H], and [Mg/Fe]. Values were derived by fitting two-dimension polynomials in M_*-M_h space to the measurements from Figure 3.5 that adopted $M_h^{\rm Tinker}$ (red datapoints). All parameters depend on both M_* and M_h. **Bottom:** Residuals relative to the median value of the parameter in the SHMR.

dance, this spectral feature is also sensitive to iron enrichment. Another significant set of spectral differences are found around 4000Å, which tend to be stronger in high-M_h centrals. These features are in a Ca-sensitive spectral region, as evidenced by the widely used CaHK, Ca4227, and Ca4455 spectral indices (e.g. Worthey et al. 1994; Tripicco & Bell 1995). Apart from being sensitive to the Calcium abundance, features at these wavelengths are also sensitive to stellar age and overall metallicity.

The detection of these differences demonstrates that halos have an impact on the stellar populations of passive central galaxies that is secondary to the correlation between M_h and M_*. We now turn to our results from stellar population fitting to attempt to interpret these results.

3.4.2 Integrated measurements

To derive the mean stellar population properties within the galaxy, we averaged the radial profiles derived with `alf` (Section 3.3.5). The results are shown with M_* and M_h as the controlling variable in the top and bottom panels of Figure 3.5, respectively. Measurements that used the Tinker catalog are plotted in circles, whereas those that used the Yang+Wang catalog are shown in the insets as triangles.

To first order, it is well known that stellar age and metallicity increase with the M_* or central velocity dispersion of galaxies (Faber & Jackson 1976a; Cid Fernandes et al. 2005; Gallazzi et al. 2005; Thomas et al. 2005, 2010; González Delgado et al. 2014; McDermid et al. 2015). While the top row of Figure 3.5 confirms this trend with age for the passive central galaxies in our study, we see that [Fe/H] decreases with M_*. In the literature, the word metallicity refers to a weighted average of the abundance of various elements (i.e., a

rescaling of the solar abundance pattern), whereas the [Fe/H] measurements that we derived with `alf` map the abundance of iron only. The decrease in [Fe/H] with M_* for $M_* > 10^{11} M_\odot$ is likely the result of how the formation timescales of galaxies become more rapid as M_* increases.

The plot in the top row, second column compares the stellar ages of centrals in low- and high-M_h at fixed M_*. With the Tinker catalog, we find low-M_h centrals to be younger than high-M_h counterparts by $\sim 1-2$ Gyr. Differences between the [Fe/H] of low- and high-M_h centrals are also present, with high-M_h centrals showing lower [Fe/H] by $\lesssim 0.05$ dex at all M_*. High-M_h centrals also show slightly greater [Mg/Fe], especially for $M_* > 10^{11} M_\odot$. Figure 3.5 shows that the deeper absorption seen in high M_h centrals (Figure 3.4) is primary a result of their older ages and higher magnesium-enhancement.

We can assign confidence levels to these results by computing the Bayes factor. As an example, we can consider the following two hypotheses: either high-M_h centrals are older or low-M_h centrals are older. The Bayes factor is just the ratio between the marginalized likelihoods of the models since we are interested in adopting flat, uninformative priors. In equation form, the Bayes factor is equal to

$$\mathcal{B} = \prod_{M_*} B_i = \prod_{M_*} \frac{\mathbb{P}(\mathrm{age}_{\text{high-}M_h} - \mathrm{age}_{\text{low-}M_h} > 0)}{\mathbb{P}(\mathrm{age}_{\text{high-}M_h} - \mathrm{age}_{\text{low-}M_h} < 0)}. \tag{3.7}$$

Figure 3.5 indicates that for the first M_* bin, the stellar ages of the two subsamples are quite similar, and therefore $\mathcal{B}_1 \sim 1$. On the other hand, high-M_h are significantly older in the highest M_* bin, and hence the associated Bayes factor is $\mathcal{B}_4 \sim 100$. If we assume that the two hypotheses cover all possible model options (i.e. that at least one of the subsamples is older), we can impose that the sum of the model probabilities is equal to one

(e.g. Oyarzún et al. 2017). With this method, we conclude that high M_h are older, have lower [Fe/H], and feature higher [Mg/Fe] than low-M_h centrals with 3.6σ, 3.6σ, and 3.4σ confidence levels, respectively.

We can now invert this analysis and use M_h as the controlling variable. The results are shown in the bottom row of Figure 3.5, and indicate clear secondary behavior in the stellar population of galaxies with different values of M_* at fixed M_h. We see that high-M_* centrals are nearly always older. For $M_h > 10^{12}h^{-1}M_\odot$, this difference can exceed 2 Gyr, has a significance of 4.4σ, and is clear in both halo catalogs. Differences in [Fe/H] show more complicated behavior that is dependent on M_h. For $M_h < 10^{12}h^{-1}M_\odot$, high-$M_*$ centrals show higher [Fe/H] by as much as 0.2 dex (8σ). For $M_h > 10^{12}h^{-1}M_\odot$, the difference reverses and [Fe/H] decreases with M_h (5σ). Significant differences are also observed in [Mg/Fe], with high-M_* centrals showing greater [Mg/Fe] at all M_h (5.6σ) and for $M_h > 10^{12}h^{-1}M_\odot$ (4.4σ) with both catalogs.

To help visualize the results across this multi-dimensional space, Figure 3.6 shows the SHMR colored by each of the stellar population properties we considered. This figure was made by fitting a two-dimensional, second-degree polynomial in M_*-M_h space to the results from Figure 3.5. Note how stellar age and [Mg/Fe] not only vary with M_*, but also with M_h. On the other hand, [Fe/H] depends almost exclusively on M_*.

3.4.3 The stellar population profiles of central galaxies

We now look at the radial dependence of our derived measurements. The stellar population profiles at fixed M_* are shown in Figure 3.7, with M_* increasing from left to right. High-M_h profiles are shown in blue and low-M_h profiles in orange. The comparison at fixed

M_h is shown in Figure 3.8, with high-M_* centrals in magenta and low-M_* centrals in green. The findings reported in this section apply to both catalogs, albeit only measurements using the Tinker catalog are shown to keep the figures simple.

In general, the stellar population profiles confirm the differences in normalization that we reported in Figure 3.5 and Section 3.4.2. We find stellar population differences to be rather constant with radius, indicating that no significant differences in profile shape are apparent between the subsamples. The stellar age and [Mg/Fe] profiles all tend to be flat, while the [Fe/H] profiles all fall with radius, as reported in previous work (e.g. Greene et al. 2015; van Dokkum et al. 2017; Alton et al. 2018; Parikh et al. 2018, 2019, 2021; Zheng et al. 2019; Lacerna et al. 2020).

The fact that parameter differences are mostly constant with radius indicates that the results in the integrated properties are not driven by outlier radial bins. This could have been more problematic in the outskirts, where the spectral S/N is a factor of two lower than at the centers (see Appendix 3.7). The profiles would also reveal if any trends in the integrated measurements are driven by standout physical behavior. For example, recent central star formation could also lower the mass-weighted stellar ages at the center, but we see no evidence for this either.

We therefore conclude that any variations in the shape of the stellar population profiles within $1.5R_e$ must be very subtle. Processes like radial migration could contribute to "wash-out" any subtle differences that might have been imparted by past events in the assembly history (Minchev et al. 2012; El-Badry et al. 2016). Moreover, the galactocentric distances probed in this paper are just inward of the radii at which the stellar metallicity

profiles of nearby galaxies start to show flattening due to minor mergers and stellar accretion from satellite galaxies (Oyarzún et al. 2019).

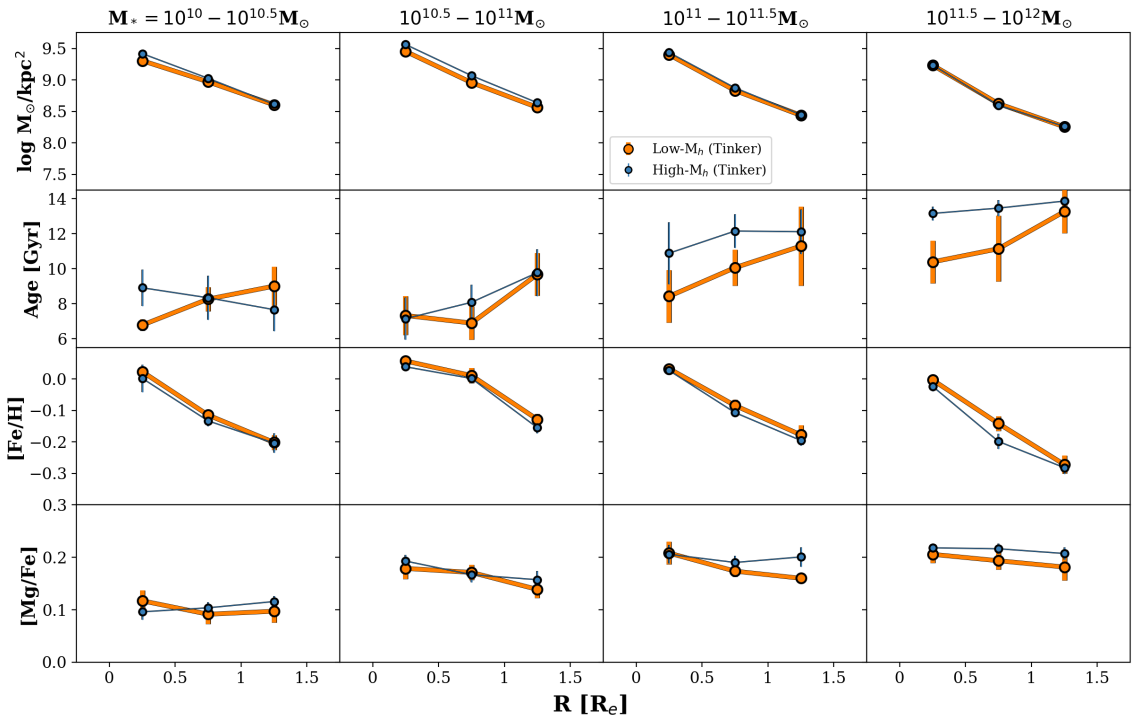

Figure 3.7: Stellar population profiles of low-M_h (orange) and high-M_h (blue) centrals at fixed M_* with the Tinker catalog. From top to bottom, shown are stellar mass surface density, stellar age, [Fe/H], and [Mg/Fe]. Stellar mass increases from left to right. Low-M_h centrals have younger stellar populations at all radii for $M_* > 10^{11} M_\odot$ and higher [Fe/H] at all radii and all M_* than high-M_h centrals.

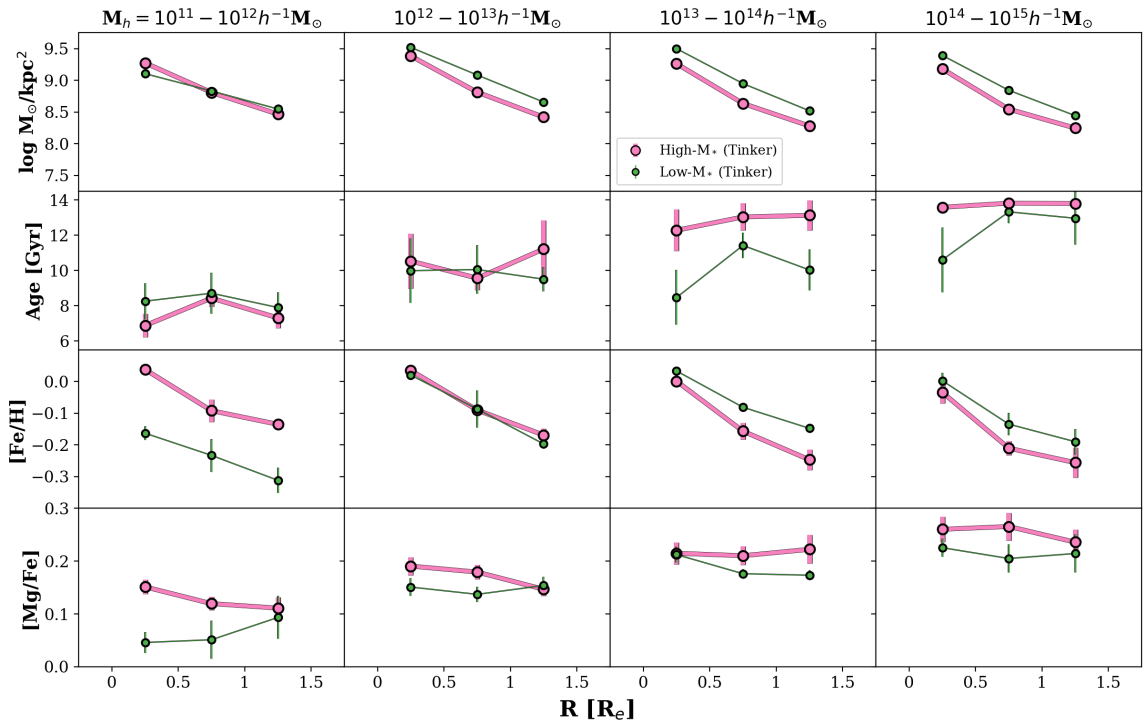

Figure 3.8: Stellar population profiles of high-M$_*$ (red) and low-M$_*$ (green) centrals at fixed M$_h$ with the Tinker catalog. From top to bottom, shown are stellar mass surface density, stellar age, [Fe/H], and [Mg/Fe]. Stellar mass increases from left to right. Despite their lower Σ_*, high-M$_*$ are more massive due to their much larger R_e. For M$_h > 10^{12}h^{-1}$M$_\odot$, high-M$_*$ centrals have stellar populations that are older, have lower [Fe/H], and show greater [Mg/Fe] than low-M$_*$ centrals at most radii.

3.5 Discussion

3.5.1 How halo mass modulates the stellar populations of passive centrals at fixed stellar mass

In the two phase scenario for galaxy evolution, the *in-situ* formation of central galaxies is followed by a phase of *ex-situ* growth through stellar accretion (Oser et al. 2010, 2012; Johansson et al. 2012b; Moster et al. 2013; Furlong et al. 2017). Recent observations of nearby massive galaxies provide support for this secondary phase. The stellar density profiles of massive galaxies at low redshift have faint, extended stellar envelopes that could have originated from late time stellar accretion (Huang et al. 2013b,a, 2018), as also identified locally in the Milky Way (e.g. Fernández-Trincado et al. 2019, 2020). Massive nearby galaxies also show flat stellar metallicity profiles beyond the R_e, as it would be expected if their outskirts assembled through minor mergers (Oyarzún et al. 2019).

In Oyarzún et al. (2019), we showed that this transition in the shape of the stellar metallicity profiles becomes prominent in galaxies with stellar mass greater than $M_* = 10^{11} M_\odot$. Our estimates of the *ex-situ* stellar mass fraction at R_e are consistent with zero for $M_* < 10^{11} M_\odot$ and unity for $M_* > 10^{11} M_\odot$. In this work, results from Figure 3.5 also indicate a phase transition at $M_* = 10^{11} M_\odot$. Below this M_*, differences in the host halo M_h seem to modulate the level of Iron enrichment at fixed M_*, while above $M_* = 10^{11} M_\odot$, differences in stellar age and [Mg/Fe] also become apparent.

A phase transition around $M_* = 10^{11} M_\odot$ also emerges in theoretical predictions. The baryon-to-star conversion efficiency is believed to peak around $M_* = 10^{10.5} M_\odot$ (e.g. Behroozi et al. 2013; Girelli et al. 2020), thus creating an inflection point in the SHMR (e.g.

Moster et al. 2010; Posti & Fall 2021). As M_* increases, the conversion efficiency decreases and mergers grow in importance (Rodriguez-Gomez et al. 2016; Rodríguez-Puebla et al. 2017). To first order, stellar mass that would have formed in the central galaxy at lower masses becomes increasingly locked up in satellites and the "intra-group" medium of host halos at larger masses. We can use these insights to inform our interpretation of Figures 3.5 and 3.7.

Focusing on lower mass galaxies with $M_* < 10^{11} M_\odot$, we see that centrals in low-M_h halos have higher [Fe/H] within $1.5R_e$ than centrals with the same M_* in larger halos. The same trend was recovered by Greene et al. (2015) in the MASSIVE survey (Greene et al. 2013) (though we should note that the opposite result was found by La Barbera et al. (2014) and Rosani et al. (2018); more in Section 3.5.2). This result can be interpreted two ways. First, it might imply that central galaxies in high-M_h halos more efficiently retained their gas throughout their star formation episodes. This could have led to rapid star formation, therefore enhancing their [Mg/Fe], which is precisely what we observe in 3.5. This Mg-enhancement in high-M_h centrals was also detected by Scholz-Díaz et al. (2022), who also characterized the stellar populations of central galaxies, but with single-fiber SDSS spectroscopy.

Alternatively, we know by definition that at fixed M_*, low-M_h centrals also have higher M_*-to-M_h ratios and lower numbers of satellites (see Figure 3.2). Perhaps our results are simply a sign of more extended central star formation histories at lower halo masses where lower virial temperatures and fewer satellites allow for longer periods of cold flow accretion (e.g. Dekel & Birnboim 2006; Zu & Mandelbaum 2016).

Before turning to the interpretation of our results toward $M_* > 10^{11} M_\odot$, we should emphasize that our sample binning and spectral S/N requirements in this work prevent us from studying the flattening of metallicity profiles in the low surface brightness outskirts of massive galaxies that were the subject of Oyarzún et al. (2019). The profiles in Figure 3.7 are mostly limited to the inner regions of galaxies, within $\sim 1.5 R_e$. That said, we see in this work that M_h has an impact on the formation of passive galaxies, even at the centers of $M_* > 10^{11} M_\odot$ centrals. Though subtle, these signatures of halo-modulated evolution are significantly detected, as evidenced in Figures 3.3 and 3.4.

For $M_* > 10^{11} M_\odot$, the stars in high-M_h halo centrals are older than their counterparts in low-M_h halos. At these large M_*, high-M_h centrals also have lower [Fe/H] and higher [Mg/Fe] at all radii. The fact that these differences are present at the centers and show little radial variation points to differences in *in-situ* formation, as opposed to minor merger accretion at larger radii. In line with our interpretation at lower M_*, a possible explanation is that low-M_h centrals continued forming stars over longer timescales. A later onset of quenching would yield younger stellar ages, higher [Fe/H], and lower [Mg/Fe] as measured today.

Given the more active merger history of high-M_* galaxies, it is worth exploring the possibility that a fraction of the stars at the centers of $M_* > 10^{11} M_\odot$ centrals was accreted. To lower the [Fe/H] abundance and increase the stellar age in high-M_h centrals, accreted stars would have to be metal poor and old. Oyarzún et al. (2019) argued that signatures of minor mergers are produced by the accretion of stellar envelopes that are more metal poor than the inner regions of the central, giving credibility to this explanation. However,

explaining why accreted stellar populations would be old is more challenging. The stellar ages of satellite galaxies rarely exceed 10 Gyr, even in halos as massive as $M_h > 10^{14} h^{-1} M_\odot$ (Pasquali et al. 2010). Yet, the stellar ages of high-M_h centrals can be as old as 12 Gyr for $M_* = 10^{11.5} M_\odot$.

Recently, Huang et al. 2020 exploited deep, wide-field imaging to measure individual early-type galaxy surface brightness profiles to $R \sim 150$ kpc for a sample large enough that precise M_h estimates could be derived through galaxy-galaxy weak lensing. They found that, as a function of their host halo M_h, central galaxies not only contain more M_* in their centers, but in their distant outskirts as well. If dry minor mergers are required to build those outskirts, does this mean that larger halos must be effective in suppressing star-formation in both their central galaxies *and* the within-the-satellite population that will later merger onto those centrals? Further exploration of this question requires a direct comparison between the stellar population profiles of central and satellite galaxies, a subject we will return to in future work.

3.5.2 How stellar mass drives evolution within dark matter halos of identical mass

So far, we have discussed the influence of the host dark matter halo mass (M_h) as a secondary, modulating variable in the formation and evolution of passive central galaxies at fixed M_*. This approach follows a long line of literature seeking to understand the role of "environment" after controlling for luminosity or stellar mass (e.g. Dressler 1980; Kauffmann et al. 2004; Peng et al. 2010b).

Our theoretical understanding of galaxy formation, however, begins by assuming

an underlying distribution of evolving dark matter halos and then seeks to build physical models on top (see Benson et al. 2000; Moster et al. 2013; Somerville & Davé 2015). Acknowledging our imperfect ability in this paper to measure dark matter halos observationally (see Section 3.5.2), we nonetheless turn to a theory-minded perspective, in which halo mass is the primary variable. By studying trends with M_* in bins of fixed M_h, we gain insight into the range of evolution that occurs within halos of fixed mass today.

Considering stellar age, [Fe/H], and [Mg/Fe] in nearly every mass bin, the bottom row of Figure 3.8 shows that the stellar populations of central galaxies at fixed M_h depend strongly on stellar mass. On the one hand, this result seems to be a familiar expression of how stellar populations depend on the luminosity of early-type galaxies (see Renzini 2006 for a review). But when we remember that our trends are seen at fixed M_h, they are perhaps more surprising. In two halos of identical mass today, central galaxies with different M_* have markedly different formation histories.

We discuss two physical interpretations of this result before concluding the discussion with an examination of potential observational biases.

Varying conditions of early formation

Our first interpretation follows in the spirit of "monolithic collapse," namely that the early conditions ($z \sim 4$) for gas accretion and mergers determine how the vast majority of stars in early type galaxies form. Rapid, intense formation leads to a greater stellar mass content (van Dokkum et al. 2009; Newman et al. 2010; Damjanov et al. 2011; Whitaker et al. 2012; Dekel & Burkert 2014; Zolotov et al. 2015). The number of stars formed in this early phase may be therefore largely independent of the progenitor halo properties, let

alone the halo's final mass at $z = 0$.

In this picture, certain halos would happen to host the conditions needed for gas-rich mergers which promote the early formation of massive central galaxies. These events would have to rapidly exhaust gas supplies to produce old and chemically enriched stellar populations today. Unfortunately, testing this scenario with stellar population profiles is challenging because the imprint of gas-rich mergers is hard to predict and sensitive to the initial conditions of the encounter (Kobayashi 2004).

We note, however, that at all M_h, high-M_h centrals are larger in size and show higher Σ_* [$M_\odot$/kpc] within $\sim$1 R_e compared to their low-M_* counterparts (see Figure 3.8). Their initial "collapse" may have driven up such large central gas densities that the resulting deep potential wells limited the impact of feedback, driving runaway growth in M_* (e.g. Matteucci 1994; Wellons et al. 2015). Such a period of collapse might leave kinematic and morphological signatures. Gas-rich major mergers might preserve the spin of the merger remnant, for example, giving rise to compact disks at $z \sim 2$ (e.g. van der Wel et al. 2011) and so-called fast rotators (e.g. Graham et al. 2018). On the other hand, a more extended formation period followed by dry mergers might produce slow rotator galaxies (Naab et al. 2014).

In a sense, this general picture aligns with Section 3.5.1 in that stellar mass, and not the dark matter halo, emerges as the dominant variable that controls how the bulk of stars in passive centrals form. This would seem antithetical to current theoretical models, however, and inconsistent with a variety of observational studies emphasizing the importance of M_h, or at least proxies thereof (e.g. $\Sigma_{1\mathrm{kpc}}$ and σ_*) in driving galaxy properties

(Figures 3.3, 3.4 of this paper and e.g. Franx et al. 2008; Wake et al. 2012; Chen et al. 2020; Estrada-Carpenter et al. 2020).

Galaxy Assembly Bias

If a galaxy's growth history is ultimately tied to its dark matter halo, then Figure 3.5 tells us that other halo parameters, beyond M_h, must play a role. These might include halo formation time and halo clustering (e.g. Gao et al. 2005; Wechsler et al. 2006), secondary properties which invoke the idea of "halo assembly bias." By definition, this term encapsulates all correlations between halo clustering and the assembly histories of halos at fixed M_h (Mao et al. 2017; Mansfield & Kravtsov 2020). For example, dark matter halos that assembled early tend to be more strongly clustered than counterparts that assembled at lower redshift (Gao et al. 2005; Contreras et al. 2019), especially for $M_h < 10^{13} h^{-1} M_\odot$ (Li et al. 2008).

The strong statistical relationship between halos and the galaxies they host (e.g. Leauthaud et al. 2017) has motivated predictions for how halo assembly bias might impact galaxy formation. Croton et al. (2007) used semi-analytic models to predict that halo formation time should correlate with galaxy luminosity at fixed M_h. In a halo mass bin of $M_h = 10^{14} - 10^{15.5} h^{-1} M_\odot$, they found that bright centrals formed in those halos that had mostly assembled by $z \sim 1$, whereas fainter centrals were associated with halos that assembled later ($z \sim 0.5$). Zehavi et al. (2018) expanded on this result, predicting a dependence of central M_* on halo formation time at fixed M_h.

An implied secondary dependence of stellar mass growth on halo age has also been studied with semi-empirical models. Bradshaw et al. 2020, for example, report factor of $\sim$3

differences in "central" M_* between the 20% youngest and oldest halos at fixed halo mass above $M_h > 10^{13} M_\odot$ as modeled in the UniverseMachine (UM; Behroozi et al. 2019). This difference in M_* and age (of approximately 1–2 Gyr) is similar to our results in the two bottom-left panels of Figure 3.5.

A galaxy assembly bias signal is also predicted in cosmological hydrodynamic simulations like EAGLE (Crain et al. 2015; Schaye et al. 2015; Matthee et al. 2017; Kulier et al. 2019) and Illustris (Vogelsberger et al. 2014a; Nelson et al. 2015; Xu & Zheng 2020), where it is driven by the fact that halos in dense regions not only collapse earlier but do so with higher halo concentrations (e.g. Wechsler et al. 2002; Zhao et al. 2009; Correa et al. 2015; Hearin et al. 2016). That yields deeper potential wells (Matthee et al. 2017) and more efficient central star formation (e.g. Booth & Schaye 2010). For example, Matthee et al. 2017 find an order-of-magnitude variation in central M_* at fixed halo mass below $M_h \lesssim 10^{12} M_\odot$. This variation correlates strongly with halo assembly time, which spans z =0.6–3 (see their Figure 7).

In IllustrisTNG, galaxy assembly bias is strongly imprinted in galaxy observables. At fixed M_h, central galaxies that are dispersion dominated, redder, larger, and have higher M_* are more strongly clustered, especially for $M_h < 10^{13} h^{-1} M_\odot$ (Montero-Dorta et al. 2020). In addition, centrals in IllustrisTNG with high M_*-to-M_h ratios exhausted their gas reservoirs earlier, thus quenching at higher redshifts (Montero-Dorta et al. 2021).

It is tempting to map these predictions to our observational results. At fixed M_h, high-M_* centrals have stellar populations that are older, have higher [Mg/Fe], and show lower [Fe/H], revealing that they formed earlier and more rapidly. In the galaxy assembly

bias scenario, this is a consequence of galaxy formation in older, highly concentrated halos. This explanation was also proposed by Scholz-Díaz et al. (2022) to explain why the same trends for stellar age and [Mg/Fe] are present in single-fiber spectra from SDSS.

Before we consider observational biases on this conclusion (Section 3.5.2), it is worth noting that there is disagreement among theoretical predictions for the detailed behavior of galaxy assembly bias. In the UM analysis, the secondary correlation with halo formation time is strongest for $M_h \gtrsim 10^{14} M_\odot$ (Bradshaw et al. 2020; see also Croton et al. 2007). But Matthee et al. (2017) find that halo formation time in EAGLE has no effect above $M_h \gtrsim 10^{12} M_\odot$. Instead, it strengthens at lower masses (see also Kulier et al. 2019). Meanwhile, Zehavi et al. (2018) and Xu & Zheng (2020) find a correlation between halo age and M_* that peaks around $M_h \sim 10^{12} h^{-1} M_\odot$ and mildly decreases in significance toward $M_h \gtrsim 10^{13.5} h^{-1} M_\odot$. Uncertainties in late-time growth explain some of the discrepancy. In hydrodynamical simulations, the stochasticity of late mergers can wash out formation-time bias at high-M_h (Matthee et al. 2017). The opposite happens in the UM because the bias here is driven by accreted stellar populations (Bradshaw et al. 2020). Halo age primarily influences the stellar mass that was accreted through mergers rather than the populations formed *in-situ*.

Finally, we note that the more rapid formation of high-M_* centrals, as inferred from the [Mg/Fe] and [Fe/H] measurements, is in agreement with the analysis by Montero-Dorta et al. (2021) in IllustrisTNG. However, it is in contrast with how high-M_* centrals assemble in EAGLE, where they grow by forming stars over long timescales (Kulier et al. 2019). As Contreras et al. (2021) concluded in their comparison of different galaxy assembly

bias models, the amplitude and behavior of the signal is strongly model-dependent.

Systematic errors and assembly bias signal

Many studies have searched for signatures of galaxy assembly bias and tentative detections have been reported, including correlations between halo concentration and the occupation fraction of centrals (Zentner et al. 2019; Lehmann et al. 2017), spatial clustering of galaxies (e.g. Berlind et al. 2006; Lacerna et al. 2014; Montero-Dorta et al. 2017), and galactic "conformity" (i.e., similarity in the physical properties of galaxies within a halo; Weinmann et al. 2006; Kauffmann et al. 2013; Calderon et al. 2018). Unfortunately, systematic errors in the distinction between centrals and satellites, halo mass estimates, and other problems have called into question many of these results (see Campbell et al. 2015; Lin et al. 2016; Tinker et al. 2018; Wechsler & Tinker 2018).

Much of the concern in our work centers on the group catalogs we use to infer the host dark matter halo properties. Indeed, we show explicitly that the choice of group catalog can affect our results. For example, the Yang+Wang and Tinker catalogs disagree as to whether low-M_h centrals have higher or lower [Fe/H] than their high-M_h counterparts (see Figure 3.5). These discrepancies are also present in other work. La Barbera et al. (2014) and Rosani et al. (2018) used the Yang et al. (2007) catalog to find that high-M_h centrals have younger and more Iron enriched populations than low-M_h centrals. The opposite was found by Greene et al. (2015) with the catalog by Crook et al. (2007).

While we favor the new group catalogs from Tinker (2020a,b), which are more sophisticated, self-consistent, and robust thanks to deeper imaging, systematic errors in M_h may significantly impact our conclusions. This is in large part because the M_h estimates

depend, at least in part, on the M_* of the central galaxy. In addition to counting satellite luminosity, the Tinker catalog also employs color and r-band light concentration when assigning M_h to an associated central galaxy. Our results indicate that high-M_* centrals have higher central Σ_*, the opposite of the expected bias with concentration. But they do have fewer satellites (apparent in Figure 3.2). This is expected because the central and satellite M_* values must roughly add to a constant at fixed M_h. It is possible that the history of satellite accretion drives the stellar population trends we see, independently of the halo assembly history.

Finally, the identified sample of "central" galaxies (which is roughly identical in the Tinker and Yang+Wang catalogs) is both incomplete and contaminated (by actual satellite galaxies) in ways that likely depend on M_* and inferred M_h. Disentangling these effects requires substantial mock observations that are beyond the scope of this paper.

Instead, in future work we can make progress by measuring observables associated with our subsamples that are independent of galaxy luminosity (i.e., independent of M_*). For example, the asssembly bias interpretation would be strengthened by a detection of different large-scale density signals on 10 Mpc scales for high- versus low-M_* galaxies at fixed M_h. Likewise, we can exploit new, more accurate proxies for M_h (e.g. Bradshaw et al., 2020), eventually aiming to derive M_h estimates from stacked weak lensing.

3.6 Summary

We constructed a sample of over 2200 passive central galaxies from the MaNGA survey to study how their assembly histories depend on M_* and M_h. We constrained the

stellar populations of our galaxies to high precision through spectral stacking and characterization with the codes `Prospector` and `alf`. We also control for systematics in M_h estimation by comparing the outputs from the group catalogs by Yang et al. (2007); Wang et al. (2016) and Tinker (2020a,b). Our findings can be summarized as follows:

1. At fixed M_*, there are significant differences in the spectra of passive centrals as a function of M_h. These differences are present at all M_* and we detect them at all radii ($R < 1.5R_e$). With no modeling involved, this shows that host halos have an impact on the formation of central galaxies.

2. To associate these spectral differences to stellar population variations, we turned to fitting with `Prospector` and `alf`. At fixed M_*, centrals in less massive halos show higher [Fe/H] and younger stellar ages. Our preferred explanation for this result is that the fewer satellites in low-M_h centrals allow for longer periods of cold flow accretion onto the central galaxy. As a result, low-M_h centrals undergo more extended star formation histories.

3. At fixed M_h, centrals with high-M_* have older stellar populations and formed in shorter timescales (low [Fe/H] and high [Mg/Fe]) than centrals with low-M_*. At first glance, this result might be expected given how the stellar populations of early-type galaxies depend on M_*. However, our results are the first to distinguish these evolutionary trends at fixed M_h. We propose two different scenarios to explain these results:

Varying conditions of early formation: at fixed M_h, centrals that undergo gas-rich mergers can fuel rapid, intense star-formation episodes followed by runaway growth in M_*. This process of "enhanced collapse" leads to the formation of old, α-enhanced stellar populations.

Galaxy assembly bias: according to theory, central galaxies with high M_*-to-M_h ratios assembled in early-forming, highly concentrated halos. Their gravitational potentials lead to early star-formation, efficient metal retention, and rapid exhaustion of their gas reservoirs.

4. Though we use two group catalogs in our analysis, we are still sensitive to sample contamination and systematic errors in M_h estimation. Future work can improve on these difficulties by measuring observables that are independent of galaxy luminosity or by exploiting more accurate proxies for M_h.

3.7 Appendix: Model fits and posterior distributions

Figures 3.9, 3.10, 3.11, and 3.12 show some of the fits and composite posterior distributions for high-M_* (red) and low-M_* (green) centrals. Halo mass increases with figure number. Top panels show the continuum-subtracted stacks and best fits. Residuals are plotted underneath. The errors shown in gray include the jitter and inflated error terms implemented by `alf`. Black vertical lines delimit the wavelength ranges used for continuum subtraction.

The bottom panels show the posterior distributions of mass-weighted ages, [Fe/H], and [Mg/Fe] derived with `alf` for the two corresponding spectra. The assumptions used to derive these quantities from raw `alf` outputs are described in Section 3.3.5. We fitted for a two-component SFH, stellar velocity dispersion, IMF, and the abundances of 19 elements. Posterior sampling was performed with emcee (Foreman-Mackey et al. 2013).

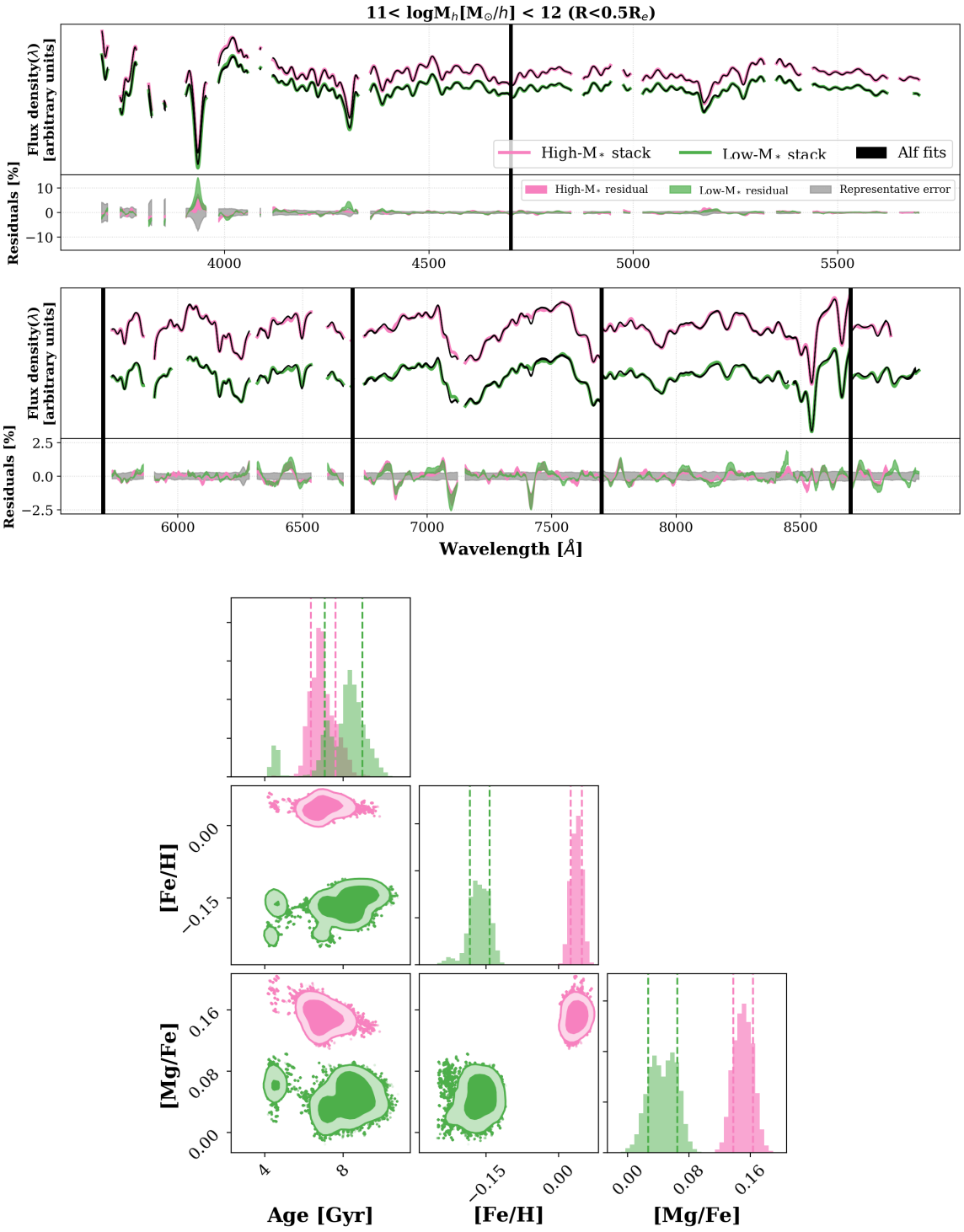

Figure 3.9: **Top:** Best fits and residuals for the 11 <logM$_h$[M$_\odot$/h]< 12 bin ($R < 0.5R_e$).

Bottom: Posterior distributions. Details in Appendix 3.7.

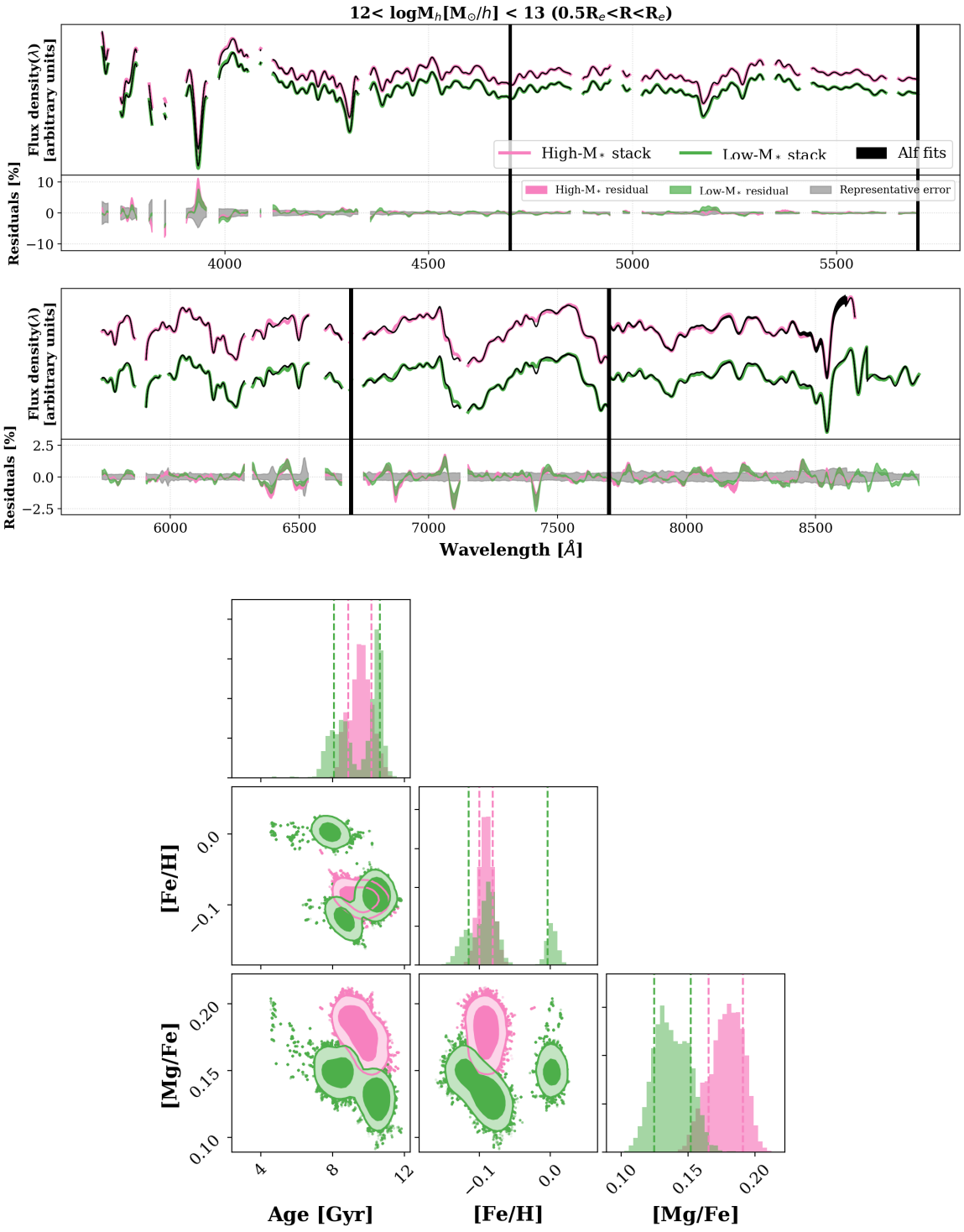

Figure 3.10: **Top:** Best fits and residuals for the 12 <logM$_h$[M$_\odot$/h]< 13 bin ($0.5R_e < R < R_e$). **Bottom:** Posterior distributions. Details in Appendix 3.7.

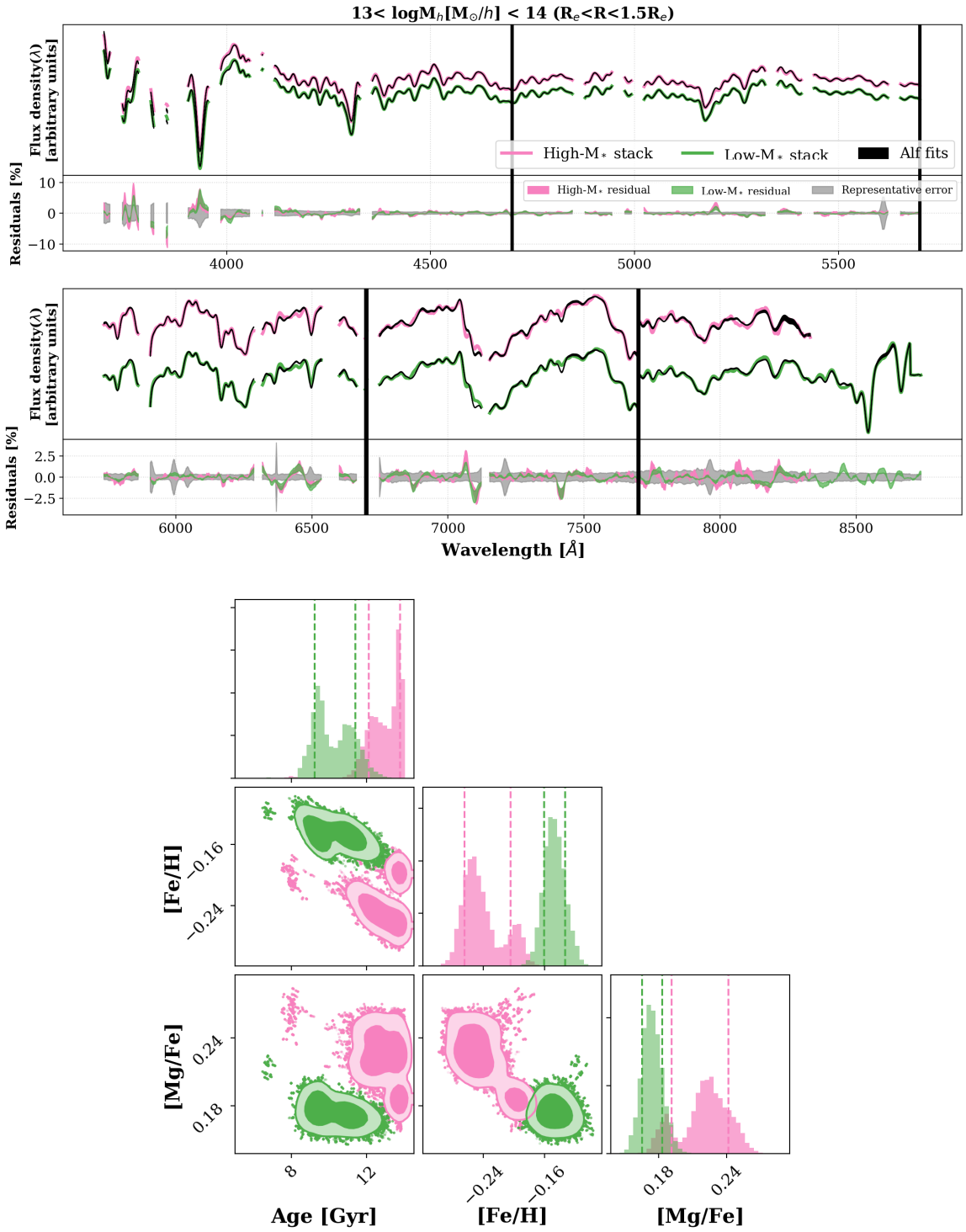

Figure 3.11: **Top:** Best fits and residuals for the 13 <logM$_h$[M$_\odot$/h]< 14 bin ($R_e < R < 1.5R_e$). **Bottom:** Posterior distributions. Details in Appendix 3.7.

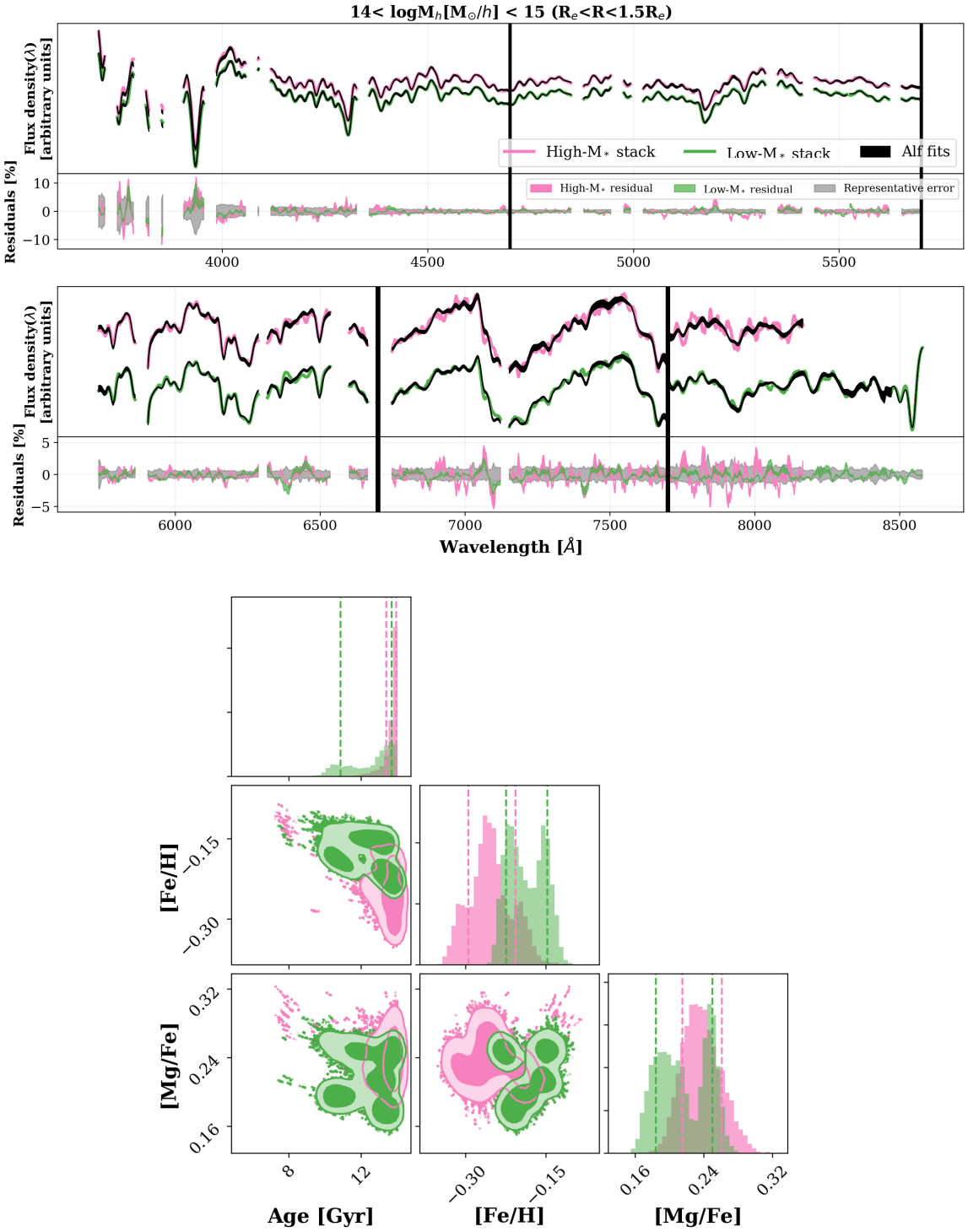

Figure 3.12: **Top:** Best fits and residuals for the 14 <logM_h[$M_\odot/h$]< 15 bin ($R_e < R < 1.5R_e$). **Bottom:** Posterior distributions. Details in Appendix 3.7.

Chapter 4

Evidence of galaxy assembly bias in the population of passive central galaxies in SDSS

4.1 Introduction

In the current cosmological picture, the formation of galaxies is closely connected to the growth of dark-matter halos (e.g. Wechsler & Tinker 2018). As halo mass (M_h) increases, so does the gravitational pull of the halo, facilitating the accretion of gas, fueling star-formation, and promoting the build-up of stellar mass (M_*). The resulting correlation between M_h and M_* is known as the stellar-to-halo mass relation of central galaxies (SHMR; e.g. Moster et al. 2013).

Halo properties other than M_h are also thought to impact the formation of central galaxies. Older and more highly concentrated halos feature deeper potential wells that promote a more rapid and earlier assembly of M_* at a given M_h (Matthee et al. 2017; Xu & Zheng 2020). The correlation between galaxy properties and secondary halo properties at fixed M_h is known as *galaxy assembly bias* (e.g. Mao et al. 2017).

The ubiquitous nature of galaxy assembly bias in theoretical work (Montero-Dorta et al. 2020; Xu & Zheng 2020) has motivated a search for observational proof of its existence. Tentative detections have been reported in the clustering of central (Lehmann et al. 2017; Zentner et al. 2019) and red and blue galaxies (Montero-Dorta et al. 2017). Signals have also been reported as part of galactic "conformity" (i.e., similarity in the physical properties of galaxies within a halo; Kauffmann et al. 2013; Calderon et al. 2018). However, the reliability of these results has been questioned, as biases of group catalogs can lead to spurious signals (Campbell et al. 2015; Lin et al. 2016; Wechsler & Tinker 2018).

In this work, we exploit the SDSS group catalog by Tinker (2020a,b) to mitigate these biases. The algorithm is calibrated on observations of color-dependent galaxy

clustering and estimates of the total satellite luminosity, which allows for a more accurate reproduction of the central galaxy quenched fraction. In addition, Tinker (2020b) used deep photometry from the DESI Legacy Imaging Survey (DLIS; Dey et al. 2019), allowing for precise accounting of galaxy M_* and group L_*.

We first used the Tinker (2020a,b) catalog in Oyarzún et al. (submitted) to characterize how the assembly histories of red central galaxies in the MaNGA survey (Bundy et al. 2015) depend on M_* and M_h. We found that centrals with high M_*-to-M_h ratios formed their stars early and rapidly, suggesting that they assembled in old dark-matter halos. In this paper, we test this hypothesis by studying how the number density of galaxies within $10h^{-1}$ Mpc, a proxy for halo formation time, depends on M_* and M_h in the SDSS MAIN Galaxy Survey (MGS; York et al. 2000; Gunn et al. 2006; Alam et al. 2015). As we will show, central galaxies with high M_*-to-M_h ratios assembled in old dark-matter halos, which is evidence of galaxy assembly bias.

This work is based on a sample of $\sim$ 150,000 red centrals from the SDSS MGS. We retrieved the spectroscopic M_* measured by Chen et al. (2012) and the M_h estimated by Tinker (2020b). We present our dataset in Section 4.2, results in Section 4.3, and discussion in Section 4.4. Our M_* adopted a Kroupa (2001) IMF and $h = 0.7$. All magnitudes are reported in the AB system (Oke & Gunn 1983).

4.2 Dataset

This paper uses the `dr72bright34` subsample of the MGS, which was defined in the construction of the NYU Value-Added Galaxy Catalog (NYU-VAC; Blanton et al.

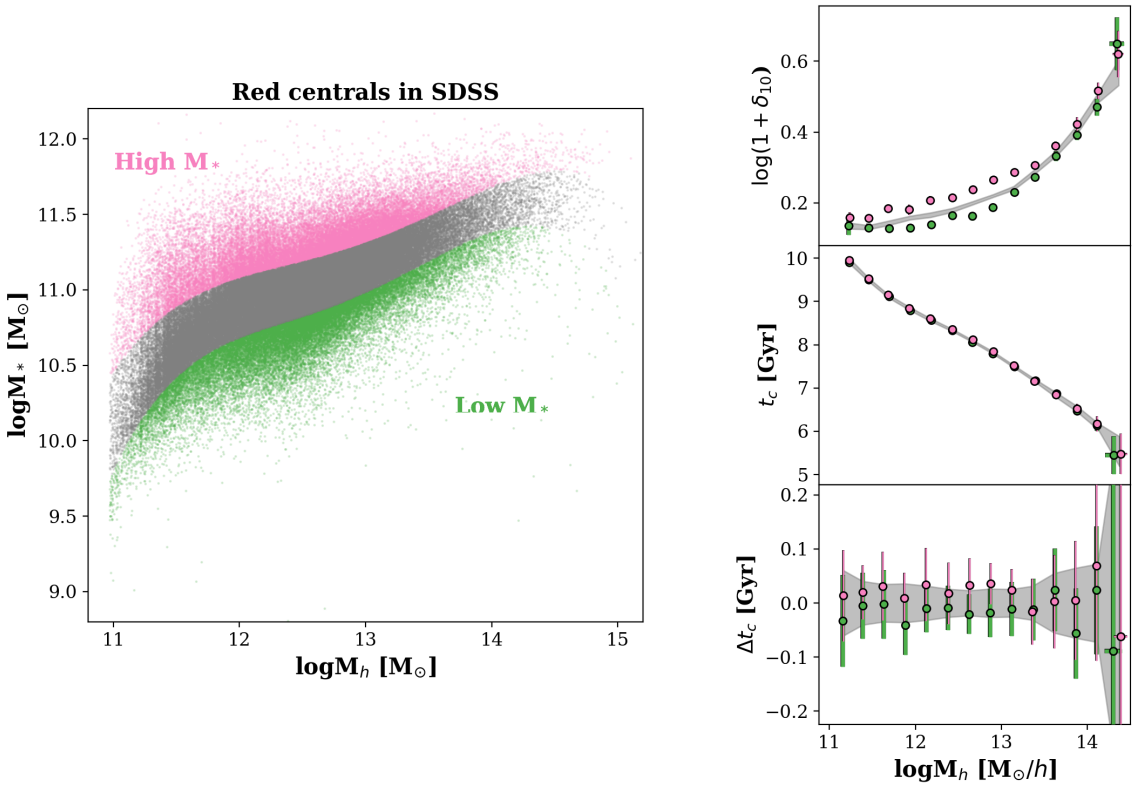

Figure 4.1: **Left:** Stellar to halo mass relation of red centrals in SDSS. The M_* were measured in SDSS spectra by Chen et al. (2012) and the M_h were estimated with deep photometry from the DLIS (Tinker 2020a,b). Centrals are divided into high M_* centrals (magenta) and low M_* centrals (green). **Right:** Normalized galaxy number density within 10 Mpc (top), halo formation time (middle), and difference in halo formation time (bottom) as a function of M_h. At fixed M_h, centrals with higher M_* reside in denser, older regions of the large scale structure, which is evidence of galaxy assembly bias.

2005a). Spectroscopy and data outputs were available as part of SDSS DR8 (Brinchmann et al. 2004). We restricted our galaxies to the redshifts $0.04 < z < 0.16$ to limit biases in the survey selection function, yielding 434,811 galaxies.

Group catalogs can bias the M_h distributions of red and blue galaxies differently (Lin et al. 2016). Therefore, we used a Gaussian-mixture model to quantify how the separation between red and blue galaxies in D_n4000 depends on L_{gal}. The outputs of the model were fit, yielding the threshold

$$D_{crit}(L_{gal}) = 1.42 + \frac{0.35}{2}\left[1 + \texttt{erf}\left(\frac{\log L_{gal} - 9.9}{0.8}\right)\right],$$

where `erf(x)` is the error function. All blue galaxies were removed, yielding 225,200 red galaxies. Further details can be found in Tinker (2020b).

The M_* were retrieved from the SDSS DR8 outputs. They were measured by Chen et al. (2012) as part of a PCA-based approach to constrain the star-formation histories (SFHs) and stellar populations of galaxies in SDSS DR7 and BOSS (Aihara et al. 2011). The small scatter at fixed halo mass shown by these stellar masses (~ 0.18 dex) make them ideal for this work (Tinker et al. 2017). To measure their M_*, Chen et al. (2012) described the optical wavelength range between 3700Å and 5500Å of every spectrum as the linear combination of seven model eigenspectra. The model space was constructed by generating a spectral library spanning a wide variety of SFHs. In this work, we retrieved the M_* that used the Maraston & Strömbäck (2011) stellar population synthesis models and Kroupa (2001) IMF for the construction of the library. The M_* for our final sample of central galaxies are shown in Figure 4.1.

Environment was quantified with the self-calibrating halo-based galaxy group

finder by Tinker (2020a). Here, the probability of a galaxy being a central depends on both galaxy type and luminosity, which allows for a more accurate reproduction of the central galaxy quenched fraction than with other algorithms. After central galaxies and their corresponding groups were determined, halo masses were assigned through the Bolshoi-Planck simulation (Klypin et al. 2016). At this point, color-dependent galaxy clustering and total satellite luminosity were used as observational constraints until the best fitting model was found.

Here, we work with the implementation of the Tinker (2020a) algorithm on SDSS (Tinker 2020b). To construct the catalog, Tinker 2020b used deep photometry from the DESI Legacy Imaging Survey (DLIS; Dey et al. 2019), allowing for more accurate accounting of galaxy M_* and group L_* than in other group catalogs (Yang et al. 2007). Our central galaxy sample was constructed by selecting all galaxies with satellite probabilities $P_{sat} < 0.1$. Of the 225,200 passive galaxies, 142,292 classified as passive centrals. Their M_h are shown in Figure 4.1. We adopted a standard error of $\log(M_h/M_\odot) = 0.3$ for all galaxies. The catalog is publicly available and can be found at https://galaxygroupfinder.net.

In this work, we use the normalized number density of galaxies (δ_{10}) as proxy for halo formation time. We computed δ_{10} for every central as

$$\delta_{10} = \frac{\rho_z}{\langle \rho_z \rangle} - 1, \tag{4.1}$$

where ρ_z is the number density of galaxies around a top-hat sphere of radius $10h^{-1}$ Mpc and $\langle \rho_z \rangle$ is the average ρ_z at the redshift of the central. These two quantities were estimated in simulations that randomized the spatial distribution of galaxies, and they account for completeness and edge effects. Errors in δ_{10} were obtained by propagating the Poisson error

in ρ_z. Further details on how δ_{10} is computed can be found in Alpaslan & Tinker (2020).

To assign halo formation times to our galaxies, we used the MultiDark Planck 2 Simulation (MDPL2; Prada et al. 2012). We first measured M_h, δ_{10}, t_c for every central in the simulation, where t_c is the time when the halo assembled half of its mass at $z = 0$. The characterization of $t_c = t_c(M_h, \delta_{10})$ in the MDPL2 was then used to assign values for the average and error on the t_c of every central in the MGS. This step was performed via Monte Carlo simulations that took full account of the scatter in M_h, δ_{10}, and t_c of both the MDPL2 and MGS. In the computation of δ_{10} in the MDPL2, we counted only subhalos with $V_{max} > 80$ kms^{-1}, as this yielded a distribution in (M_h, δ_{10}) that matched the MGS.

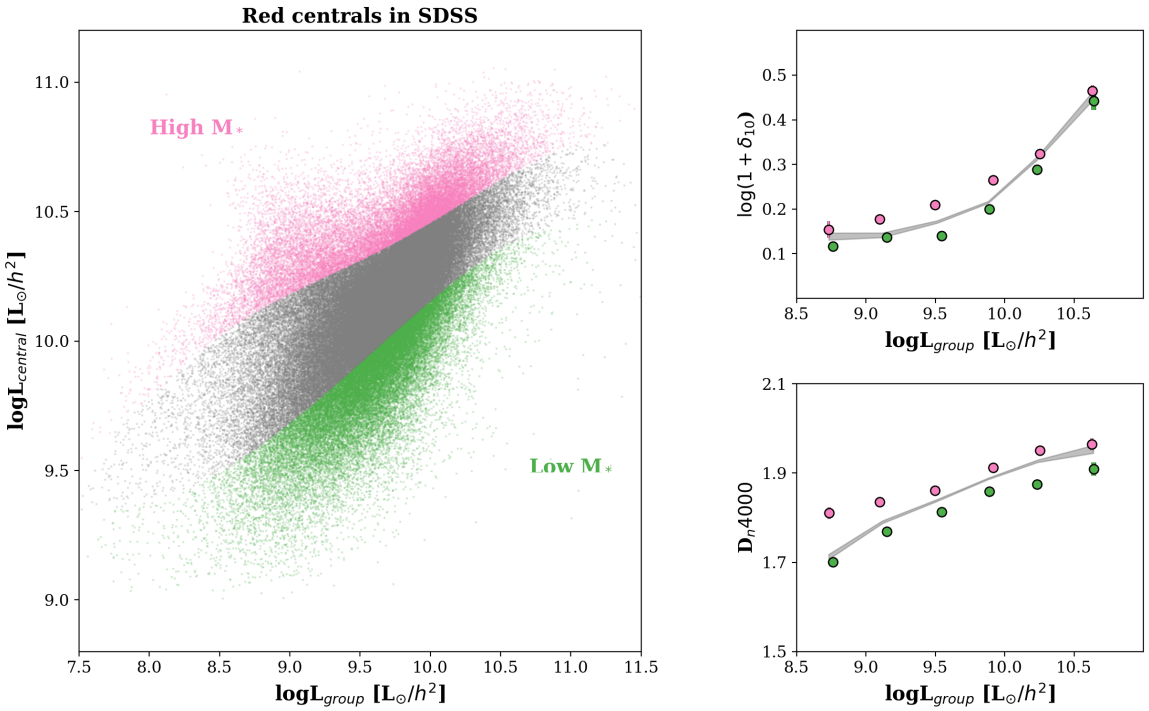

Figure 4.2: **Left:** Galaxy luminosity as a function of group luminosity for centrals in SDSS. Here, high M_* centrals (magenta) and low M_* centrals (green) are defined at fixed L_{group}. **Right:** Normalized galaxy number density within 10 Mpc (top) and D_n4000 (bottom) as a function of L_{group} for the two subsamples. At fixed L_{group}, centrals with higher M_* assembled in denser regions (i.e., older halos) and have higher D_n4000 (older/more metal-rich stellar populations). This figure highlights that the galaxy assembly bias signal from Figure 4.1 is also detected in observable quantities.

4.3 Results

Figure 4.1 shows the M_* and M_h of our sample. Two subsamples at fixed M_h were defined: high M_* centrals (magenta) and low M_* centrals (green). The right column of Figure 4.1 shows the δ_{10} and t_c of the two subsamples after binning in redshift space and then stacking (bins of width $\Delta z = 10^{-2}$). For $M_h = 10^{11} - 10^{13} h^{-1} M_\odot$, high M_* centrals have higher δ_{10} and older halo formation times than low M_* centrals.

Figure 4.2 shows that these trends are also present when using quantities that are more truthful to the data. At fixed group luminosity (L_{group}), high M_* centrals show higher δ_{10} (i.e., older halo ages) and higher D_n4000 (older/more metal-rich stellar populations) than low M_* centrals. Taken together, Figures 4.1 and 4.2 indicate that galaxy assembly bias is present in the population of passive central galaxies of SDSS.

4.4 Discussion

At fixed M_h, red central galaxies of higher M_* formed in older dark-matter halos. We also found higher M_* centrals to show systematically older stellar ages, higher [Fe/H], and greater [Mg/Fe] (Oyarzún et al. submitted). Taken together, these results indicate that early-forming halos lead to early star-formation, fast stellar mass build-up, and rapid quenching at fixed M_h (Booth & Schaye 2010; Matthee et al. 2017).

The greater metal-enrichment of high M_* centrals could also be associated with differences in halo concentration. At fixed M_h, older halos tend to show higher concentrations and therefore more strongly bind the stellar and gaseous contents of centrals (e.g. Wechsler et al. 2002; Hearin et al. 2016). In fact, Montero-Dorta et al. (2020, 2021) showed

that in the IllustrisTNG simulation (Vogelsberger et al. 2014a; Nelson et al. 2015), older, highly concentrated halos are responsible for the formation of high M_*, red, and old centrals.

This interrelation between galaxy and halo assembly is the strongest when the formation times of halos and galaxies go hand in hand. The galaxy assembly bias signal peaks in magnitude for $M_h \sim 10^{12.5} h^{-1} M_\odot$ (see Figure 4.1), which corresponds to halo and galaxy formation times of $\sim 8-9$ Gyr (Figure 4.1 and Oyarzún et al. submitted). As M_h increases, the deeper gravitational potentials of massive halos facilitate earlier and more rapid galaxy formation ($>$ 10 Gyr; Oyarzún et al. submitted). However, massive halos assemble most of their mass through mergers at later times (e.g. Figure 4.1), possibly indicating that the decoupling between the formation times of halos and galaxies is responsible for the decrease in magnitude of assembly bias toward $M_h \gtrsim 10^{13.5} h^{-1} M_\odot$. In addition, the stochasticity of merger growth can also "wash-out" any residual assembly bias trends in the stellar ages and stellar masses of massive centrals, an idea proposed in Matthee et al. (2017).

The range over which we find the assembly bias signal to peak is well reproduced by some theoretical work. In IllustrisTNG, the correlation between halo age and M_* also peaks around $M_h \sim 10^{12} h^{-1} M_\odot$ and mildly decreases in significance toward $M_h \gtrsim 10^{13.5} h^{-1} M_\odot$ (Zehavi et al. 2018; Xu & Zheng 2020). Though this agreement is interesting, we must exercise caution, as it may stem from similarities in how the IllustrisTNG and MDPL2 simulations populate the M_h, M_*, and t_c space. More telling is that galaxy assembly bias in IllustrisTNG is also present when using the number density of particles within $5h^{-1}$ Mpc instead of t_c (Zehavi et al. 2018), in strong agreement with the top right panel of our Figure 4.1.

Not all theoretical work predicts the signal to weaken for $M_h \gtrsim 10^{13.5} h^{-1} M_\odot$. In the UniverseMachine (UM; Behroozi et al. 2019), the magnitude of galaxy assembly bias remains strong even for $M_h > 10^{14} h^{-1} M_\odot$. Bradshaw et al. (2020) showed that the 20% youngest and oldest halos in the UM above $M_h > 10^{14} h^{-1} M_\odot$ show differences of a factor of $\sim 2-5$ in M_*. The EAGLE simulation (Crain et al. 2015; Schaye et al. 2015) is at the other end of the spectrum, predicting that halo formation time has little impact above $M_h \gtrsim 10^{11.5} h^{-1} M_\odot$ (Matthee et al. 2017). Some of the discrepancies between these simulations may originate in how mergers are handled by the different algorithms, especially given that mergers become increasingly important as M_h increases (Matthee et al. 2017; Bradshaw et al. 2020).

Our result also has important implications for the construction of galaxy formation models, as it can constrain how halo occupation distributions (HODs) are constructed (Tinker et al. 2008; Wechsler & Tinker 2018). For instance, Zentner et al. (2019) showed that accounting for assembly bias in the HOD can better reproduce the clustering of $M_r < -19$ galaxies in SDSS. The amplitude of the signal is particularly constraining, as incorrect galaxy assembly bias prescriptions can lead to systematic errors in the recovered clustering measurement (Zentner et al. 2014).

It is also important to address how biases in our approach could fabricate the galaxy assembly bias signal. For instance, passive central galaxies in the Yang et al. (2007) group catalog show older stellar ages and are more strongly clustered than star-forming counterparts of the same M_h (e.g. Wang et al. 2008). Yet, weak lensing analyses revealed differences between their underlying M_h distributions, indicating that the scatter of the

SHMR in the Yang et al. (2007) catalog correlates with the physical properties of galaxies in an unaccounted for manner (Lin et al. 2016).

Our approach accounts for these difficulties in multiple ways. First, our detection is not reliant on the differences between passive and star-forming centrals, since our sample is limited to the former. Second, the impact of the color-dependent spatial distribution of galaxies on halo mass estimation is accounted for, as the Tinker (2020a) algorithm is designed to fit for the clustering of passive and star-forming galaxies separately. It is also reassuring that the SDSS implementation of the algorithm can reproduce the weak-lensing derived SHMR (Mandelbaum et al. 2016), especially for passive centrals in our M_h regime (Tinker 2020b). Finally, the fact that we also recover the result when using total group luminosity is indication that the signal is not a byproduct of the complexity of the algorithm (Figure 4.2).

Another systematic error in group finding algorithms can be central and satellite galaxy mis-classification. Lin et al. (2016) showed that satellite contamination can affect the correlation functions and the dark matter profiles of central galaxy samples. Yet, as also pointed out by Lin et al. (2016), satellites that are mis-classified as centrals reflect the large-scale bias of their higher M_h hosts. As the normalized densities converge at high M_h (Figures 4.1 and 4.2), central and satellite galaxy mis-classification would weaken the assembly bias signal. Also, adopting a central selection criterion of $P_{sat} < 0.01$ instead of $P_{sat} < 0.1$ does not affect the results of this work.

Any biases arising from our M_* are unlikely. At fixed M_h, the measurement error of our stellar masses is $\Delta M_* < 0.18$ dex (Tinker et al. 2017), much smaller than the

~ 0.4 dex separating our two M_* subsamples (left panel of Figure 4.2). The normalized number densities are also robust, as the flux limit of the DLIS reaches 22.8 mag at 5σ (Dey et al. 2019), $5-6$ magnitudes deeper than the m_* of the galaxy luminosity function at $z = 0.1$ (Blanton et al. 2005a). The densities are also a measurement largely independent of halo mass, as they probe vastly different physical scales ($10h^{-1}$ Mpc and $\lesssim 1h^{-1}$ Mpc, respectively).

Still, quantifying the magnitude and significance of galaxy assembly bias with other probes for M_h is still a priority. Weak lensing can be used to search for systematic differences between the total mass surface density profiles of high and low M_* centrals (e.g. Lin et al. 2016). In addition, host M_h can also be estimated through the tight correlation between central M_*, M_h, and M_*^{max}, where M_*^{max} is the the stellar mass of the central out to 100 kpc (Huang et al. 2020). In future work, we will exploit these techniques to further constrain the role of halo assembly on galaxy formation.

This result opens up a new set of questions. Is there a signal for $M_h > 10^{13}h^{-1}M_\odot$ and is it driven by differences in halo angular momentum (Wechsler & Tinker 2018)? Does the signal propagate to the satellite galaxy population (Tinker 2020a; Alpaslan & Tinker 2020)? To answer some of these questions, the statistical power of upcoming surveys like The DESI Experiment (DESI Collaboration et al. 2016) will be key.

Chapter 5

The stellar population profiles of passive central and satellite galaxies

5.1 Introduction

Evolution of structure in the ΛCDM model is hierarchical (White & Rees 1978; Davis et al. 1985). Massive central galaxies are thought to grow in stellar mass (M_*) and size through the accretion of stellar envelopes from satellite galaxies (Oser et al. 2010, 2012; Johansson et al. 2012b). Several observations have found supporting evidence for this picture. Cluster galaxies show an excess in surface brightness that can extend out to 100 kpc and beyond (intra-cluster light; Zibetti et al. 2005). Similarly, the surface brightness profiles of massive elliptical galaxies ($M_* > 10^{11} M_\odot$) contain faint, extended components at large radii ($r > 10$ kpc; Huang et al. 2013b,a) presumably accreted from satellite galaxies (Huang et al. 2018). Furthermore, in Oyarzún et al. (2019) we showed that the stellar metallicity profiles of $M_* > 10^{11} M_\odot$ early-type galaxies (ETGs) flatten beyond the effective radius (R_e), which is another signature of stellar accretion (Cook et al. 2016; Taylor & Kobayashi 2017).

The hierarchical formation scenario can also successfully explain some of the differences between the central and satellite galaxy populations. At fixed M_*, satellite galaxies show higher stellar concentrations, older stellar populations, higher stellar metallicities, and a higher quenched fraction than central galaxies (van den Bosch et al. 2008a; Pasquali et al. 2010; Wetzel et al. 2012; La Barbera et al. 2014; Davies et al. 2019; Pasquali et al. 2019; Gallazzi et al. 2020; Trussler et al. 2021). These observations suggest that parent halos facilitate satellite quenching through mechanisms that can, for example, remove the subhalo ISM (i.e. ram-pressure stripping; Gunn & Gott 1972; Einasto et al. 1974; Nulsen 1982) or inhibit further star formation through the shutdown of cold gas accretion (e.g. starvation;

Kawata & Mulchaey 2008).

At the low M_* end ($M_* < 10^8 M_\odot$), ram-pressure stripping is thought to dominate satellite quenching (Weisz et al. 2015; Davies et al. 2016). Low M_* satellites interact with the intra-cluster medium (ICM) of the parent halo, stripping their gas reservoirs and truncating their star-formation (e.g. Balogh & Morris 2000; Mayer et al. 2001, 2006; van den Bosch et al. 2008b; Spindler & Wake 2017b). As a result, satellite galaxies show older stellar populations than centrals of the same M_* (Pasquali et al. 2010). At the same time, low M_* satellites can lose some of their M_* through tidal stripping (Kang & van den Bosch 2008). As this process leaves stellar metallicity roughly unaltered (Pasquali 2015), low M_* satellites deviate from the average stellar mass-metallicity relation followed by central galaxies (Faber & Jackson 1976a; Cid Fernandes et al. 2005; Gallazzi et al. 2005; Thomas et al. 2005, 2010; González Delgado et al. 2014; Pasquali 2015).

The impact of ram-pressure stripping is believed to decrease toward higher stellar masses ($M_* = 10^8 - 10^{11} M_\odot$), as deeper potentials can more effectively sustain drag from the ICM (Fillingham et al. 2015). At these masses, mechanisms that inhibit future star formation through environmental pre-processing more likely dominate. In starvation, satellite galaxies can lose their cold gas reservoirs through tidal interactions with the parent halo, suppressing future star-formation (Kawata & Mulchaey 2008). This process can also apply to hot subhalo gas in a process known as strangulation (e.g. Larson et al. 1980). These two mechanisms are thought to act in timescales of 2-6 Gyr, after which the satellite galaxy quenches within 1 Gyr ("delayed-then-rapid"; Wetzel et al. 2012, 2013).

All of these mechanisms point at a strong connection between the satellite infall

time (T_{inf}) and the satellite quenching time (T_q). To test this connection, Pasquali et al. (2019) and Smith et al. (2019) parameterized T_{inf} in projected phase space (distance and velocity of the satellite within the parent halo). Using this parameterization, Gallazzi et al. (2020) found ancient infallers ($T_{inf} > 5$ Gyr) to host older stellar populations and show higher stellar metallicities than recent infallers ($T_{inf} < 2$ Gyr). This result led Gallazzi et al. (2020) to conclude that ancient infallers likely quench through starvation and strangulation ($T_q > T_{inf}$). On the other hand, recent infallers probably quenched through internal processes, long before they entered the virial radius of the parent halo ($T_q < T_{inf}$).

So far, this picture for how central and satellite galaxies form and quench has been built almost uniquely on spatially integrated observations with SDSS (Pasquali et al. 2010; Wetzel et al. 2012; Pasquali et al. 2019; Gallazzi et al. 2020). To further develop this picture, we can take advantage of spatially resolved spectroscopy. For instance, major and minor mergers can change the shape of the stellar metallicity profiles of galaxies (Di Matteo et al. 2009; Cook et al. 2016; Oyarzún et al. 2019) and tidal stripping primarily removes stars beyond the tidal radius of satellite galaxies (Read et al. 2006). However, so far no conclusive evidence of any environmental dependence in the stellar population gradients of central and satellite galaxies has been found. For example, Santucci et al. (2020) reported no significant differences between the stellar age, metallicity, and [α/Fe] gradients of central and satellite galaxies in the SAMI survey (Allen et al. 2015). Goddard et al. (2017b) and Zheng et al. (2017) searched for differences between the stellar population gradients of centrals and satellites in the MaNGA survey (Bundy et al. 2015), and found no significant differences either.

Some of the difficulty in detecting these signatures originates in the sample sizes of spatially resolved surveys. Greene et al. (2015) were unable to compare the stellar population profiles of central and satellite galaxies at fixed M_* due to the size of the MASSIVE sample. Less than thousand galaxies had been observed by MaNGA at the time that Goddard et al. (2017b) and Zheng et al. (2017) performed their work on the stellar population gradients. This number is in strong contrast to the SDSS samples used by Pasquali et al. (2010); Gallazzi et al. (2020); Trussler et al. (2021), which exceeded 500,000 galaxies. However, now that the MaNGA survey is complete, in this paper we take advantage of the full sample that exceeds 10,000 galaxies. Taking into account signal-to-noise and the number of spectra per galaxy, the constraining power of MaNGA is almost a factor of two larger than that of the SDSS MAIN Galaxy Survey sample (York et al. 2000; Gunn et al. 2006; Alam et al. 2015; Oyarzún et al. submitted).

Another possible source of uncertainty comes from stellar population characterization. Most fitting codes do not fit for individual element abundances, adding uncertainties to reported ages and metallicities (Conroy 2013). This is particularly relevant in light of variations in the abundance pattern of passive galaxies with local environment (e.g. Greene et al. 2019 and Oyarzún et al. submitted). To account for these variations, in this work we use the stellar population fitting code `alf` (Conroy & van Dokkum 2012; Conroy et al. 2018). This program is designed to capture uncertainties in stellar evolution, allowing us to fit for the age, abundance of various elements, and initial mass function (IMF) of stellar systems older than 1 Gyr.

The use of stellar population gradients in spatially resolved surveys adds to the

difficulties. Linear fits to the stellar population profiles of early-type galaxies (ETGs) can "wash-out" underlying trends in the data (Oyarzún et al. 2019). For example, Greene et al. (2015) were only able to conclude that the ages of ETGs correlate with group richness by directly analyzing the stellar age profiles and their dependence on galaxy number density. In this paper, we overcome the limitations posed by the use of gradients by comparing the full extent of the stellar population profiles of central and satellite galaxies.

Cross-contamination of central and satellite galaxy samples also present a challenge. Group catalogs can sometimes struggle to reproduce the fractions of red and blue satellites, biasing the samples (Tinker 2020a). To mitigate this effect, we employ the SDSS group catalog by Tinker (2020b), which is calibrated on observations of color-dependent galaxy clustering and estimates of the total satellite luminosity to accurately reproduce the fraction of red and blue satellites for $M_* > 10^{11} M_\odot$. Furthermore, the Tinker (2020b) group catalog exploits deep photometry from the DESI Legacy Imaging Survey (Dey et al. 2019), allowing for the precise measurements of group luminosity required to estimate M_h.

This paper is structured as follows. In Section 5.2 we define our sample of passive central and satellite galaxies from SDSS-IV MaNGA. In Section 5.3, we describe our handling of the spectra and fitting with `alf`. We show our results in Section 5.4 and discuss the implications in Section 5.5. We summarize in Section 5.6. This work adopts a Kroupa IMF (Kroupa 2001) for estimating stellar masses. We assume $H_0 = 70$ km s^{-1}Mpc^{-1}, and all magnitudes are reported in the AB system (Oke & Gunn 1983).

5.2 Dataset

5.2.1 The MaNGA survey

The MaNGA survey (Bundy et al. 2015; Yan et al. 2016a) was part of SDSS-IV (York et al. 2000; Gunn et al. 2006; Blanton et al. 2017; Aguado et al. 2019) and provided spatially resolved spectroscopy for over ten thousand nearby ($z < 0.15$) galaxies (Drory et al. 2015; Law et al. 2015). The spectra have a median spectral resolution of σ=72 km s^{-1} (R$\sim$2000) and cover the wavelength range 3600-10300Å (Smee et al. 2013). The data cubes typically reach a 10σ continuum surface brightness of 23.5 mag arcsec^{-2}, and their astrometry is measured to be accurate to $0\farcs1$ (Law et al. 2016). Radial coverage reaches between $1.5R_e$ and $2.5R_e$ for most targets (Wake et al. 2017).

The data was reduced by the MaNGA Data Reduction Pipeline (DRP; Law et al. 2016; Yan et al. 2016b). De-projected distances, stellar kinematic maps, and emission line fluxes were computed by the MaNGA Data Analysis Pipeline (DAP; Belfiore et al. 2019; Westfall et al. 2019). Effective radii (R_e) for all MaNGA galaxies were retrieved from the NASA-Sloan Atlas[1](NSA). These R_e were determined using an elliptical Petrosian analysis of the r-band image from the NSA, implementing the detection and deblending technique described in Blanton et al. (2011). For data access and handling, we used the tool Marvin[2].

5.2.2 Sample

This work uses the final internal release of MaNGA data, known as MaNGA Product Launch 11 (MPL-11). The total number of galaxies in MPL-11 is 10,086. The approach

[1]http://nsatlas.org
[2]https://api.sdss.org/doc/manga/marvin

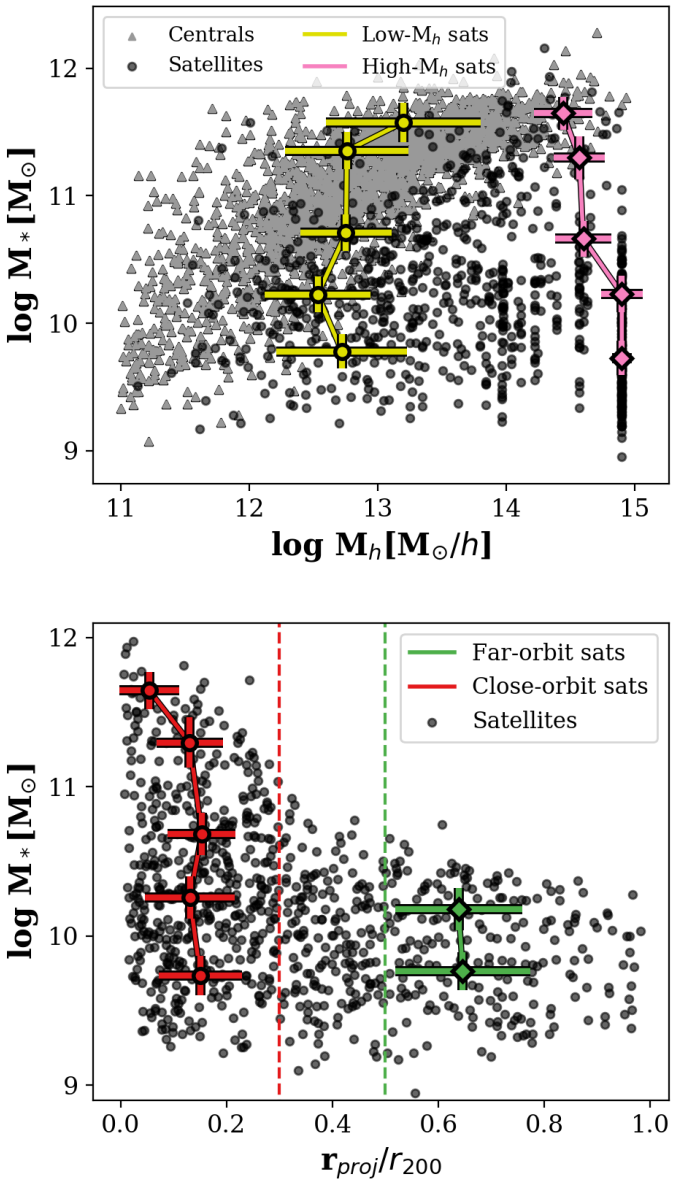

Figure 5.1: Distribution of passive MaNGA galaxies in stellar, halo mass, and normalized cluster-centric distance. Stellar masses were measured with `Prospector`. Central/satellite classification and halo mass estimates come from the Tinker (2020b) catalog. Shown are satellite galaxies only (black circles). We define two satellite subsamples according to host halo mass and normalized cluster-centric distance: close-orbit satellites (red) and far-orbit satellites (green). Shown are the mean and scatter of their distributions.

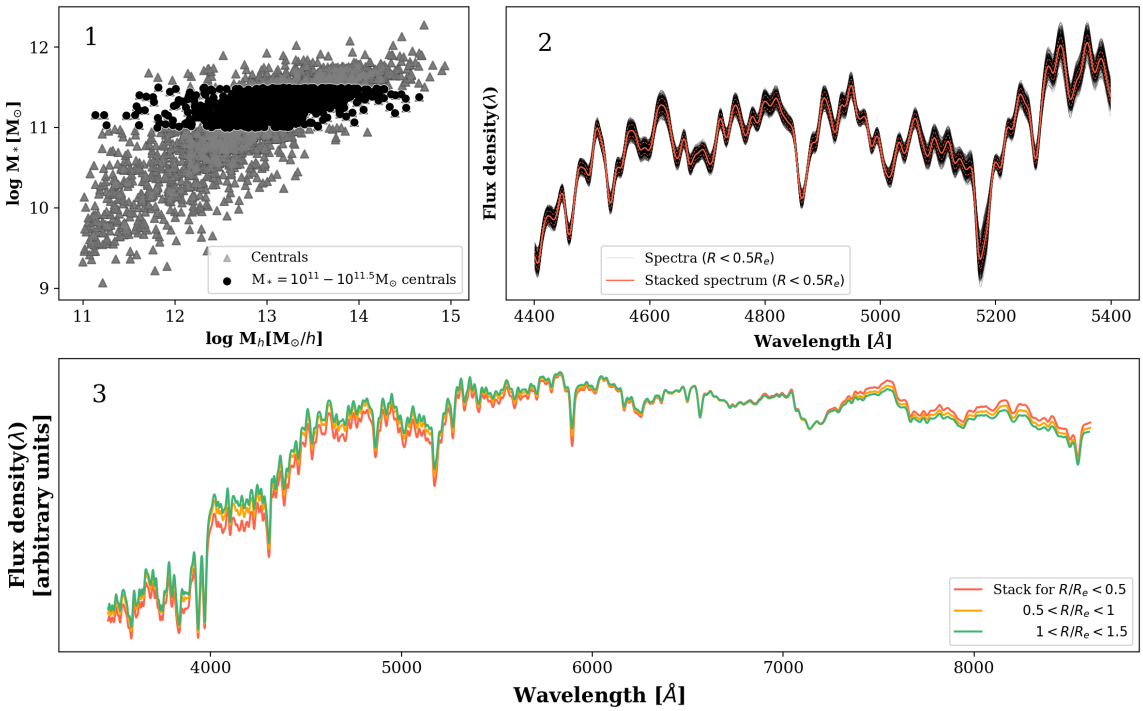

Figure 5.2: Treatment of MaNGA data. **Top left:** Stellar-to-halo mass relation of all passive central galaxies in MaNGA (gray triangles). Black circles show centrals in the $M_* = 10^{11} - 10^{11.5}$ bin. **Top right:** Spectra (within $0.5R_e$ of the galaxy center) of all centrals in the aforementioned bin (black). Resulting stack and errors are plotted in red. **Bottom:** Stacked spectra at all galactocentric distances for centrals in the $M_* = 10^{11} - 10^{11.5}$ bin.

Table 5.1: Number of passive central and satellite galaxies in MaNGA as a function of stellar mass

M_* [$M_\odot$]=	$10^{9.5} - 10^{10}$	$10^{10} - 10^{10.5}$	$10^{10.5} - 10^{11}$	$10^{11} - 10^{11.5}$	$10^{11.5} - 10^{12}$
Centrals	111	211	514	948	412
Low M_h satellites	85	101	43	10	7
High M_h satellites	117	107	24	17	12
Low M_h close-orbit sats	43	50	37	10	7
High M_h close-orbit sats	45	56	19	17	12
Low M_h far-orbit sats	33	26	3	0	0
High M_h far-orbit sats	37	28	1	0	0

Note that not all satellite galaxies are classified as either close-orbit or far-orbit (see Figure 5.1).

to stellar population characterization that we implement in this paper is designed for old stellar systems only. Therefore, we removed star-forming systems by setting the criterion $\log(\text{sSFR}) < -11.5$ $M_\odot yr^{-1}$, where sSFR stands for spatially integrated specific star-formation rates measured in MaNGA as part of the pipeline for the pipe3D Value Added Catalog for DR17[3] Since these sSFRs were corrected for dust attenuation using the Balmer decrement (Sánchez et al. 2016), this method to estimating the intrinsic sSFR of galaxies is among the most reliable at low-redshift (e.g. Moustakas et al. 2006). This selection resulted in a sample of 3957 passive galaxies, of which 2217 have more than a 90% probability of being a central and 902 have more than a 90% probability of being a satellite according to the Tinker (2020b) catalog (more in Section 5.2.4).

[3]https://www.sdss.org/dr17/manga/manga-data/manga-pipe3d-value-added-catalog/.

5.2.3 Stellar masses

To estimate the stellar mass (M_*) of every galaxy, we first co-added the spectra within the R_e. Then, the mass within the R_e was measured by running the stellar population fitting code `Prospector`[4](Leja et al. 2017) on the co-added spectrum.

`Prospector` samples the posterior distribution for a variety of stellar population parameters and star formation history (SFH) prescriptions. Stellar population synthesis is handled by the code FSPS[5](Conroy et al. 2009; Conroy & Gunn 2010). Our runs adopted the MILES stellar library (Sánchez-Blázquez et al. 2006), MIST isochrones (Dotter 2016; Choi et al. 2016), and a Kroupa 2001 IMF. For the SFH, we implemented a non-paramteric prescription with a continuity prior, emphasizing smooth SFHs over time (Leja et al. 2019).

The total stellar mass of the galaxy is then

$$M_*^{total} = 2M_*^{Re} \times 10^{-0.15}, \tag{5.1}$$

where M_*^{Re} is the spectroscopic stellar mass within the effective radius. We measure an offset of 0.15 dex between our $2M_*^{Re}$ and the stellar masses measured through k-correction fits to the Sersic fluxes in the NSA (Blanton & Roweis 2007). This is not unexpected, since half-mass radii are smaller than half-light radii (García-Benito et al. 2017). We correct for this offset by multiplying our stellar masses for $10^{-0.15}$ (see the equation). For the rest of the paper, we will simply refer to M_*^{total} as M_*.

[4]Prospector
https://github.com/bd-j/prospector/blob/master/doc/index.rst
[5]FSPS: Flexible Stellar Population Synthesis
https://github.com/cconroy20/fsps

5.2.4 Local environment

This paper uses the Tinker (2020b) group catalog for characterization of the local environment. This catalog is the implementation on SDSS of the self-calibrating halo-based galaxy group finder (Tinker 2020a). In the finder algorithm, the probability of a galaxy being a satellite is dependent on both galaxy color and luminosity. This allows Tinker (2020b) to accurately reproduce the fraction of massive quenched satellite galaxies and estimate M_h more accurately (Campbell et al. 2015). The Tinker (2020b) catalog also took advantage of deep photometry from the DESI Legacy Imaging Survey (DLIS; Dey et al. 2019), allowing for precise group and galaxy M_* measurements. These improvements are key to accurately constraining M_h (Bernardi et al. 2013; Wechsler & Tinker 2018).

Yet, the approach in Tinker (2020a) still has its limitations. Like most group catalogs, it is susceptible to central galaxy mis-identification. It also assumes that the total satellite luminosity is a function of halo mass only. The Tinker (2020b) catalog also fails reproduce the clustering of faint quiescent galaxies ($M_* < 10^{9.5} M_\odot$).

This work used the public version of the Tinker (2020b) group catalog[6]. Satellite probabilities (P_{sat}) were used to define central and satellite galaxy subsamples. To select centrals, we implemented the criterion $P_{sat} < 0.1$. To select satellites, we set $P_{sat} > 0.9$. These selections yielded two subsamples with 2217 central and 902 satellite galaxies. Their distribution in M_h and M_* space is shown in Figure 5.1.

[6]https://galaxygroupfinder.net

5.3 Methodology

5.3.1 Central and satellite subsamples

The assembly histories of satellite galaxies have been found to depend on both M_* and the M_h of the parent halo (Pasquali et al. 2019). Moreover, recent studies have shown that no differences between the quenching properties of centrals and satellites are apparent when both M_* and M_h are controlled for (Bluck et al. 2016; Wang et al. 2018b,a, 2020). To characterize these dependencies in the stellar population profiles, we defined three galaxy subsamples: centrals, low M_h satellites, and high M_h satellites. The two aforementioned satellite subsamples were defined to include only satellites below the 33rd and above the 66th percentiles in M_*-to-M_h ratio as a function of M_*. We note that the difference in M_h between the two satellite subsamples decreases with M_* (see Figure 5.1). After defining five M_* bins in the range $M_* = 10^{9.5} - 10^{12} M_\odot$ for every subsample (see Table 5.1), we computed high signal-to-noise stacked spectra.

The epoch at which the satellite first crosses the virial radius of the host halo (infall time; T_{inf}) is another property that shapes the stellar populations of satellite galaxies. For instance, Gallazzi et al. (2020) showed that the old ages of high M_h satellites are caused by ancient infallers ($T_{inf} > 5$ Gyr). On the other hand, the stellar populations of recent infallers ($T_{inf} < 2.5$ Gyr) were found to show little dependence on M_h.

Gallazzi et al. (2020) selected ancient and recent infallers by characterizing how T_{inf} is mapped onto the projected phase space composed of cluster-centric velocity and radius (Pasquali et al. 2019; Smith et al. 2019). Here, we implement a similar, albeit more simplistic, analysis based on cluster-centric radius only. As in Pasquali et al. (2019); Smith

et al. (2019), we define the projected, normalized cluster-centric radius as:

$$D_{proj} = r_{proj}/r_{200} \tag{5.2}$$
$$r_{200}[\text{kpc h}^{-1}] = 258.1 \times \frac{(M_h/10^{12})^{1/3} \times (\Omega_m/0.25)^{1/3}}{(1+z)} \ ,$$

where r_{proj} is the projected distance between the central and satellite, r_{200} is the virial radius (Yang et al. 2007; Pasquali et al. 2019), $\Omega_m = 0.3$, and $h = 0.7$.

Based on D_{proj}, we defined other two subsamples. Close-orbit satellites have $D_{proj} < 0.3$, and are meant to resemble the ancient infaller selection. According to Table 1 in Pasquali et al. (2019), close-orbit satellites have an average $\bar{\text{T}}_{inf} \sim 5$ Gyr and standard deviation $\sigma_{inf} \sim 2.5$ Gyr. Based on these numbers, we estimate a recent infaller contamination of 15%.

On the other hand, far-orbit satellites are defined by $D_{proj} > 0.5$ and are similar to recent infallers. Based on Table 1 from Pasquali et al. (2019), far-orbit satellites have $\bar{\text{T}}_{inf} \sim 3.5$ Gyr and $\sigma_{inf} \sim 2.5$. We estimate an ancient infaller contamination of around 20%.

Of our sample of 902 passive satellites, 473 are close-orbit and 185 are far-orbit. Detailed numbers, including their distributions in the low and high M_h classifications, are presented in Table 5.1 and Figure 5.1. Note that not all satellite galaxies are classified as either close-orbit or far-orbit.

5.3.2 Co-addition and stacking of spectra

Within every galaxy, we co-added the spectra into the three annuli R= $[0, 0.5]$, $[0.5, 1]$, and $[1, 1.5]$ effective radii. This step required shifting every spectrum back to the

rest-frame using the stellar systemic velocity (v_*) maps calculated by the DAP. Then, we stacked the spectra of central and satellite galaxies in each M_* and annular bin (see Table 5.1). Stacks were obtained by computing the median and errors were quantified through Monte Carlo simulations that accounted for the propagated errors. All spectra were convolved to $\sigma_* = 350\ kms^{-1}$ and median normalized before stacking. The stacking process is summarized in Figure 5.2.

5.3.3 Stellar population fitting with `alf`

The stacked spectra were fitted with the code `alf` to characterize their stellar populations. The program `alf` fits the optical absorption line spectra of old ($\gtrsim$1 Gyr) stellar systems (Conroy & van Dokkum 2012; Conroy et al. 2018) to estimate their stellar population parameters. It is based on the MIST isochrones (Dotter 2016; Choi et al. 2016) and the stellar libraries by Sánchez-Blázquez et al. (2006) and Villaume et al. (2017). Deviations from the solar abundance pattern are quantified in the theoretical response functions (Conroy et al. 2018; Kurucz 2018).

We fitted for a two-component SFH (i.e. two SSPs), stellar velocity dispersion, IMF, and the abundances of 19 elements. For the IMF, power laws were fit in the ranges $0.08-0.5M_\odot$ and $0.5-1M_\odot$, with the IMF slope set to -2.35 for the 1-100 $M_\odot$ range (Salpeter 1955). We sampled this multivariate posterior with `emcee` (Foreman-Mackey et al. 2013) using a setup of 1024 walkers, 10^4 burn-in steps, and 100-step chains.

Stellar ages reported throughout correspond to the mass-weighted age of the two component SFH. Uncertainties on the fitted parameters account for errors in sample assignment, stacking and fitting. This was achieved by bootstrapping the selection of galaxies

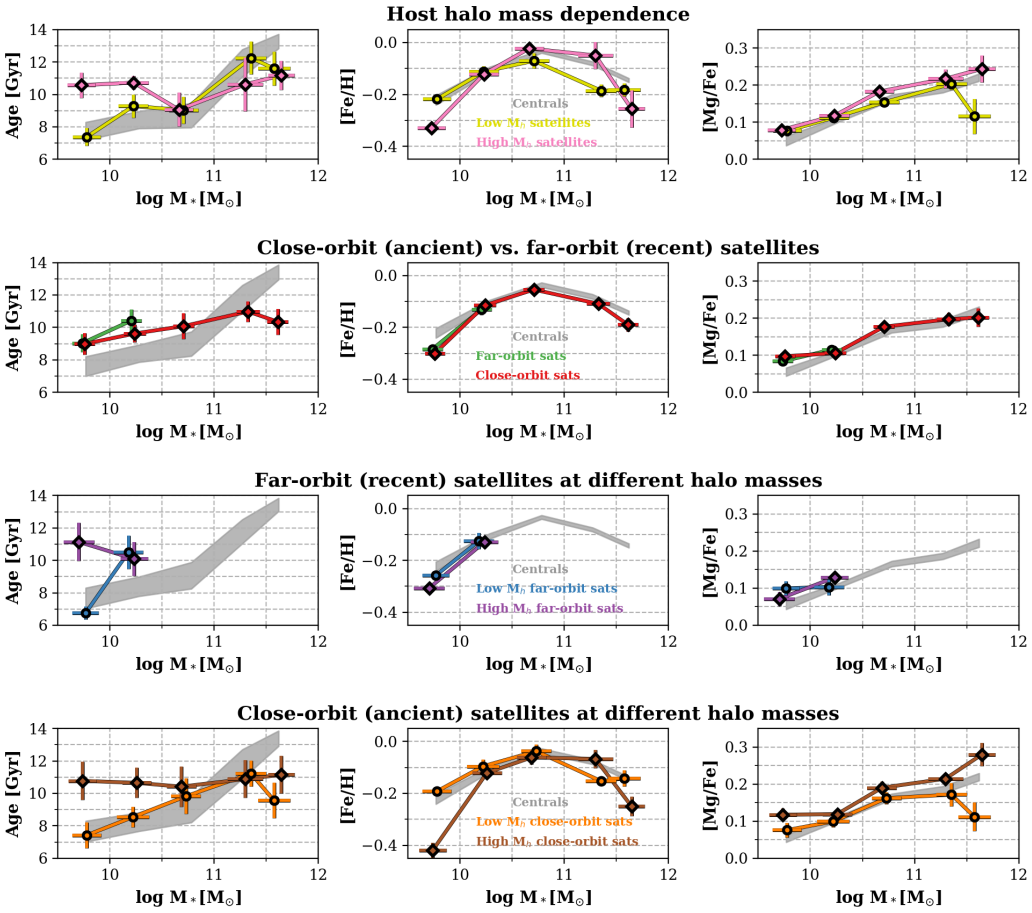

Figure 5.3: Stellar population parameters integrated within 1.5R$_e$ as a function of M$_*$. Stellar age is shown on the left, [Fe/H] in the middle, and [Mg/Fe] on the right. Different rows compare centrals against different subsamples of satellite galaxies. In the top two rows, satellites are divided as a function of host halo mass and custer-centric distance. Both selection methods are combined in the bottom two rows, with far-orbit satellites shown in the third row and close-orbit satellites at the bottom. At fixed M$_*$, satellites found in high M$_h$ halos are old and have high [Mg/Fe], even at fixed cluster-centric distance. Note that the selection in the first and final rows are not equivalent at high M$_*$, as some satellites do not qualify as either close-orbit or far-orbit (Figure 5.1).

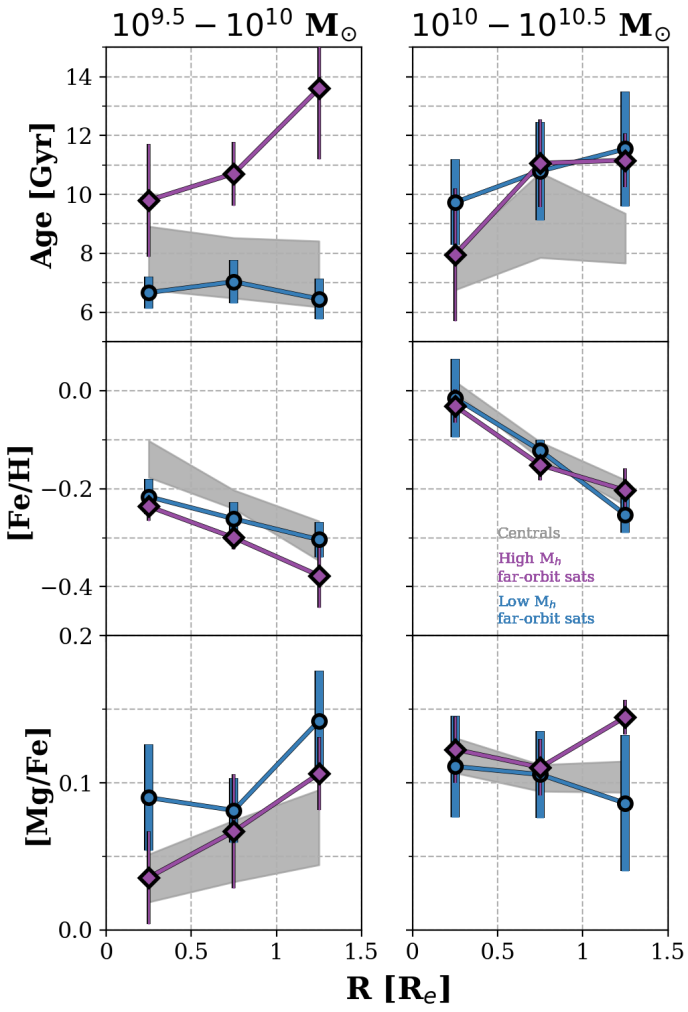

Figure 5.4: Stellar population profiles of centrals (gray), far-orbit satellites in low M_h host halos (blue circles), and far-orbit satellites in high M_h host halos (purple diamonds). From top to bottom, shown are the profiles in stellar age, [Fe/H], and [Mg/Fe]. Stellar mass increases left to right. At all radii, far-orbit satellites in high M_h halos show the oldest stellar populations.

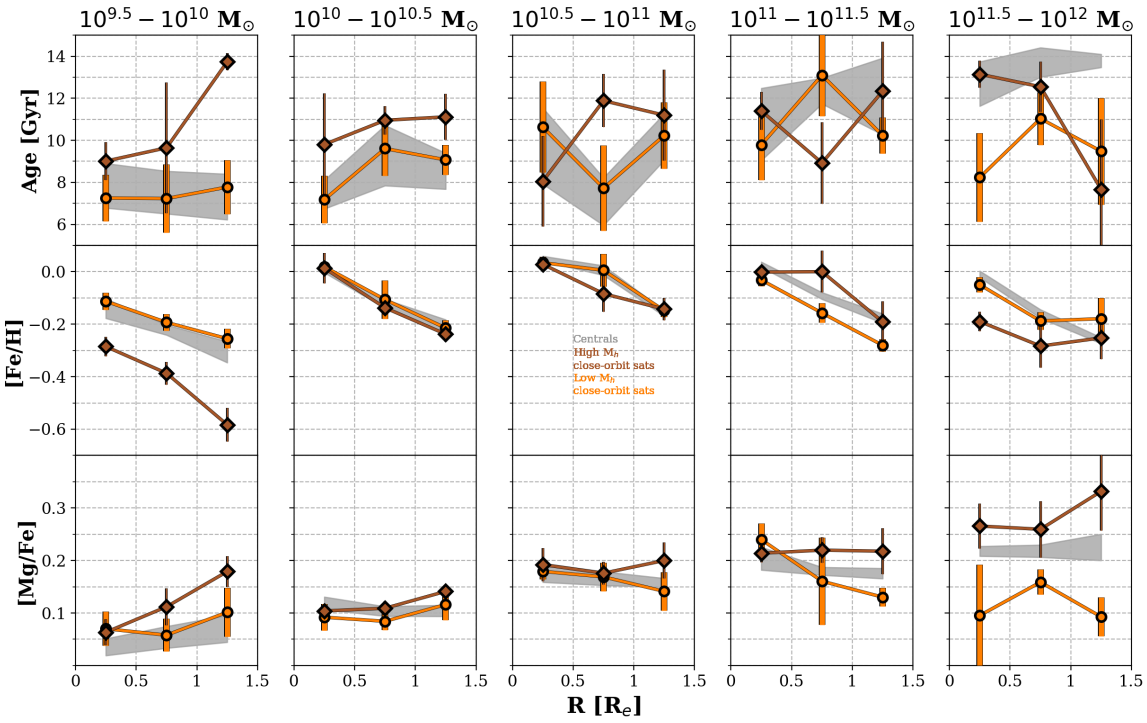

Figure 5.5: Comparison between the stellar population profiles of centrals (gray) and close-orbit satellites. The latter are divided into two bins: low M_h close-orbit satellites (orange circles) and high M_h close-orbit satellites (maroon diamonds). From top to bottom, shown are the profiles in stellar age, [Fe/H], and [Mg/Fe]. Stellar mass increases left to right. At most M_* and radii, close-orbit satellites in massive host halos show the oldest ages and the highest [Mg/Fe].

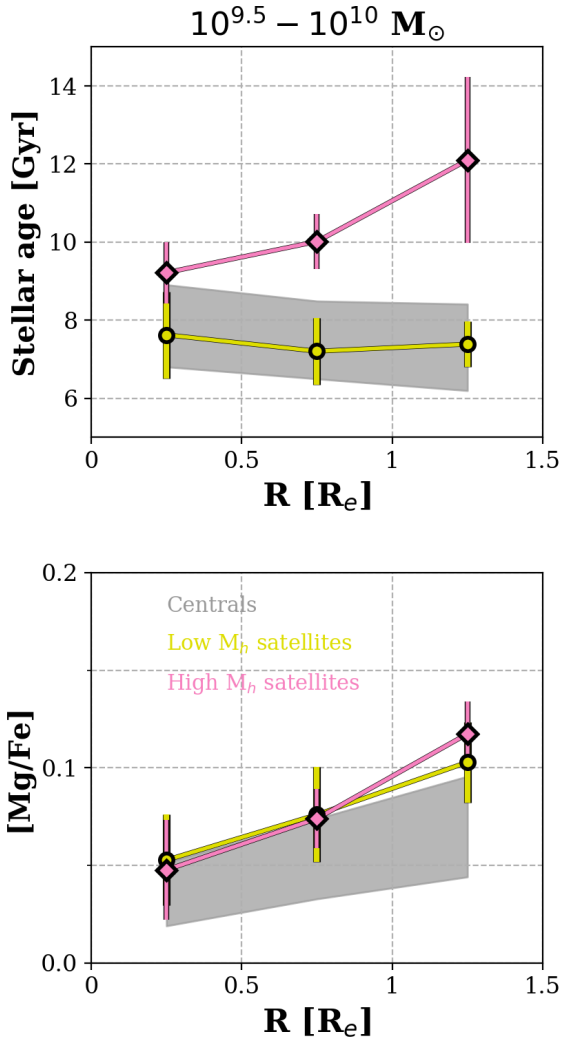

Figure 5.6: Stellar population profiles of passive galaxies with $M_* = 10^{9.5} - 10^{10} M_\odot$. Centrals (gray) are compared against satellites in host halos of low M_h (yellow) and high M_h (magenta). The top panel shows the stellar age profiles and the bottom panel the [Mg/Fe] profiles. Satellites in massive halos are older and have higher [Mg/Fe] than centrals beyond the R_e.

five times, and then by stacking and fitting in every iteration.

5.4 Results

Figure 5.3 shows the stellar population parameters integrated within $1.5R_e$ as a function of M_*. These were derived by radially collapsing the stellar parameter distributions measured with `alf` for every subsample and M_* bin. The datapoints and errobars shown in Figure 5.3 therefore correspond to the median and the standard deviation of the composite distributions. Instead of running `alf` on spectra stacked out to 1.5 R_e, collapsing the distributions better accounts for any radial scatter in the stellar population parameters and any scatter in the best fit models that would be lost in radial surface brightness variations within these galaxies.

Centrals and high and low M_h satellites are shown in the top row. Far- and close-orbit satellites are compared in the second row. To perform this comparison, we first divided close- and far-orbit satellites into two M_h bins and then radially collapsed the results using the same method outlined above. This approach allows us to decouple any impact of the underlying M_h distributions on the differences as a function of cluster-centric distance.

The bottom two rows show combinations of cluster-centric distance and host halo mass selections for satellites. As for centrals, we separated them into different M_h bins in Oyarzún et al. (submitted) and showed that stellar populations variations at fixed M_* are small. These variations are within the errorbars in our figures throughout this paper.

The left panels of Figure 5.3 show stellar age. The ages of central galaxies increase from 8 Gyr at $M_* = 10^{10}M_\odot$ to $>$ 10 Gyr for $M_* > 10^{11}M_\odot$. This is in agreement with

previous observations indicating that galaxies of increasing M_* are older (e.g. Gallazzi et al. 2005; McDermid et al. 2015; Lacerna et al. 2020). Satellite galaxies in high M_h halos tend to be older than centrals of the same M_* for $M_* < 10^{10.5} M_\odot$. This correlation between satellite age and host M_h is roughly independent on cluster-centric distance, hinting that host M_h is more important that accretion time in determining the ages of satellite galaxies.

Iron abundance is plotted in the middle panel. As we observed in Oyarzún et al. submitted, the magnitude of [Fe/H] increases with M_* before turning over around $M_* \sim 10^{11} M_\odot$. This might seem to contradict the stellar mass-metallicity relation, in which metallicity always increases with the M_* or central velocity dispersion of the galaxy (Faber & Jackson 1976a; Cid Fernandes et al. 2005; Gallazzi et al. 2005; Thomas et al. 2005, 2010; González Delgado et al. 2014; McDermid et al. 2015). This is because stellar metallicity is typically used to refer to a weighted average of the abundance of various elements (i.e., a rescaling of the solar abundance pattern), whereas the [Fe/H] that we measured with `alf` map the abundance of iron only. As we pointed out in Oyarzún et al. submitted, the decrease in [Fe/H] with M_* at the massive end is likely a consequence of how the star-formation timescales of galaxies shorten as M_* increases.

With that said, we generally find satellites to show lower [Fe/H] than centrals by $\sim 0.05 - 0.1$ dex, especially for satellites with $M_* < 10^{10.5} M_\odot$ residing in massive host halos. The right panel of Figure 5.3 shows [Mg/Fe], a proxy for [α/Fe] (e.g. Faber & Jackson 1976a; Faber et al. 1985; Thomas et al. 2005). We observe slightly higher [Mg/Fe] in satellites than in centrals, with the effect being more pronounced for high M_h satellites in close-orbits.

Details of how central and satellite galaxies form are also contained in the radial distribution of their stellar populations. Therefore, we also compared their stellar population profiles. Centrals and far-orbit satellites are compared in Figure 5.4, whereas the comparison between centrals and close-orbit satellites is shown in Figure 5.5. For both of these figures, stellar mass increases from left to right. From top to bottom, shown are stellar age, [Fe/H], and [Mg/Fe].

The stellar age profiles are rather flat for all subsamples, in agreement with work on the stellar population gradients of massive galaxies (Goddard et al. 2017a,b; Zheng et al. 2017). On the other hand, the [Fe/H] profiles fall with radius (e.g. Greene et al. 2015; Parikh et al. 2018, 2019; Lacerna et al. 2020). As measured in Parikh et al. (2019), the [Mg/Fe] profiles have a shape that is constant with radius.

There are notable differences in normalization between the profiles of central and satellite galaxies. Satellites in high M_h halos are older and have greater [Mg/Fe] than centrals at most radial bins from the centers out to $1.5R_e$. The consistency with radius in these differences means that variations between the integrated properties of centrals and satellites (Figure 5.3) are not driven by single radial bins.

Given the uncertainties resulting from the required sample binning, we see little statistically significant variation in the shape of the radial profiles between centrals and satellites. A key exception are the age and [Mg/Fe] profiles for $M_* < 10^{10}M_\odot$. At these M_*, the ages and [Mg/Fe] of centrals show a flat radial dependence, whereas the ages and [Mg/Fe] of satellites in massive halos increase noticeably with radius (Figures 5.4, 5.5, and 5.6). These results represent the first detection of an environmental signal in the radial

profiles of stellar population diagnostics.

5.5 Discussion

Several mechanisms have been proposed to explain how galaxies quench (De Lucia et al. 2012; Knobel et al. 2015; Davidzon et al. 2016; Jian et al. 2017; Pintos-Castro et al. 2019). Some mechanisms can be classified as environment-driven, meaning that they are triggered by the parent halo as satellite galaxies are accreted. Some environment-driven mechanisms consist of subhalo ISM removal (i.e. ram-pressure stripping; Gunn & Gott 1972; Einasto et al. 1974; Nulsen 1982) or inhibition of further star formation through the shutdown of cold gas accretion (e.g. starvation; Kawata & Mulchaey 2008). Other mechanisms qualify as mass-driven, meaning that some form of stellar and/or AGN feedback maintains the subhalo gas warm, preventing further star-formation (Dekel & Burkert 2014).

5.5.1 Environment-driven quenching

Observations have shown that satellite galaxies have higher quenched fractions and are older than central galaxies of the same M_* (e.g. Pasquali et al. 2010; Peng et al. 2012), a pair of results that highlights the role that the local environment plays in galaxy quenching. As we have emphasized in this paper, host halo mass is another key property, as satellites in massive host halos have increasingly older ages for $M_* < 10^{10.5} M_\odot$ and higher [Mg/Fe] at all M_*. Though this result has also been found in $M_* < 10^{10.5} M_\odot$ galaxies from SDSS (Pasquali et al. 2010; Gallazzi et al. 2020), we can now confirm that the trend of higher [Mg/Fe] in more massive halos exists at all masses in the range $M_* = 10^{9.5} - 10^{12} M_\odot$.

A possible explanation for the old ages of satellites in high M_h halos can be found in the "delayed-then-rapid" scenario. Through starvation and strangulation, massive halos can strip satellite galaxies from their cold and hot gas reservoirs, suppressing future star-formation (Larson et al. 1980; Kawata & Mulchaey 2008). These mechanisms are believed to act in timescales of 2-6 Gyr, after which the satellite galaxy rapidly quenches within 1 Gyr, keeping their stellar populations old (van den Bosch et al. 2008a; Wetzel et al. 2012, 2013; Fossati et al. 2017; Cora et al. 2019).

The increase in [Mg/Fe] and $\log Z/Z_\odot$ with M_h (seen here for [Mg/Fe] and first reported in Pasquali et al. 2010; Gallazzi et al. 2020 for both [Mg/Fe] and $\log Z/Z_\odot$) can be explained by variations in ISM enrichment. As the gas reservoirs in satellites are removed through ram-pressure stripping, starvation and strangulation, the accretion of low-metallicity gas is suppressed (Pasquali 2015; Bahé & McCarthy 2015). As a result, the star-forming gas in satellite galaxies is more metal-rich, enhancing the metal content of their stellar populations (Pasquali et al. 2012; Bahé et al. 2017).

In addition, tidal forces can strip M_* from satellite galaxies while leaving their stellar metallicities unaffected (Kang & van den Bosch 2008). In this scenario, satellites in high M_h halos would lose more M_*, causing them to show higher metallicites than expected for their M_* at $z = 0$ (Pasquali 2015). However, we should also note that ram-pressure and tidal stripping are thought to be more dominant at masses lower than the mass range of this work ($M_* < 10^8 M_\odot$; Weisz et al. 2015; Davies et al. 2016; Kawinwanichakij et al. 2017).

An implication of the "delayed-then-rapid" picture is that the time of quenching is dependent on the time of infall. Starvation and strangulation must trigger earlier in ancient

infallers ($T_{inf} > 5$; Pasquali et al. 2019) than in recent infallers ($T_{inf} < 2.5$; Pasquali et al. 2019). Ancient infallers also tend to orbit central galaxies in close-orbits, where the suppression of gas accretion is believed to peak (van de Voort et al. 2017; Cleland & McGee 2021). Indication of these trends has been reported in SDSS by Gallazzi et al. (2020), who found ancient infallers to have older ages, higher $\log Z/Z_{\odot}$, and greater [α/Fe] than recent infallers for $M_* \sim 10^{10} M_{\odot}$. However, this comparison was performed before separating satellites into star-forming and quiescent. In the second row of Figure 5.3, we showed that differences in age, [Fe/H], and [Mg/Fe] between ancient and recent infallers hold true after controlling for M_h and after removing star-forming galaxies, further supporting the "delayed-then-rapid" scenario for the quenching of $M_* \sim 10^{10} M_{\odot}$ satellites.

These results suggest that the ancient infaller subsample is ideal for testing the impact of host M_h on environment-driven quenching. Figures 5.3 and 5.5 show that ancient infallers in high M_h halos have older stellar ages, lower [Fe/H], and greater [Mg/Fe] than ancient infallers in low M_h halos. Gallazzi et al. (2020) also found the stellar ages and [α/Fe] of ancient infallers to correlate with host M_h, while also reporting that $\log Z/Z_{\odot}$ increases with M_h. Taken together, the trends in stellar age indicate that high M_h halos quench satellite galaxies earlier. The lower [Fe/H] and higher [Mg/Fe] (or [α/Fe]) in high M_h satellites reveal that they formed in shorter timescales. Finally, the results for $\log Z/Z_{\odot}$ could indicate that high M_h halos more efficiently suppress the accretion of low-metallicity gas (Gallazzi et al. 2020).

With respect to recent infallers ($T_{inf} < 2$), Gallazzi et al. (2020) found their assembly histories to show little dependence on host M_h. Their interpretation was that

recent infallers quenched through internal processes, long before they entered the virial radius of the parent halo ($T_q < T_{inf}$). In contrast with this result, we found the stellar ages of recent infallers to also increase with host M_h (Figure 5.3). In other work, recent infallers have been found to feature lower sSFR and older ages than field galaxies of the same M_* (Pasquali et al. 2019). In addition, Smith et al. (2019) found evidence that clusters impact the star-formation histories of satellite galaxies before they enter the virial radius of the host halo.

These observations seem at odds with the "delayed-then-rapid" picture for satellite quenching, but they fit very well with the idea of "pre-processing". In this mechanism, satellite cold gas reservoirs are heated up (i.e., evaporation) and/or warm subhalo gas is stripped (i.e. strangulation) by the hot ICM gas (Fujita 2004). These processes can suppress star-formation and limit the stellar mass build-up in satellite galaxies, sometimes even before they enter the virial radius of the host halo (Pallero et al. 2019). This scenario not only can explain the differences with host M_h in the populations of recent infallers, but also subtle variations in the quenched fraction of galaxies at large cluster-centric distances (Haines et al. 2015; Bianconi et al. 2018; van der Burg et al. 2018; Sarron et al. 2019; Sarron & Conselice 2021).

5.5.2 Mass-driven quenching and merger-driven growth

"Pre-processing" is not the only method through which satellites can quench before infall. Figures 5.3 and 5.5 reveal that the differences between the stellar ages of passive central and satellite galaxies decrease in magnitude at the highest M_*. The same trend was recovered by Pasquali et al. (2010) and Gallazzi et al. (2020) for stellar age and $\log Z/Z_\odot$.

Other work has shown that the quenched fractions of massive central and satellite galaxies are quite similar after M_h is controlled for (Bluck et al. 2016; Wang et al. 2020). These results are often interpreted as evidence that mass-driven quenching dominates at the high M_* end (e.g. Pasquali et al. 2010; Davies et al. 2016; Gallazzi et al. 2020; Li et al. 2020; Xie et al. 2020). In this picture, galaxy formation in deep potential wells can lead to runaway assembly that culminates in rapid quenching (Matteucci 1994; van Dokkum et al. 2009; Newman et al. 2010; Damjanov et al. 2011; Wellons et al. 2016; Zolotov et al. 2015), which is then maintained by stellar and/or AGN feedback (Dekel & Burkert 2014).

In this work some of the differences between centrals and satellites hold true even at the highest M_*. Figure 5.5 shows that satellites tend to have lower [Fe/H] than centrals at most radii between the centers and $1.5R_e$. Moreover, differences with M_h in the stellar ages and [Fe/H] of satellites are still present at the highest M_*, in contrast with Pasquali et al. (2010) and Gallazzi et al. (2020). The much larger samples by Pasquali et al. (2010) and Gallazzi et al. (2020) might suggest that our results are affected by sample variance at the highest M_* (N=25; see Table 5.1). Alternatively, these results could suggest that starvation and strangulation still play a major role at the highest M_*. Although no evidence supporting a galaxy environment-dependent IMF has been found (Rosani et al. 2018), another option is that differences in [Mg/Fe] are driven by IMF variations (e.g. Yan et al. 2021).

One more scenario to explain why massive satellites have lower [Fe/H] than massive centrals could be variations in the metal enrichment efficiency. Both central and satellite galaxies eject their metals back to the circum-galactic medium after their episodes of star-formation. Metal-enriched gas may then re-enter galaxies to fuel further episodes (Trager

et al. 2000; Schiavon et al. 2006; Wu et al. 2018; Chauke et al. 2019). The deeper gravitational potentials of centrals may enhance the efficiency of the gas "re-accretion" process, boosting their [Fe/H] and decreasing their [Mg/Fe]. This scenario is consistent with observations that residual star-formation in passive galaxies is more common at the highest M_* (Bundy et al. 2017).

Lastly, differences between the stellar populations of centrals and satellites could also originate from differences in their accretion histories (Shi et al. 2020). Most of the stellar content in massive central galaxies is thought to have formed *ex-situ* and later accreted (Oser et al. 2010, 2012; Johansson et al. 2012b; Moster et al. 2013; Rodriguez-Gomez et al. 2015; D'Souza & Bell 2018). A reasonable approximation for the characteristic difference between the M_* of the central and accreted satellites is $\Delta \log M_* \sim 0 - 0.5$ (e.g. Rodriguez-Gomez et al. 2016). Therefore, we can propose the simplistic model in which the building blocks of central galaxies of mass $\log M_*^{cen}$ are some average between satellites of $\log M_*^{sat} = \log M_*^{cen}$ and $\log M_*^{sat} = \log M_*^{cen} - 0.5$.

In practice, this means that the stellar populations of massive centrals (fifth column of Figure 5.5) should have values somewhere between the profiles of massive satellites (fifth column of Figure 5.5) and those of slightly less massive satellites (fourth column of Figure 5.5). Upon inspection of the figure, we can see that the stellar age, [Fe/H], and [Mg/Fe] profiles of massive centrals are consistent with this simple model. However, we must note that observations typically do not associate the impact of mergers to the centers of centrals, but with the outskirts instead ($R>R_e$; Huang et al. 2013b,a; Spindler & Wake 2017a; Oyarzún et al. 2019). Further exploration of this model will require quantitative tests

that account for the redistribution of metals in central galaxies, an analysis that we will leave for future work.

5.5.3 Inferences from the stellar population profiles

Several work have exploited spatially resolved spectroscopy to quantify how the stellar population gradients of nearby galaxies depend on local environment. So far, no conclusive evidence of an environmental dependence in the gradients has been found (Goddard et al. 2017b; Zheng et al. 2017; Santucci et al. 2020; Zhou et al. 2020). In Oyarzún et al. (2019), we advocated for analysis of the full extent of the profile, showing that gradients can "wash-out" trends in the data. For this reason, in this paper we compared the full extent of the stellar population profiles of central and satellite galaxies, and yet we still found little differences, at least for for $M_* > 10^{10} M_\odot$ (Figures 5.4 and 5.5). Collectively, all of these results suggest that environment-driven quenching operates on radial scales larger than the effective radii of $M_* > 10^{10} M_\odot$ galaxies.

The picture is different for $M_* < 10^{10} M_\odot$. In contrast to the flat age and [Mg/Fe] profiles of centrals at these M_*, the ages and [Mg/Fe] of satellites increase with radius (Figure 5.6). The trend is more prominent for satellites in close-orbits around massive halos, hinting satellite quenching in the outskirts is driven by the host halo. This result may be the manifestation of other patterns observed in the SAMI (Allen et al. 2015) and MaNGA surveys, like suppression of star-formation (Schaefer et al. 2017) and deficit of M_* (Spindler & Wake 2017a) in the outskirts of satellite galaxies. At the same time, a degree of environmental quenching also seems to occur from the "inside-out" (Lin et al. 2019), highly suggestive that multiple suppression mechanisms are at play. Further study of even lower

mass galaxies have the potential to better tease out these mechanisms.

5.6 Summary

In this work, we took advantage of the sample size and radial coverage of the MaNGA survey to compute high signal-to-noise stacked spectra for central and satellite galaxies out to $1.5R_e$. By using the stellar population fitting code `alf` and the Tinker (2020b) group catalog, we were able to constrain the stellar age, [Fe/H], and [Mg/Fe] profiles of centrals and satellite galaxies as a function of M_*, M_h, and cluster-centric distance. We found the following:

1. Satellites are older ($\sim 1-2$ Gyr) and show greater [Mg/Fe] (~ 0.2 dex) than centrals at all radii within $1.5R_e$ and at all stellar masses in the range $M_* = 10^{9.5}-10^{10.5}M_\odot$. These results agree with differences reported in previous work (e.g. Pasquali et al. 2010; Gallazzi et al. 2020).

2. The stellar populations of close-orbit satellites strongly depend on the mass of the host halo. Close-orbit satellites in high M_h halos have older ages, lower [Fe/H], and greater [Mg/Fe] than counterparts in low M_h halos. These results indicate that massive halos quench satellites earlier and more rapidly.

3. The stellar populations of far-orbit satellites (recent infallers) also depend on host M_h. Far-orbit satellites in high M_h halos have older ages and lower [Fe/H] than counterparts in low M_h halos. These results are consistent with environmental "pre-processing", i.e., the idea that satellite star-formation can be suppressed before the galaxy enters the virial radius of the current host halo.

4. The stellar ages of centrals and satellites are comparable ($>$ 10 Gyr) at the highest M_* ($> 10^{11.5} M_\odot$). As in previous work (Pasquali et al. 2010; Gallazzi et al. 2020), we associate this result to internal (mass-driven) satellite quenching.

5. Even at the highest M_*, satellites have lower [Fe/H] and higher [Mg/Fe] than centrals at all radii between the centers and $1.5 R_e$. We propose various scenarios to explain these results, including differences in metal-enrichment, IMF variations, and galaxy mergers. Another possibility is sample variance, since our satellite sample is small at these M_* ($N = 25$).

6. In agreement with previous work, we find no significant differences between the shape of the stellar population profiles of central and satellite galaxies for $M > 10^{10} M_\odot$. We conclude that the lasting impact of environment on the shape of the stellar population profiles is very subtle at these M_*.

7. Differences in the stellar population profiles are apparent for $M_* = 10^{9.5} - 10^{10} M_\odot$. Centrals have flat age and [Mg/Fe] profiles, whereas the ages and [Mg/Fe] of satellites increase with radius. The difference grows in magnitude as host M_h increases, suggesting that the host halo is driving the quenching of satellites in the outskirts. This result fits well with evidence of "outside-in" quenching of satellites in dense environments (Schaefer et al. 2017).

Chapter 6

Conclusion

Early-type galaxies are the most massive galaxies in the Universe, and yet their formation history continues to be hotly debated. Did they form all at once long ago, or have they been steadily assembling their stars over time? In this Thesis, I used new, statistically powerful MaNGA (Bundy et al. 2015) observations coupled with state-of-the-art modeling to trace the assembly of nearby galaxies back in time. I found observational evidence that the assembly of early-type galaxies is closely connected with the growth of their host dark-matter halos, a key feature of our current cosmological model (ΛCDM; Blumenthal et al. 1984).

In Chapter 2, I showed that massive ($M_* > 10^{11} M_\odot$) early-type galaxies in MaNGA contain signatures of minor mergers, a key feature of late-time halo growth. The evidence comes from flattening of the stellar metallicity profile beyond the effective radius, a feature predicted in hydrodynamical simulations (Cook et al. 2016). This is one of the first detections of merger signatures in galaxy stellar populations.

Future work could quantify whether the flattening of the metallicity profile is dependent on the local environment. Perhaps the expectation is to find an enhanced flattening of the metallicity profile in denser environments, yet it is unclear if the local environment of galaxies today is representative of the surroundings at the peak of merger-driven growth. Perhaps more telling would be to test if the profile flattening shows any dependence on effective radius at fixed stellar mass, indicating whether merger-driven growth is indeed responsible for the large sizes of nearby early-types.

Alternatively, the evolution with redshift of the sizes of early-type galaxies could be the result of the *progenitor bias* effect. Highly concentrated halos are believed to collapse at earlier times, which results in the average effective radii of galaxies to decrease as redshift increases (e.g. Poggianti et al. 2013). Discerning between merger growth and progenitor bias requires spectroscopy of "red nuggets", since the spectral response to age variations in early-type galaxies is too subtle for photometry (Conroy 2013). Such characterization will greatly benefit from the launch of JWST, with spectroscopic observations for a dozen of "red nuggets" set to become publicly available (Kriek et al. 2021).

Although we might not know whether stellar accretion or *progenitor bias* is the dominant mechanism, what we do know is that halos indeed shape the assembly histories of central galaxies (Chapter 3). At fixed stellar mass, centrals in more massive halos are older, show lower [Fe/H], and have higher [Mg/Fe]. In fact, it makes sense to think of halo mass as a more fundamental property than stellar mass, at least from a theoretical perspective. In halos of the same mass today, centrals of higher M_* are older and formed their stars more rapidly. This result is suggestive of galaxy assembly bias, the prediction that high M_*

centrals assemble in early-forming, highly concentrated halos.

I built upon this result in Chapter 4 by quantifying how the M_* and M_h of passive central galaxies in SDSS depend on halo formation time. To this end, I used the normalized environmental density within 10 Mpc (δ_{10}) as a proxy for halo age (Alpaslan & Tinker 2020). I found that high M_* centrals have higher δ_{10}, implying that they formed in older dark-matter halos. This result is perhaps the most significant evidence of galaxy assembly bias to date. In the upcoming years, surveys like DESI (DESI Collaboration et al. 2016) will further probe the nature and significance of galaxy assembly bias. The BGS sample of DESI will yield spectra for 10 million galaxies in the range $0 < z < 0.4$, twenty times as many galaxies as in the MAIN SDSS sample. For example, we will be able to quantify how the magnitude of assembly bias depends on galaxy properties like color (i.e., red or blue) and redshift ($0 < z < 0.4$). These characterizations will not only reveal the details of how galaxy formation and halo assembly are connected, but also improve our cosmological probes (i.e. halo occupation models; e.g. Zentner et al. 2014).

In general, studies of the galaxy-halo connection are based on using M_* as a proxy to relate to M_h (e.g. Tinker 2020a). However, variations in the stellar initial mass function (IMF) could have serious implications on this assumption, potentially biasing our M_* by factors two to three (e.g. Conroy 2013). Future work can exploit the rich MaNGA dataset to exhaustively characterize the IMF in nearby galaxies. A key open question in this field is whether the IMF depends on local environment. Are processes unique to satellites, like rapid energy exchanges in a turbulent ISM, relevant to the IMF? (e.g. Hopkins 2013). Since we know that the stellar population parameters of satellite galaxies can strongly depend

on properties like stellar mass, host halo mass, and galactocentric distance (Chapter 5), analyses of this kind will require sophisticated stellar population characterization tools like the program `alf` (Conroy & van Dokkum 2012; Conroy et al. 2018).

Bibliography

Adelman-McCarthy, J. K., Agüeros, M. A., Allam, S. S., et al. 2006, ApJS, 162, 38

Aguado, D. S., Ahumada, R., Almeida, A., et al. 2019, ApJS, 240, 23

Aihara, H., Allende Prieto, C., An, D., et al. 2011, ApJS, 193, 29

Alam, S., Albareti, F. D., Allende Prieto, C., et al. 2015, ApJS, 219, 12

Allen, J. T., Croom, S. M., Konstantopoulos, I. S., et al. 2015, MNRAS, 446, 1567

Alpaslan, M., & Tinker, J. L. 2020, MNRAS, 496, 5463

Alton, P. D., Smith, R. J., & Lucey, J. R. 2018, MNRAS, 478, 4464

Argudo-Fernández, M., Verley, S., Bergond, G., et al. 2015, A&A, 578, A110

Arimoto, N., & Yoshii, Y. 1987, A&A, 173, 23

Bahé, Y. M., & McCarthy, I. G. 2015, MNRAS, 447, 969

Bahé, Y. M., Schaye, J., Crain, R. A., et al. 2017, MNRAS, 464, 508

Balogh, M. L., & Morris, S. L. 2000, MNRAS, 318, 703

Barro, G., Faber, S. M., Pérez-González, P. G., et al. 2013, ApJ, 765, 104

Behroozi, P., Wechsler, R. H., Hearin, A. P., & Conroy, C. 2019, MNRAS, 488, 3143

Behroozi, P. S., Wechsler, R. H., & Conroy, C. 2013, ApJL, 762, L31

Belfiore, F., Maiolino, R., Maraston, C., et al. 2016, MNRAS, 461, 3111

Belfiore, F., Westfall, K. B., Schaefer, A., et al. 2019, AJ, 158, 160

Benson, A. J., Cole, S., Frenk, C. S., Baugh, C. M., & Lacey, C. G. 2000, MNRAS, 311, 793

Berlind, A. A., Kazin, E., Blanton, M. R., et al. 2006, arXiv e-prints, astro

Bernardi, M., Meert, A., Sheth, R. K., et al. 2013, MNRAS, 436, 697

Bezanson, R., van Dokkum, P. G., Tal, T., et al. 2009, ApJ, 697, 1290

Bianconi, M., Smith, G. P., Haines, C. P., et al. 2018, MNRAS, 473, L79

Blanton, M. R., Eisenstein, D., Hogg, D. W., Schlegel, D. J., & Brinkmann, J. 2005a, ApJ, 629, 143

Blanton, M. R., Kazin, E., Muna, D., Weaver, B. A., & Price-Whelan, A. 2011, AJ, 142, 31

Blanton, M. R., & Roweis, S. 2007, AJ, 133, 734

Blanton, M. R., Hogg, D. W., Bahcall, N. A., et al. 2003, ApJ, 594, 186

Blanton, M. R., Schlegel, D. J., Strauss, M. A., et al. 2005b, AJ, 129, 2562

Blanton, M. R., Bershady, M. A., Abolfathi, B., et al. 2017, AJ, 154, 28

Bluck, A. F. L., Maiolino, R., Sánchez, S. F., et al. 2020, MNRAS, 492, 96

Bluck, A. F. L., Mendel, J. T., Ellison, S. L., et al. 2016, MNRAS, 462, 2559

Blumenthal, G. R., Faber, S. M., Primack, J. R., & Rees, M. J. 1984, Nature, 311, 517

Booth, C. M., & Schaye, J. 2010, MNRAS, 405, L1

Bradshaw, C., Leauthaud, A., Hearin, A., Huang, S., & Behroozi, P. 2020, MNRAS, 493, 337

Bressan, A., Chiosi, C., & Fagotto, F. 1994, ApJS, 94, 63

Brinchmann, J., Charlot, S., White, S. D. M., et al. 2004, MNRAS, 351, 1151

Bruzual, G., & Charlot, S. 2003, MNRAS, 344, 1000

Buitrago, F., Trujillo, I., Conselice, C. J., et al. 2008, ApJL, 687, L61

Bundy, K., Leauthaud, A., Saito, S., et al. 2017, ApJ, 851, 34

Bundy, K., Bershady, M. A., Law, D. R., et al. 2015, ApJ, 798, 7

Calderon, V. F., Berlind, A. A., & Sinha, M. 2018, MNRAS, 480, 2031

Campbell, D., van den Bosch, F. C., Hearin, A., et al. 2015, MNRAS, 452, 444

Cappellari, M. 2017, MNRAS, 466, 798

Cappellari, M., & Emsellem, E. 2004, PASP, 116, 138

Cappellari, M., McDermid, R. M., Alatalo, K., et al. 2013, MNRAS, 432, 1862

Carollo, C. M., Danziger, I. J., & Buson, L. 1993, MNRAS, 265, 553

Carollo, C. M., Bschorr, T. J., Renzini, A., et al. 2013, ApJ, 773, 112

Cassata, P., Giavalisco, M., Guo, Y., et al. 2010, ApJL, 714, L79

—. 2011, ApJ, 743, 96

Chabrier, G. 2003, PASP, 115, 763

Chauke, P., van der Wel, A., Pacifici, C., et al. 2019, ApJ, 877, 48

Chen, Y.-M., Kauffmann, G., Tremonti, C. A., et al. 2012, MNRAS, 421, 314

Chen, Z., Faber, S. M., Koo, D. C., et al. 2020, ApJ, 897, 102

Cherinka, B., Andrews, B. H., Sánchez-Gallego, J., et al. 2019, AJ, 158, 74

Choi, J., Dotter, A., Conroy, C., et al. 2016, ApJ, 823, 102

Cid Fernandes, R., Mateus, A., Sodré, L., Stasińska, G., & Gomes, J. M. 2005, MNRAS, 358, 363

Cid Fernandes, R., Stasińska, G., Mateus, A., & Vale Asari, N. 2011, MNRAS, 413, 1687

Cimatti, A., Cassata, P., Pozzetti, L., et al. 2008, A&A, 482, 21

Cleland, C., & McGee, S. L. 2021, MNRAS, 500, 590

Comparat, J., Maraston, C., Goddard, D., et al. 2017, ArXiv e-prints, arXiv:1711.06575

Conroy, C. 2013, ARA&A, 51, 393

Conroy, C., Graves, G. J., & van Dokkum, P. G. 2014, ApJ, 780, 33

Conroy, C., & Gunn, J. E. 2010, ApJ, 712, 833

Conroy, C., Gunn, J. E., & White, M. 2009, ApJ, 699, 486

Conroy, C., & van Dokkum, P. 2012, ApJ, 747, 69

Conroy, C., Villaume, A., van Dokkum, P. G., & Lind, K. 2018, ApJ, 854, 139

Contini, E., Gu, Q., Kang, X., Rhee, J., & Yi, S. K. 2019, ApJ, 882, 167

Contreras, S., Angulo, R. E., & Zennaro, M. 2021, MNRAS, arXiv:2005.03672

Contreras, S., Zehavi, I., Padilla, N., et al. 2019, MNRAS, 484, 1133

Cook, B. A., Conroy, C., Pillepich, A., Rodriguez-Gomez, V., & Hernquist, L. 2016, ApJ, 833, 158

Cooper, A. P., Parry, O. H., Lowing, B., Cole, S., & Frenk, C. 2015, MNRAS, 454, 3185

Cora, S. A., Hough, T., Vega-Martínez, C. A., & Orsi, Á. A. 2019, MNRAS, 483, 1686

Correa, C. A., Wyithe, J. S. B., Schaye, J., & Duffy, A. R. 2015, MNRAS, 450, 1521

Crain, R. A., Schaye, J., Bower, R. G., et al. 2015, MNRAS, 450, 1937

Crook, A. C., Huchra, J. P., Martimbeau, N., et al. 2007, ApJ, 655, 790

Croton, D. J., Gao, L., & White, S. D. M. 2007, MNRAS, 374, 1303

Daddi, E., Renzini, A., Pirzkal, N., et al. 2005, ApJ, 626, 680

Damjanov, I., McCarthy, P. J., Abraham, R. G., et al. 2009, ApJ, 695, 101

Damjanov, I., Abraham, R. G., Glazebrook, K., et al. 2011, ApJL, 739, L44

Davidzon, I., Cucciati, O., Bolzonella, M., et al. 2016, A&A, 586, A23

Davies, L. J. M., Robotham, A. S. G., Driver, S. P., et al. 2016, MNRAS, 455, 4013

Davies, L. J. M., Robotham, A. S. G., Lagos, C. d. P., et al. 2019, MNRAS, 483, 5444

Davis, M., Efstathiou, G., Frenk, C. S., & White, S. D. M. 1985, ApJ, 292, 371

Dawson, K. S., Schlegel, D. J., Ahn, C. P., et al. 2013, AJ, 145, 10

De Lucia, G., & Blaizot, J. 2007, MNRAS, 375, 2

De Lucia, G., Weinmann, S., Poggianti, B. M., Aragón-Salamanca, A., & Zaritsky, D. 2012, MNRAS, 423, 1277

Dekel, A., & Birnboim, Y. 2006, MNRAS, 368, 2

Dekel, A., & Burkert, A. 2014, MNRAS, 438, 1870

DESI Collaboration, Aghamousa, A., Aguilar, J., et al. 2016, arXiv e-prints, arXiv:1611.00036

Dey, A., Schlegel, D. J., Lang, D., et al. 2019, AJ, 157, 168

Di Matteo, P., Pipino, A., Lehnert, M. D., Combes, F., & Semelin, B. 2009, A&A, 499, 427

Diaz, J., Bekki, K., Forbes, D. A., et al. 2018, MNRAS, 477, 2030

Djorgovski, S., & Davis, M. 1987, ApJ, 313, 59

D'Onofrio, M., & Chiosi, C. 2021, arXiv e-prints, arXiv:2112.03574

Dotter, A. 2016, ApJS, 222, 8

Dressler, A. 1980, ApJ, 236, 351

Dressler, A., Lynden-Bell, D., Burstein, D., et al. 1987, ApJ, 313, 42

Drory, N., MacDonald, N., Bershady, M. A., et al. 2015, AJ, 149, 77

D'Souza, R., & Bell, E. F. 2018, MNRAS, 474, 5300

D'Souza, R., Kauffman, G., Wang, J., & Vegetti, S. 2014, MNRAS, 443, 1433

Dunkley, J., Komatsu, E., Nolta, M. R., et al. 2009, ApJS, 180, 306

Eggen, O. J., Lynden-Bell, D., & Sandage, A. R. 1962, ApJ, 136, 748

Einasto, J., Saar, E., Kaasik, A., & Chernin, A. D. 1974, Nature, 252, 111

El-Badry, K., Wetzel, A., Geha, M., et al. 2016, ApJ, 820, 131

Estrada-Carpenter, V., Papovich, C., Momcheva, I., et al. 2020, ApJ, 898, 171

Faber, S. M., Friel, E. D., Burstein, D., & Gaskell, C. M. 1985, ApJS, 57, 711

Faber, S. M., & Jackson, R. E. 1976a, ApJ, 204, 668

—. 1976b, ApJ, 204, 668

Fan, L., Lapi, A., Bressan, A., et al. 2010, ApJ, 718, 1460

Fan, L., Lapi, A., De Zotti, G., & Danese, L. 2008, ApJL, 689, L101

Fernández-Trincado, J. G., Beers, T. C., & Minniti, D. 2020, A&A, 644, A83

Fernández-Trincado, J. G., Beers, T. C., Placco, V. M., et al. 2019, ApJL, 886, L8

Fillingham, S. P., Cooper, M. C., Wheeler, C., et al. 2015, MNRAS, 454, 2039

Foreman-Mackey, D., Hogg, D. W., Lang, D., & Goodman, J. 2013, PASP, 125, 306

Fossati, M., Wilman, D. J., Mendel, J. T., et al. 2017, ApJ, 835, 153

Franx, M., van Dokkum, P. G., Förster Schreiber, N. M., et al. 2008, ApJ, 688, 770

Fraser-McKelvie, A., Aragón-Salamanca, A., Merrifield, M., et al. 2018, MNRAS, 481, 5580

Fujita, Y. 2004, PASJ, 56, 29

Furlong, M., Bower, R. G., Crain, R. A., et al. 2017, MNRAS, 465, 722

Gallazzi, A., Charlot, S., Brinchmann, J., White, S. D. M., & Tremonti, C. A. 2005, MNRAS, 362, 41

Gallazzi, A. R., Pasquali, A., Zibetti, S., & La Barbera, F. 2020, arXiv e-prints, arXiv:2010.04733

Gao, L., Springel, V., & White, S. D. M. 2005, MNRAS, 363, L66

García-Benito, R., González Delgado, R. M., Pérez, E., et al. 2017, A&A, 608, A27

Genel, S., Nelson, D., Pillepich, A., et al. 2018, MNRAS, 474, 3976

Girelli, G., Pozzetti, L., Bolzonella, M., et al. 2020, A&A, 634, A135

Goddard, D., Thomas, D., Maraston, C., et al. 2017a, MNRAS, 466, 4731

—. 2017b, MNRAS, 465, 688

González Delgado, R. M., Cid Fernandes, R., García-Benito, R., et al. 2014, ApJL, 791, L16

González Delgado, R. M., García-Benito, R., Pérez, E., et al. 2015, A&A, 581, A103

Graham, A. W., Dullo, B. T., & Savorgnan, G. A. D. 2015, ApJ, 804, 32

Graham, M. T., Cappellari, M., Li, H., et al. 2018, MNRAS, 477, 4711

Graves, G. J., Faber, S. M., & Schiavon, R. P. 2009, ApJ, 698, 1590

Greene, J. E., Janish, R., Ma, C.-P., et al. 2015, ApJ, 807, 11

Greene, J. E., Murphy, J. D., Graves, G. J., et al. 2013, ApJ, 776, 64

Greene, J. E., Veale, M., Ma, C.-P., et al. 2019, ApJ, 874, 66

Gunn, J. E., & Gott, J. Richard, I. 1972, ApJ, 176, 1

Gunn, J. E., Siegmund, W. A., Mannery, E. J., et al. 2006, AJ, 131, 2332

Haines, C. P., Pereira, M. J., Smith, G. P., et al. 2015, ApJ, 806, 101

Hearin, A. P., Zentner, A. R., van den Bosch, F. C., Campbell, D., & Tollerud, E. 2016, MNRAS, 460, 2552

Hirschmann, M., Naab, T., Ostriker, J. P., et al. 2015, MNRAS, 449, 528

Hopkins, P. F. 2013, MNRAS, 433, 170

Hopkins, P. F., Bundy, K., Hernquist, L., Wuyts, S., & Cox, T. J. 2010a, MNRAS, 401, 1099

Hopkins, P. F., Hernquist, L., Cox, T. J., Dutta, S. N., & Rothberg, B. 2008, ApJ, 679, 156

Hopkins, P. F., Bundy, K., Croton, D., et al. 2010b, ApJ, 715, 202

Huang, S., Ho, L. C., Peng, C. Y., Li, Z.-Y., & Barth, A. J. 2013a, ApJL, 768, L28

—. 2013b, ApJ, 766, 47

Huang, S., Leauthaud, A., Greene, J. E., et al. 2018, MNRAS, 475, 3348

Huang, S., Leauthaud, A., Hearin, A., et al. 2020, MNRAS, 492, 3685

Jian, H.-Y., Lin, L., Lin, K.-Y., et al. 2017, ApJ, 845, 74

Johansson, J., Thomas, D., & Maraston, C. 2012a, MNRAS, 421, 1908

Johansson, P. H., Naab, T., & Ostriker, J. P. 2012b, ApJ, 754, 115

Johnson, B. D., Leja, J., Conroy, C., & Speagle, J. S. 2020, arXiv e-prints, arXiv:2012.01426

Johnston, E. J., Aragón-Salamanca, A., & Merrifield, M. R. 2014, MNRAS, 441, 333

Johnston, E. J., Aragón-Salamanca, A., Merrifield, M. R., & Bedregal, A. G. 2012, MNRAS, 422, 2590

Johnston, E. J., Merrifield, M., & Aragón-Salamanca, A. 2018, MNRAS, 478, 4255

Kang, X., & van den Bosch, F. C. 2008, ApJL, 676, L101

Kannappan, S. J., Guie, J. M., & Baker, A. J. 2009, AJ, 138, 579

Kauffmann, G., Li, C., Zhang, W., & Weinmann, S. 2013, MNRAS, 430, 1447

Kauffmann, G., White, S. D. M., Heckman, T. M., et al. 2004, MNRAS, 353, 713

Kawata, D., & Mulchaey, J. S. 2008, ApJL, 672, L103

Kawinwanichakij, L., Papovich, C., Quadri, R. F., et al. 2017, ApJ, 847, 134

Kirby, E. N., Guhathakurta, P., & Sneden, C. 2008, ApJ, 682, 1217

Klypin, A., Yepes, G., Gottlöber, S., Prada, F., & Heß, S. 2016, MNRAS, 457, 4340

Knobel, C., Lilly, S. J., Woo, J., & Kovač, K. 2015, ApJ, 800, 24

Kobayashi, C. 2004, MNRAS, 347, 740

Kriek, M., & Conroy, C. 2013, ApJL, 775, L16

Kriek, M., Beverage, A. G., Barro, G., et al. 2021, Ultra-deep continuum spectroscopy of quiescent galaxies at 1.0, JWST Proposal. Cycle 1, ,

Kroupa, P. 2001, MNRAS, 322, 231

Kulier, A., Padilla, N., Schaye, J., et al. 2019, MNRAS, 482, 3261

Kuntschner, H. 2015, in IAU Symposium, Vol. 311, Galaxy Masses as Constraints of Formation Models, ed. M. Cappellari & S. Courteau, 53–56

Kuntschner, H., Emsellem, E., Bacon, R., et al. 2010, MNRAS, 408, 97

Kurucz, R. L. 2018, in Astronomical Society of the Pacific Conference Series, Vol. 515, Workshop on Astrophysical Opacities, 47

La Barbera, F., de Carvalho, R. R., Gal, R. R., et al. 2005, ApJL, 626, L19

La Barbera, F., Ferreras, I., de Carvalho, R. R., et al. 2011, ApJL, 740, L41

La Barbera, F., Pasquali, A., Ferreras, I., et al. 2014, MNRAS, 445, 1977

Lacerna, I., Ibarra-Medel, H., Avila-Reese, V., et al. 2020, A&A, 644, A117

Lacerna, I., Padilla, N., & Stasyszyn, F. 2014, MNRAS, 443, 3107

Lackner, C. N., Cen, R., Ostriker, J. P., & Joung, M. R. 2012, MNRAS, 425, 641

Larson, R. B. 1974, MNRAS, 169, 229

Larson, R. B., Tinsley, B. M., & Caldwell, C. N. 1980, ApJ, 237, 692

Law, D. R., Yan, R., Bershady, M. A., et al. 2015, AJ, 150, 19

Law, D. R., Cherinka, B., Yan, R., et al. 2016, AJ, 152, 83

Law, D. R., Westfall, K. B., Bershady, M. A., et al. 2021, AJ, 161, 52

Leauthaud, A., Saito, S., Hilbert, S., et al. 2017, MNRAS, 467, 3024

Lehmann, B. V., Mao, Y.-Y., Becker, M. R., Skillman, S. W., & Wechsler, R. H. 2017, ApJ, 834, 37

Leja, J., Carnall, A. C., Johnson, B. D., Conroy, C., & Speagle, J. S. 2019, ApJ, 876, 3

Leja, J., Johnson, B. D., Conroy, C., van Dokkum, P. G., & Byler, N. 2017, ApJ, 837, 170

Li, H., Mao, S., Cappellari, M., et al. 2018, MNRAS, 476, 1765

Li, P., Wang, H., Mo, H. J., Wang, E., & Hong, H. 2020, arXiv e-prints, arXiv:2003.09776

Li, Y., Mo, H. J., & Gao, L. 2008, MNRAS, 389, 1419

Lin, L., Hsieh, B.-C., Pan, H.-A., et al. 2019, ApJ, 872, 50

Lin, Y.-T., Mandelbaum, R., Huang, Y.-H., et al. 2016, ApJ, 819, 119

Lynden-Bell, D. 1967, MNRAS, 136, 101

Mandelbaum, R., Wang, W., Zu, Y., et al. 2016, MNRAS, 457, 3200

Mansfield, P., & Kravtsov, A. V. 2020, MNRAS, 493, 4763

Mao, Y.-Y., Zentner, A. R., & Wechsler, R. H. 2017, ArXiv e-prints, arXiv:1705.03888

Maraston, C., & Strömbäck, G. 2011, MNRAS, 418, 2785

Martín-Navarro, I., Vazdekis, A., Falcón-Barroso, J., et al. 2018, MNRAS, 475, 3700

Matteucci, F. 1994, A&A, 288, 57

Matthee, J., Schaye, J., Crain, R. A., et al. 2017, MNRAS, 465, 2381

Mayer, L., Governato, F., Colpi, M., et al. 2001, ApJ, 559, 754

Mayer, L., Mastropietro, C., Wadsley, J., Stadel, J., & Moore, B. 2006, MNRAS, 369, 1021

McDermid, R. M., Alatalo, K., Blitz, L., et al. 2015, MNRAS, 448, 3484

Minchev, I., Famaey, B., Quillen, A. C., et al. 2012, A&A, 548, A126

Montero-Dorta, A. D., Chaves-Montero, J., Artale, M. C., & Favole, G. 2021, arXiv e-prints, arXiv:2105.05274

Montero-Dorta, A. D., Pérez, E., Prada, F., et al. 2017, ApJL, 848, L2

Montero-Dorta, A. D., Artale, M. C., Abramo, L. R., et al. 2020, MNRAS, 496, 1182

Moster, B. P., Naab, T., & White, S. D. M. 2013, MNRAS, 428, 3121

Moster, B. P., Somerville, R. S., Maulbetsch, C., et al. 2010, ApJ, 710, 903

Moustakas, J., Kennicutt, Robert C., J., & Tremonti, C. A. 2006, ApJ, 642, 775

Naab, T., Oser, L., Emsellem, E., et al. 2014, MNRAS, 444, 3357

Nair, P. B., & Abraham, R. G. 2010, ApJS, 186, 427

Neistein, E., van den Bosch, F. C., & Dekel, A. 2006, MNRAS, 372, 933

Nelson, D., Pillepich, A., Genel, S., et al. 2015, Astronomy and Computing, 13, 12

Newman, A. B., Ellis, R. S., Treu, T., & Bundy, K. 2010, ApJL, 717, L103

Nipoti, C., Londrillo, P., & Ciotti, L. 2003, MNRAS, 342, 501

Nulsen, P. E. J. 1982, MNRAS, 198, 1007

Oke, J. B., & Gunn, J. E. 1983, ApJ, 266, 713

Oser, L., Naab, T., Ostriker, J. P., & Johansson, P. H. 2012, ApJ, 744, 63

Oser, L., Ostriker, J. P., Naab, T., Johansson, P. H., & Burkert, A. 2010, ApJ, 725, 2312

Oyarzún, G. A., Blanc, G. A., González, V., Mateo, M., & Bailey, John I., I. 2017, ApJ, 843, 133

Oyarzún, G. A., Bundy, K., Westfall, K. B., et al. 2019, ApJ, 880, 111

Pallero, D., Gómez, F. A., Padilla, N. D., et al. 2019, MNRAS, 488, 847

Parikh, T., Thomas, D., Maraston, C., et al. 2021, arXiv e-prints, arXiv:2102.06703

—. 2018, MNRAS, 477, 3954

—. 2019, MNRAS, 483, 3420

Pasquali, A. 2015, Astronomische Nachrichten, 336, 505

Pasquali, A., Gallazzi, A., Fontanot, F., et al. 2010, MNRAS, 407, 937

Pasquali, A., Gallazzi, A., & van den Bosch, F. C. 2012, Monthly Notices of the Royal Astronomical Society, 425, 273

Pasquali, A., Smith, R., Gallazzi, A., et al. 2019, MNRAS, 484, 1702

Peng, C. Y., Ho, L. C., Impey, C. D., & Rix, H.-W. 2010a, AJ, 139, 2097

Peng, Y.-j., Lilly, S. J., Renzini, A., & Carollo, M. 2012, ApJ, 757, 4

Peng, Y.-j., Lilly, S. J., Kovač, K., et al. 2010b, ApJ, 721, 193

Pillepich, A., Vogelsberger, M., Deason, A., et al. 2014, MNRAS, 444, 237

Pillepich, A., Springel, V., Nelson, D., et al. 2018, MNRAS, 473, 4077

Pintos-Castro, I., Yee, H. K. C., Muzzin, A., Old, L., & Wilson, G. 2019, ApJ, 876, 40

Pipino, A., D'Ercole, A., Chiappini, C., & Matteucci, F. 2010, MNRAS, 407, 1347

Poggianti, B. M., Calvi, R., Bindoni, D., et al. 2013, ApJ, 762, 77

Posti, L., & Fall, S. M. 2021, arXiv e-prints, arXiv:2102.11282

Prada, F., Klypin, A. A., Cuesta, A. J., Betancort-Rijo, J. E., & Primack, J. 2012, MNRAS, 423, 3018

Rawle, T. D., Smith, R. J., & Lucey, J. R. 2010, MNRAS, 401, 852

Read, J. I., Wilkinson, M. I., Evans, N. W., Gilmore, G., & Kleyna, J. T. 2006, MNRAS, 366, 429

Renzini, A. 2006, ARA&A, 44, 141

Rodriguez-Gomez, V., Genel, S., Vogelsberger, M., et al. 2015, MNRAS, 449, 49

Rodriguez-Gomez, V., Pillepich, A., Sales, L. V., et al. 2016, MNRAS, 458, 2371

Rodríguez-Puebla, A., Primack, J. R., Avila-Reese, V., & Faber, S. M. 2017, MNRAS, 470, 651

Roig, B., Blanton, M. R., & Yan, R. 2015, ApJ, 808, 26

Rosani, G., Pasquali, A., La Barbera, F., Ferreras, I., & Vazdekis, A. 2018, MNRAS, 476, 5233

Saha, K., & Cortesi, A. 2018, ApJL, 862, L12

Salpeter, E. E. 1955, ApJ, 121, 161

Sánchez, S. F., Kennicutt, R. C., Gil de Paz, A., et al. 2012, A&A, 538, A8

Sánchez, S. F., Pérez, E., Sánchez-Blázquez, P., et al. 2016, RMxAA, 52, 171

Sánchez, S. F., Avila-Reese, V., Hernandez-Toledo, H., et al. 2018, RMxAA, 54, 217

Sánchez-Blázquez, P., Forbes, D. A., Strader, J., Brodie, J., & Proctor, R. 2007, MNRAS, 377, 759

Sánchez-Blázquez, P., Peletier, R. F., Jiménez-Vicente, J., et al. 2006, MNRAS, 371, 703

Sandage, A., Freeman, K. C., & Stokes, N. R. 1970, ApJ, 160, 831

Santucci, G., Brough, S., Scott, N., et al. 2020, arXiv e-prints, arXiv:2005.00541

Sarron, F., Adami, C., Durret, F., & Laigle, C. 2019, A&A, 632, A49

Sarron, F., & Conselice, C. J. 2021, MNRAS, 506, 2136

Schaefer, A. L., Croom, S. M., Allen, J. T., et al. 2017, MNRAS, 464, 121

Schaye, J., Crain, R. A., Bower, R. G., et al. 2015, MNRAS, 446, 521

Schiavon, R. P. 2007, ApJS, 171, 146

Schiavon, R. P., Faber, S. M., Konidaris, N., et al. 2006, ApJL, 651, L93

Scholz-Díaz, L., Martín-Navarro, I., & Falcón-Barroso, J. 2022, MNRAS, 511, 4900

Scott, N., Brough, S., Croom, S. M., et al. 2017, MNRAS, 472, 2833

Shi, J., Wang, H., Mo, H., et al. 2020, ApJ, 893, 139

Smee, S. A., Gunn, J. E., Uomoto, A., et al. 2013, AJ, 146, 32

Smith, R., Pacifici, C., Pasquali, A., & Calderón-Castillo, P. 2019, ApJ, 876, 145

Somerville, R. S., & Davé, R. 2015, ARA&A, 53, 51

Speagle, J. S. 2019, arXiv e-prints, arXiv:1904.02180

Spergel, D. N., Bean, R., Doré, O., et al. 2007, ApJS, 170, 377

Spindler, A., & Wake, D. 2017a, MNRAS, 468, 333

—. 2017b, MNRAS, 468, 333

Spolaor, M., Proctor, R. N., Forbes, D. A., & Couch, W. J. 2009, ApJL, 691, L138

Szomoru, D., Franx, M., van Dokkum, P. G., et al. 2013, ApJ, 763, 73

Taranu, D., Dubinski, J., & Yee, H. K. C. 2015, ApJ, 803, 78

Taylor, P., & Kobayashi, C. 2017, MNRAS, 471, 3856

Thomas, D., Maraston, C., & Bender, R. 2003, MNRAS, 339, 897

Thomas, D., Maraston, C., Bender, R., & Mendes de Oliveira, C. 2005, ApJ, 621, 673

Thomas, D., Maraston, C., Schawinski, K., Sarzi, M., & Silk, J. 2010, MNRAS, 404, 1775

Tinker, J. L. 2020a, arXiv e-prints, arXiv:2007.12200

—. 2020b, arXiv e-prints, arXiv:2010.02946

Tinker, J. L., Conroy, C., Norberg, P., et al. 2008, ApJ, 686, 53

Tinker, J. L., Hahn, C., Mao, Y.-Y., Wetzel, A. R., & Conroy, C. 2018, MNRAS, 477, 935

Tinker, J. L., Brownstein, J. R., Guo, H., et al. 2017, ApJ, 839, 121

Tissera, P. B., Beers, T. C., Carollo, D., & Scannapieco, C. 2014, MNRAS, 439, 3128

Tissera, P. B., Scannapieco, C., Beers, T. C., & Carollo, D. 2013, MNRAS, 432, 3391

Toft, S., van Dokkum, P., Franx, M., et al. 2007, ApJ, 671, 285

Toomre, A. 1977, in Evolution of Galaxies and Stellar Populations, ed. B. M. Tinsley & D. C. Larson, Richard B. Gehret, 401

Tortora, C., & Napolitano, N. R. 2012, MNRAS, 421, 2478

Tortora, C., Napolitano, N. R., Cardone, V. F., et al. 2010, MNRAS, 407, 144

Trager, S. C., Faber, S. M., Worthey, G., & González, J. J. 2000, AJ, 120, 165

Tripicco, M. J., & Bell, R. A. 1995, AJ, 110, 3035

Trujillo, I., Conselice, C. J., Bundy, K., et al. 2007, MNRAS, 382, 109

Trujillo, I., Feulner, G., Goranova, Y., et al. 2006a, MNRAS, 373, L36

Trujillo, I., Förster Schreiber, N. M., Rudnick, G., et al. 2006b, ApJ, 650, 18

Trussler, J., Maiolino, R., Maraston, C., et al. 2021, MNRAS, 500, 4469

Valentinuzzi, T., Poggianti, B. M., Saglia, R. P., et al. 2010, ApJL, 721, L19

van de Voort, F., Bahé, Y. M., Bower, R. G., et al. 2017, MNRAS, 466, 3460

van den Bosch, F. C., Aquino, D., Yang, X., et al. 2008a, MNRAS, 387, 79

van den Bosch, F. C., Pasquali, A., Yang, X., et al. 2008b, arXiv e-prints, arXiv:0805.0002

van den Bosch, F. C., Yang, X., Mo, H. J., et al. 2007, MNRAS, 376, 841

van der Burg, R. F. J., McGee, S., Aussel, H., et al. 2018, A&A, 618, A140

van der Wel, A., Holden, B. P., Zirm, A. W., et al. 2008, ApJ, 688, 48

van der Wel, A., Rix, H.-W., Wuyts, S., et al. 2011, ApJ, 730, 38

van der Wel, A., Franx, M., van Dokkum, P. G., et al. 2014, ApJ, 788, 28

van Dokkum, P., Conroy, C., Villaume, A., Brodie, J., & Romanowsky, A. J. 2017, ApJ, 841, 68

van Dokkum, P. G., Kriek, M., & Franx, M. 2009, Nature, 460, 717

van Dokkum, P. G., Franx, M., Kriek, M., et al. 2008, ApJL, 677, L5

van Dokkum, P. G., Whitaker, K. E., Brammer, G., et al. 2010, ApJ, 709, 1018

Vazdekis, A., Sánchez-Blázquez, P., Falcón-Barroso, J., et al. 2010, MNRAS, 404, 1639

Villaume, A., Conroy, C., Johnson, B., et al. 2017, ApJS, 230, 23

Vogelsberger, M., Genel, S., Springel, V., et al. 2014a, MNRAS, 444, 1518

—. 2014b, Nature, 509, 177

Wake, D. A., van Dokkum, P. G., & Franx, M. 2012, ApJL, 751, L44

Wake, D. A., Bundy, K., Diamond-Stanic, A. M., et al. 2017, AJ, 154, 86

Wang, E., Wang, H., Mo, H., et al. 2018a, ApJ, 864, 51

Wang, E., Wang, H., Mo, H., van den Bosch, F. C., & Yang, X. 2020, ApJ, 889, 37

Wang, E., Wang, H., Mo, H., et al. 2018b, ApJ, 860, 102

Wang, H., Mo, H. J., Jing, Y. P., et al. 2009, MNRAS, 394, 398

Wang, H., Mo, H. J., Yang, X., & van den Bosch, F. C. 2012, MNRAS, 420, 1809

Wang, H., Mo, H. J., Yang, X., et al. 2016, ApJ, 831, 164

Wang, Y., Yang, X., Mo, H. J., et al. 2008, ApJ, 687, 919

Wechsler, R. H., Bullock, J. S., Primack, J. R., Kravtsov, A. V., & Dekel, A. 2002, ApJ, 568, 52

Wechsler, R. H., & Tinker, J. L. 2018, ARA&A, 56, 435

Wechsler, R. H., Zentner, A. R., Bullock, J. S., Kravtsov, A. V., & Allgood, B. 2006, ApJ, 652, 71

Weinberger, R., Springel, V., Hernquist, L., et al. 2017, MNRAS, 465, 3291

Weinberger, R., Springel, V., Pakmor, R., et al. 2018, MNRAS, 479, 4056

Weinmann, S. M., van den Bosch, F. C., Yang, X., & Mo, H. J. 2006, MNRAS, 366, 2

Weisz, D. R., Dolphin, A. E., Skillman, E. D., et al. 2015, ApJ, 804, 136

Wellons, S., Torrey, P., Ma, C.-P., et al. 2015, MNRAS, 449, 361

—. 2016, MNRAS, 456, 1030

Westfall, K. B., Cappellari, M., Bershady, M. A., et al. 2019, AJ, 158, 231

Wetzel, A. R., Tinker, J. L., & Conroy, C. 2012, MNRAS, 424, 232

Wetzel, A. R., Tinker, J. L., Conroy, C., & van den Bosch, F. C. 2013, MNRAS, 432, 336

Whitaker, K. E., Kriek, M., van Dokkum, P. G., et al. 2012, ApJ, 745, 179

White, S. D. M., & Rees, M. J. 1978, MNRAS, 183, 341

Wilkinson, D. M., Maraston, C., Goddard, D., Thomas, D., & Parikh, T. 2017, MNRAS, 472, 4297

Worthey, G., Faber, S. M., Gonzalez, J. J., & Burstein, D. 1994, ApJS, 94, 687

Wu, P.-F., van der Wel, A., Gallazzi, A., et al. 2018, ApJ, 855, 85

Xie, L., De Lucia, G., Hirschmann, M., & Fontanot, F. 2020, arXiv e-prints, arXiv:2003.12757

Xu, X., & Zheng, Z. 2020, MNRAS, 492, 2739

Yan, R., Bundy, K., Law, D. R., et al. 2016a, AJ, 152, 197

Yan, R., Tremonti, C., Bershady, M. A., et al. 2016b, AJ, 151, 8

Yan, Z., Jerabkova, T., & Kroupa, P. 2021, arXiv e-prints, arXiv:2107.03388

Yang, X., Mo, H. J., van den Bosch, F. C., & Jing, Y. P. 2005, MNRAS, 356, 1293

Yang, X., Mo, H. J., van den Bosch, F. C., et al. 2007, ApJ, 671, 153

York, D. G., Adelman, J., Anderson, Jr., J. E., et al. 2000, AJ, 120, 1579

Zehavi, I., Contreras, S., Padilla, N., et al. 2018, ApJ, 853, 84

Zentner, A. R., Hearin, A., van den Bosch, F. C., Lange, J. U., & Villarreal, A. 2019, MNRAS, 485, 1196

Zentner, A. R., Hearin, A. P., & van den Bosch, F. C. 2014, MNRAS, 443, 3044

Zhao, D. H., Jing, Y. P., Mo, H. J., & Börner, G. 2009, ApJ, 707, 354

Zheng, Z., Wang, H., Ge, J., et al. 2017, MNRAS, 465, 4572

Zheng, Z., Li, C., Mao, S., et al. 2019, ApJ, 873, 63

Zhou, S., Mo, H. J., Li, C., Boquien, M., & Rossi, G. 2020, MNRAS, 497, 4753

Zibetti, S., White, S. D. M., Schneider, D. P., & Brinkmann, J. 2005, MNRAS, 358, 949

Zirm, A. W., van der Wel, A., Franx, M., et al. 2007, ApJ, 656, 66

Zolotov, A., Willman, B., Brooks, A. M., et al. 2009, ApJ, 702, 1058

Zolotov, A., Dekel, A., Mandelker, N., et al. 2015, MNRAS, 450, 2327

Zu, Y., & Mandelbaum, R. 2016, MNRAS, 457, 4360